

Concentration gradient generation for microfluidic applications

Toh, Alicia Guek Geok

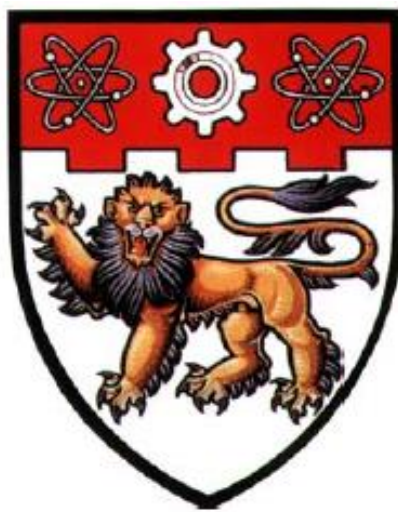
2016

Toh, A. G. G. (2016). Concentration gradient generation for microfluidic applications.
Doctoral thesis, Nanyang Technological University, Singapore.

<https://hdl.handle.net/10356/69096>

<https://doi.org/10.32657/10356/69096>

Concentration Gradient Generation for Microfluidic Applications



TOH GUEK GEOK, ALICIA

SCHOOL OF MECHANICAL & AEROSPACE ENGINEERING

NANYANG TECHNOLOGICAL UNIVERSITY

2016

CONCENTRATION GRADIENT GENERATION FOR MICROFLUIDIC APPLICATIONS

TOH GUEK GEOK, ALICIA

Supervisor:

Associate Professor Yang Chun

A Thesis Submitted for the Degree of

Doctor of Philosophy

School of Mechanical & Aerospace Engineering

Nanyang Technological University

Singapore

2016

Abstract

Microfluidic concentration gradient generators (μ C GG) are a unique class of fluidic devices that can be used to produce rapidly programmable, repeatable and precise concentration landscapes for biological applications. The miniaturization of length and time scales in μ C GGs has greatly improved the accuracy and control of concentration gradients, as compared to traditional techniques that utilize static diffusion chambers. However, the spatio-temporal control of chemical gradients with insignificant flow induced shear effects has proved difficult due to two conflicting mass transport mechanisms. The high temporal resolution for concentration gradient control is achieved at the expense of increasing flow rates which thereupon, results in strong flow induced shear effects. Due to this limitation, fast microfluidic gradient generation exposes cells to flow shear levels that may not be present in their native microenvironments. The presence of shear may elicit cell responses which differ greatly from that exhibited *in-vivo*.

This dissertation presents a systematic and in-depth investigation of using stagnation flows to control binary and combinational concentration gradients in low flow shear environments. Stagnation flows, characterized by their diminishing velocity fields that surround a stagnation point, are used to precisely confine concentration gradients under low flow shear conditions. Analogous to the confinement effects in potential wells, it is hypothesized that the diminishing flow fields around the stagnation point could function as fluid velocity wells. These velocity wells could be used to hydrodynamically confine and control concentration

gradients that are formed between concentration sources and sinks. A stagnation flow gradient generator is designed by making modifications to the conventional cross-slot design. Concentration generation of binary and combinational chemical species within the modified cross-slot (MCS) device is tested and evaluated. The concentration gradients formed across the stagnation velocity well is studied with respect to velocity well steepness. The effect of flow rate on velocity well steepness, flow shear stress, concentration gradient length and time to gradient stability is studied and characterized by introducing the dimensionless *Péclet* number. The *Péclet* number characterizes the balance between convection and diffusion. Experimental and numerical results show that the *Péclet* number is inversely scaled to gradient length but has a direct correlation to velocity well steepness, flow shear stress and time to gradient stability. This trend confirms the hypothesis that the stagnation flow can be used to control both temporal and physical parameters related to concentration gradient generation in velocity wells.

In this thesis, Chapter 1 introduces the background and motivation of this work, followed by a review of the state-of-the-art in microfluidic gradient generation, its role in biological applications and a summary of current gradient generation technologies. Chapter 2 delves into the design of the stagnation flow gradient generator, the analytical and numerical models used to understand the physical parameters governing concentration gradient generation across stagnation flows. Chapter 3 covers the device fabrication, experimental setup and protocols used in gradient generation studies. Chapter 4 presents the experimental and analytical results pertaining to steady-state and transient concentration gradient confinement

across stagnation flows. Chapter 5 describes experiments and numerical results regarding the use of stagnation flows to hydrodynamically confine and control both binary and combinational concentration gradient landscapes. Chapter 6 discusses the results obtained from biological experiments in which the individual cell sensing characteristics of *Pseudomonas Aeruginosa* (*P. Aeruginosa*) cells were studied in response to rapid temporal stimuli from a chemoattractant. Chapter 7 summarizes the findings of this thesis research and also provides recommendations for future areas of research.

Experiment results revealed that binary and combinational concentration gradients can be confined and stretched across velocity wells that are produced in stagnation flows. During concentration gradient generation, the convection- diffusion processes across the stagnation flow were found to have a direct correlation to the flow strain rate. Based on linear flow analysis, the flow strain rate is a key parameter in determining the characteristic flow velocities and *Pé* number of flows within the MCS device. Proper length and time scaling through the introduction of this *Pé* number results in a simplified analytical model that was used to describe the spatiotemporal characteristics of concentration gradient formation across stagnation flows. Experiments revealed that near the stagnation point, concentration gradient lengths of 85 μm to 350 μm are directly controllable while maintaining low flow-induced shear stresses. In line with the hypothesis, it was found that the stabilization and spatial movement of concentration gradients can be achieved rapidly, at temporal resolutions of 3s or less. The results highlight the efficacy of stagnation flows, and its velocity wells to produce low flow shear concentration gradients within short

characteristic times. Finally, this gradient generation approach was used to study freely rotating, tethered *Pseudomonas Aeruginosa* cells, in the presence of a fast changing chemoattractant microenvironment. As stagnation flow within the MCS device can be controlled dynamically, this allows us to test both the chemotactic response and adaptation of individual *P. Aeruginosa* cells. Stagnation flow within the MCS device was leveraged to study these cells since shear stresses as low as 2.4 mPa were found to adversely influence cell sensing and flagellum rotation during chemotaxis. Cell responses were studied in two scenarios- an abrupt enrichment and depletion of a chemoattractant (*L*-Serine) within the cells' microenvironment. Enrichment of the cells' microenvironment was achieved by flowing *L*-Serine into the stagnation chamber, thereby producing a ramp-up chemoattractant signal. On the other hand, stagnation flow introducing M9 medium (the control buffer) into the stagnation chamber produced a ramp-down in the chemoattractant signal. In both scenarios, chemoattractant signaling was achieved within 3s or less, thereby minimizing any data convolution resulting from signaling kinetics. In their pre-stimulus state, cells were found to spend equivalent durations in either clockwise or counter-clockwise rotational phases. This behavior was similar to control experiments performed in the petri dish. Upon exposure to ramp-up signals, cells experienced a bias in flagella rotation, allowing the cell to continue moving towards the favorable environment. However, when cells experienced the ramp-down signal, cells performed a reversal in their rotational phase, followed by a bias in the reversed rotational phase. In both cases, the rotational bias persisted for ~22s and subsequently returned to its pre-stimulus state, having little rotational bias. Calculation of the adaptation kinetics of *P. Aeruginosa* revealed that cells responded

to ramp-up and ramp-down chemoattractant signals similarly, with an adaptation time of 88.9s and 86.8s, respectively. The work presented here revealed that *P. Aeruginosa* exhibits an entirely different biophysical chemotactic adaptation as compared to that reported for the model *E.coli* cell. The findings here suggest that differences in the flagellar apparatus and chemosensory network of cells result in a variety of chemotactic and adaptation responses. Understanding these differences can lead to the development of relevant biophysical models and bring us closer to developing and controlling artificial molecular machines. Further to the work in this thesis, it is envisioned that the spatio-temporal resolutions achieved by this novel gradient generation approach would be useful for biological studies involving shear-sensitive cells.

Acknowledgements

I would like to express my deepest appreciation and gratitude to two of my Ph.D. supervisors, Associate Professor Yang Chun, Charles and Professor Nguyen Nam-Trung. Their valuable mentorship and continuous support throughout this project have helped me tremendously, especially in how to perceive and solve research problems. I am grateful to Prof Nguyen for introducing the field of microfluidics to me and allowing me to benefit from his insight in this field. Furthermore, I am grateful to Prof Yang for his wisdom and experience in microfluidics- this project would have been immensely difficult if not for all the illuminating discussions with Prof Yang. It has been a great privilege and honour to have worked under the mentorship of two awesome supervisors.

I also would like to thank Dr Wang Zhiping for his patience and guidance during the course of this project. I am particularly grateful to Dr Wang for allowing me to contribute as a research engineer with the Microfluidics Manufacturing Programme (MMP), SIMTech (A*STAR) while working on this thesis part-time. In particular, I am grateful for use of the amazing facilities in SIMTech and benefiting from many insightful discussions with my peer group in MMP. I am also thankful for the help rendered by Dr Chiam Keng Hwee and Dr Zeng Yu Kai from the Bioinformatics Institute, A*STAR for sharing their experience, protocols and knowledge in bacteria work.

Last but not the least, I would like to thank my family for their love, understanding and support in this journey of learning.

Contents

Abstract.....	II
Acknowledgements.....	VII
Contents	IX
List of Figures.....	XIII
List of Tables	XXV
Nomenclature.....	XXVI
1 Introduction.....	1
1.1 Background and motivation.....	1
1.2 Objective and scope	6
1.3 Outline of the dissertation.....	7
1.4 Literature review	9
1.4.1 Introduction.....	9
1.4.2 Basic mass transport phenomena in microfluidic gradient generators .	10
1.4.3 Characterizing pressure driven flow in concentration gradient generators.....	14
1.4.4 Mass transport in convection/ diffusion based gradient generators.....	19
1.4.5 Shear stresses associated with mass transport in convective type gradient generators.....	22
1.4.6 Time scales associated with mass transport in gradient generators.....	24
1.4.7 Types of gradient generator designs used in biological applications ...	29
1.4.7.1 Convective type gradient generators for investigating cell responses to chemical stimuli	29

1.4.7.2	Convective type gradient generator designs for studying cell responses to pulsatile and temporal stimuli	36
1.4.7.3	Gradient generator designs for low shear biological experiments	40
1.4.8	Summary	46
2	Theoretical Modelling of Convective- Diffusion Mass Transport in Stagnation Flow Concentration Gradient Generation	49
2.1	Introduction.....	49
2.2	Governing equations	52
2.2.1	Equations that govern fluid motion	52
2.2.2	Equations that govern mass transport phenomena.....	56
2.2.2.1	Mass transport due to diffusion	56
2.2.2.2	Mass transport due to the convection and diffusion	57
2.3	Analytical solution for mass transport across the stagnation flow	59
2.4	Numerical analysis of mass transport across stagnation flows.....	65
2.4.1	Time scale analysis	66
2.4.2	Mesh generation and domain setting	68
2.4.3	Boundary conditions for steady state analysis	71
2.4.4	Boundary conditions for transient analysis.....	73
2.4.5	Wall shear stress calculations from velocity fields.....	74
2.4.6	Summary	76
3	Modified Cross-Slot (MCS) Device Design, Fabrication and Experimental Setup	77
3.1	MCS device design	77
3.2	MCS Device Fabrication and Materials.....	80

3.3	Experimental Setup.....	84
3.3.1	Microfluidic experiment setup.....	84
3.3.1.1	Pressure versus flow rate calibration of the MCS devices.....	87
3.3.1.2	Sample preparation and fluorescence calibration	92
3.3.1.3	Experimental procedure and image processing	94
3.3.1.4	Particle image velocimetry (PIV) analysis	97
3.4	Protocols used for biological experiments.....	98
3.4.1	<i>P. Aeruginosa</i> cell culture and chemotaxis.....	98
3.4.2	Experimental process and analysis of cell responses.....	99
4	Steady-state and transient concentration gradient confinement through stagnation flow.....	102
4.1	Introduction.....	102
4.2	Stagnation flow characteristics and their role in convection-diffusion mass transport	105
4.2.1	Stagnation flow characteristics	105
4.2.2	Convection-diffusion mass transport in stagnation flows.....	110
4.3	Dynamics of concentration gradient formation in stagnation flows.....	115
4.4	Summary.....	118
5	Binary and Combinational Concentration Gradient Confinement in Stagnation Flow	120
5.1	Introduction.....	120
5.2	Stagnation flow characteristics of the MCS device	123
5.3	Confinement of binary concentration gradients.....	129
5.4	Hydrodynamic positioning of combinational concentration gradients.....	134

5.5	Summary	137
6	Dynamic Concentration Signalling for Studying Individual Cell Sensing	140
6.1	Introduction	140
6.2	Chemoattractant ramp signaling through stagnation flow	144
6.3	Resolving temporal and shear effects during signal ramps	149
6.4	Population based chemotaxis and chemotactic adaptation of individual <i>P.Aeruginosa</i> cells	154
6.5	Summary	162
7	Conclusion and Future Studies	164
7.1	Conclusion and contributions of this study	164
7.2	Recommendations for future studies	168
Appendix A.	FOTS Deposition Protocol	170
Appendix B.	Pressure Pump Design	171
Appendix C.	Experimental uncertainty analysis	174
Appendix D.	<i>Peclet</i> number calculations for flows	175
Appendix E.	Coefficient of variation analysis for steady state time within cell observation window	177
References	179

List of Figures

- Figure 1.1 Fully developed laminar flow within a microchannel. Flow profile is defined with reference to the rectangular co-ordinates shown. 15
- Figure 1.2 Shear stress in a microchannel: (a) Parallel plate flow induced shear stress on a cell residing on the bed of a microchannel. (b) Linear and proportional relationship between shear stress and flow rate. Change in maximum shear stress applied on cells when microchannel height, h is varied, for a fixed microchannel width of $w=1000\mu\text{m}$. The shear stress is plotted for water viscosity, $\mu=8.9\times 10^{-4}\text{ Pa}\cdot\text{s}$ 23
- Figure 1.3 (a)“Christmas tree” gradient generators used in chemotaxis studies of *E. coli* RP437 cells in response to singular and competing chemoeffector concentrations (Englert et al., 2010). Figure reproduced with permission from the American Society for Microbiology. (b) “Christmas tree” gradient generators used to conduct parallel melting curve analysis of matched and mismatched DNA oligonucleotides (Russom, Irimia, & Toner, 2009). Figure reproduced with permission from John Wiley and Sons..... 31
- Figure 1.4 Microfluidics based gradient generator designs: (a) (*left*) “Christmas tree” design for 1D (N. J. Jeon et al., 2000) and (*right*) 2D gradient generation (Paul J. Hung et al., 2005); (b) (*left*) Y- junction (Atencia et al., 2012), (*centre*) T-junction (Long & Ford, 2009) and (*right*) flow splitter designs (Irimia, Geba, & Toner, 2006); (c) (*left*) 1D gradient generation and (*right*) 2D gradient generation through pressure balance designs; (d)

Molded gels for (left) 1D (Ahmed et al., 2010a), (centre) 2D (C. R. Kothapalli et al., 2011) and (right) 3D gradient generation (Ulrike Haessler et al., 2011), and (e) Submersible microfluidic probes (Qasaimeh et al., 2011).	33
Figure 1.5 (a) (i) T-configuration design that produces (ii) drug gradients along the length of an isolated cancer tumour mass. (Walsh et al., 2009). Figures reproduced with permission from the Royal Society of Chemistry. (b) (i) Y-configuration device used for performing wound healing assays. Centre microchannel of the Y-device transports a stream of trypsin that detaches cells previously adhered to the channel substrate to artificially create a wound (ii). (iii) & (iv) show actin filament stains of endothelial cells under (iii) quiescent and (iv) shear flow conditions (Meer, Vermeul, Poot, Feijen, & Vermes, 2010).	33
Figure 1.6 (a) (i) Microvalve embedded device for generating pulsatile concentration gradients and (ii) Increase in glucose concentrations from 3mM to pulsing concentrations with a mean of 11mM (red line) applied to entrain intracellular Ca^{2+} oscillations from single islets of Langerhans. Reprinted with permission from (Zhang et al., 2010). Copyright (2010) American Chemical Society. (b) (i) Rootchip device used to incubate Arabidopsis thaliana root seedlings and expose them to (ii) temporal concentration gradients of glucose (Glc) and galactose (Gal)	38
Figure 1.7 (a) The “microfluidic palette” that provides spatiotemporal of overlapping concentration gradients for bacteria chemotaxis experiments (Atencia et al., 2009). (b) Fluorescent bead images highlighting the stagnation point	

created by the “microfluidic probe” to produce a binary concentration gradient (Qasaimeh et al., 2011).	43
Figure 1.8 Shear flow shielding by seeding cells in (a) deep microwells (Hung et al., 2005; Wang et al., 2008) or (b) on porous membranes (VanDersarl et al., 2011).	46
Figure 1.9 A summary of temporal and shear stress characteristics in convection, pressure- balance and diffusion microfluidic gradient generators. Grey circle covers the void in concentration gradient generators which can quickly stabilize concentration gradients, while maintaining low shear stresses.	47
Figure 2.1 (a) Conventional cross-slot device and (<i>lower</i>) concentration profile of the binary concentration gradient formed across line X-X'. (b) Modified cross-slot (MCS) device designed in this thesis consists of a main stagnation flow chamber that is linked to wide delivery channels via several narrow diffusion channels. (<i>lower</i>) Concentration profile of combinational concentration gradients formed across line X-X'.	51
Figure 2.2 G.I. Taylor’s macro-scale four roll mill apparatus (in planar view) and the MCS device equivalent for producing stagnation flow in microfluidics. Rotation of the four roll mills (with a radius, r) at an equivalent angular velocity of ω , results in the surrounding fluid to flow at a velocity, v . Analogous to the four roll mill, the MCS device produces stagnation flow of a purely extensional nature when $Q=Q_1=Q_2=Q_3=Q_4$	55
Figure 2.3 Symmetrical boundary conditions that are applied to the modified cross-slot (MCS) device- shown with flow streamlines. The characteristic	

length for mass transport within the MCS device is defined as d , half the diagonal length of the 1mm square chamber.	62
Figure 2.4 (a) 3D tetrahedral mesh for the MCS device which has a uniform depth of 12 μ m. (b) 3D tetrahedral mesh for the MCS device with cell chamber-Additional inlets for injecting cells are added to prevent cells from clotting the narrow diffusion channels. The cell chamber has a depth of 350 μ m while diffusion and delivery channels both have a depth of 12 μ m. (Right a,b) Zoomed-in mesh of the stagnation chamber for each device design.	69
Figure 2.5 Mid-plane slice of the velocity field within the MCS device. The velocity magnitude is subsequently used to map the maximum wall shear stress occurring chamber at the base. X , Y and Z are the global co-ordinates of the mesh geometry.	76
Figure 3.1 Device assembly and dimensions of (a) the MCS device, (b) the MCS device with valves and (c) the MCS device with a step-down cell chamber. All device dimensions shown are in <i>mm</i>	79
Figure 3.2 Schematic illustration of the soft lithography process that was used to fabricate (a) the MCS device, (b) the MCS device with valves and (c) the MCS device with step-down cell chamber.	82
Figure 3.3 Photograph of pre-filled PDMS devices consisting of (a) the Modified Cross-slot (MCS) design, (b) the MCS with valve design and (c) the MCS with step-down cell chamber.	84
Figure 3.4 (a) Equipment and experimental setup. (b) Zoomed-in view of the MCS device that is encircled in the orange box in (a). The fluorescein dye	

injected into the MCS device is illuminated with the excitation wavelength of 480nm and emits a yellow/ green fluorescent wavelength (~520nm). (c) Microscopy image of the MCS device. Scale bar shown in (c) is 1000 μ m.	85
Figure 3.5 Inlet flow rate versus pump pressure calibration curve for MCS devices having diffusion channels widths of 20 μ m, 30 μ m and 50 μ m. (<i>Inset</i>) Microscope images the MCS device with zoomed-in view (blue dotted box) of the different channel widths tested.	88
Figure 3.6 Inlet flow rate versus pump pressure calibration curve for MCS devices with valves. (<i>Inset</i>) Microscope image of the MCS device with fluidic channels (filled with blue dye) and underlying valve control channels, V ₁ -V ₄ (filled with red dye).	89
Figure 3.7 Inlet flow rate versus pump pressure calibration curve for MCS devices with extended cell chamber. (<i>Inset</i>) Microscope image of MCS device with flow inlets for the cell medium, Q_m and chemoattractant, Q_c	90
Figure 3.8 (a) Principle of membrane valve actuation within the MCS devices with valves- blue channel is filled with fluid and red channel is pressurized with air. (b) Valve closure (η) calibration plot with respect to inlet flow rate (Q) and valve actuation pressure (P_v).	92
Figure 3.9 Fluorescence emission calibration curve for (a) Fluorescein and (b) Rhodamine 6G solutions.	94
Figure 3.10 Measurement of the gradient length, L_g across the stagnation flow. The gradient length is obtained as the distance between 95% (<i>i.e.</i> C=0.95) and 5% (<i>i.e.</i> C=0.05) of the maximum normalized concentration. The abscissa	

of the plot is non- dimensionalized by the total diagonal length of the chamber, along the y-axis. (<i>Inset</i>) Typical grayscale image of fluorescein concentration gradient formed in MCS device; Line A-A' highlights the measurement of the concentration gradient along the y-direction.....	96
Figure 3.11 (a) Progression of fluorescein concentration stabilization across the stagnation point (marked by a white cross). (b) Plot of the normalized concentration level of the image pixel situated at the stagnation point (denoted by a white cross in (a)). The time for concentration stabilization at the stagnation point is defined by t_{ss}	97
Figure 4.1 (a) Design of the modified cross-slot device with (b) zoomed-in diffusion channels (in a dotted box). Diffusion channel width, w , is varied at $50\mu m$, $30\mu m$ and $20\mu m$. (c) Flow configuration used to form stagnation flow at the centre chamber. Flow rates in all the inlets, Q , are equivalent, resulting in a stagnation point forming at the centre of the chamber. The pump controller injects fluorescein, C_I and deionized water, C_0 from the liquid reservoirs and into the device inlets.	105
Figure 4.2 (a) Microparticle ($2\mu m$) streamlines tracing the formation of stagnation flow within the MCS device ($w=30\mu m$), at a flow rate of $Q=30nl\ s^{-1}$. Yellow arrow points to stagnation point at the chamber centre. Scale bar is $200\mu m$. (b) Flow velocity mapping of streamlines shown in (a). Colour bar indicates a velocity range from 0 (blue) to $0.5\ mm\ s^{-1}$ (red). L represents the length of the stagnation chamber ($L= 1mm$). (c) Flow velocity profiles along the y-axis that is non-dimensionalized by d , the distance between the chamber edge and the central stagnation point	

shown in (b). (d) Effect of flow rate on the flow strain rates produced within different MCS devices. Error bars in (c, d) were calculated from 100 image pairs using an experimental uncertainty analysis (see Appendix A for details).	106
Figure 4.3 (a) Concentration gradient formed by convection-diffusion processes across the stagnation flow with an MCS design of $w=30\mu\text{m}$. Scale bar represents $200\mu\text{m}$. (b) Concentration gradients formed at different flow rates, magnified from the location of the yellow dotted box in (a). (c) Comparison between experimental and analytical concentration profiles. (d) Comparison of gradient length, L_g across different diffusion channel widths, w , for a range of flow rates. The gradient length (L_g) is determined as the distance along line A-A' that separates 5% and 95% of the normalized concentration shown in (c).	112
Figure 4.4 Linear correlation between the concentration gradient, L_g and the <i>Péclet</i> number, Pe , within the stagnation flow.	114
Figure 4.5 Time-dependent transport of fluorescein solute obtained through (a) experiments and (b) numerical simulations of MCS devices with $30\mu\text{m}$ diffusion channels. (c) Concentration profiles showing the stabilization of the concentration levels at the stagnation point of the MCS device with $30\mu\text{m}$ diffusion channels. (d) Effect of flow rate on the time required for fluorescein concentration to stabilize at the stagnation point.	117
Figure 5.1 (a) Microscope image of the MCS device with a fluidic layer (filled with blue dye) and a pneumatic valve layer (filled with red dye). (b) Streakline traces of the extensional stagnation flow formed at the centre of the	

stagnation flow chamber. (c) Pump and flow configurations used to control stagnation flow within the MCS device. Inset shows the 3D valve configuration and valve actuation scheme that was used to hydrodynamically control the position of the stagnation point. 124

Figure 5.2 (a) Vector mapping of flow velocities within the stagnation chamber ($Q=100\text{nl s}^{-1}$). Arrow scale indicates velocity vector strength of 2 mm s^{-1} . Scale bar represents $100\mu\text{m}$. (b) Velocity component (v_x) along the dimensionless x -axis (x/d) where d is half the diagonal length of the chamber. Inset in figure shows how the homogeneous flow strain rate, ϵ is calculated from the velocity profile. (c) Residual data, e , which plots the difference between measured velocity profiles (v_x) and the linear correlations (vx). (d) Velocity gradient, also known as flow strain rate plotted with respect to the inlet flow rates. 126

Figure 5.3 (a) Flow velocity profile measured from stagnation flows at various flow rates. (b-d) Two-dimensional velocity mapping showcasing the velocity well that increases in steepness as the inlet flow rates are increased.... 128

Figure 5.4 (a) Binary source fluorescein gradient across stagnation flow. (b) Concentration gradient along line B'-B'' for various flow rates. (c) Focused 2D concentration contours (from dotted box in (a)), comparing experimental (upper) and numerical (lower) concentration gradient formation. Scale bar represents $200\mu\text{m}$ for images in (c). (d) Measured concentration gradient length, L , for various flow rates. (*Inset*) Time slices of concentration gradient across line B'-B'' for a time period of 2

hours. In plots (b) and (d), dotted lines represent numerical simulation results.	130
Figure 5.5 (a) Shear stress contour map of the stagnation chamber for a flow rate of $Q=50 \text{ nls}^{-1}$. (b) Maximum flow-induced shear stresses for various inlet flow rates. c_v measures the % variation between the measured and numerical wall shear stresses.	132
Figure 5.6 (a) 2D velocity maps (<i>top</i>) and streakline images (<i>bottom</i>) highlighting the variation of the stagnation point with the non-dimensionalized flow factor, f . Circular velocity wells are present around the stagnation point as they are moved across the chamber along the line C'-C''. White arrows indicate the stagnation point location. Scale bar represents 200 μm . (b) Locational map of stagnation point translation along line C'-C''. (c) Characterization plot of stagnation point location, y with respect to flow factor, f . The stagnation point location, y is scaled using the length of line C'-C'' such that $y = y/(C' - C'' \text{ length})$	135
Figure 5.7 (<i>Upper</i>) Confinement of fluorescein and rhodamine 6G overlapping concentration gradients as stagnation flow is tuned with respect to the flow factor. (<i>Lower</i>) Localization of stagnation point with flow factor adjustment. Arrows point to stagnation point location for each non-dimensionalized flow factor, f . Scale bar represents 200 μm for images.	137
Figure 6.1 Microfluidic and chemotaxis protocol used during experiments. (a) Image of flow within main chamber when chemoattractant (visualized here using fluorescein dye) is introduced into the main chamber. (b) Temporal	

ramp up and ramp down signals experienced by cells within the main chamber. To generate a ramp up in chemoattractant concentration, Q_c is set at higher flow rate than Q_m , allowing chemoattractant to enter the chamber (c). To generate a ramp down in chemoattractant concentration, Q_m is set at a higher flow rate than Q_c , allowing medium to flush out chemoattractant from the chamber (d). (e) During the process of ramping chemoattractant concentrations, individual tethered cells within a central $100\mu\text{m}$ square periphery of the velocity well, are observed using time-lapsed microscopy. The cell rotation videos (population size of 50 cells) are entered into a bacteria tethering analysis program (*BTAP*) to extract information such as cell rotation speed and rotation phase frequency for each individual cell. 145

Figure 6.2 Stagnation point formation and concentration signal gating within the stagnation flow chamber. (a) Streakline image of stagnation flow with a yellow dotted arrow pointing to the stagnation point in the centre of the chamber. Scale bar represents $100\mu\text{m}$. (b) Corresponding flow rates for chemoattractant, Q_c , and medium, Q_m , that were used to either ramp up or ramp down the chemoattractant concentration within the stagnation chamber. (c) Example of how flow rate ratios influence chemoattractant concentrations within the stagnation chamber. 147

Figure 6.3 Shear stress induced by flow velocities during the onset of bacteria motor stalling. (a) Velocity mapping within the observation window for the chemoattractant flow rate of $Q_c=190\text{nl s}^{-1}$ (arrow points to the central stagnation point) and (b) Maximum flow velocities and corresponding

<p>wall shear stresses, τ_{wss}, with respect to the chemoattractant flow rate. Bacteria rotation experiences stalling at a threshold flow rate of $Q_c=220\text{nl s}^{-1}$ (<i>i.e.</i> $\tau_{wss}=2.43\text{mPa}$).....</p>	151
<p>Figure 6.4 Stagnation flow dynamics resulting in precisely controlled steady state ramp-up and ramp-down chemoattractant signalling. (a) Progressive filling of chemoattractant ($Q_c= 190\text{nl s}^{-1}$) into the stagnation chamber during ramp-up signalling and (b) filling of medium ($Q_m = 123\text{nl s}^{-1}$) into the stagnation chamber during ramp-down signalling. (c) Ramp-up and (d) ramp-down signal steady state response across five locations of the observation window shown in (a). Insets in (c) and (d) are concentration profiles with zoomed-in time scales. (e) Time required for ramp-up or ramp-down signal to completely fill the chamber. Scale bars in images (a, b) represent $100\mu\text{m}$.</p>	153
<p>Figure 6.5 Quantitative analysis of the rotation profile of a tethered <i>P. aeruginosa</i> cell before (0-60 s) and after (60-120 s) addition of chemoattractant L-serine or control buffer M9. (a) Phase contrast time-lapsed images of a tethered cell rotating in the CW and CCW direction (<i>top</i> and <i>bottom</i> row respectively). <i>Red lines</i> denote horizontal lines passing through the axis of rotation of the cell. (b) Scattering profile of the centroid positions of the tethered cell throughout the experiments at 40 fps for 120 s, with the <i>cross</i> indicating the bacterial rotation axis. (c) Instantaneous rotational speed of a tethered <i>P. aeruginosa</i> cell during a L-serine ramp-up experiment. (d) Rotational profile of the cell being classified into CW, CCW or pause phases during a L-serine ramp-up experiment. The <i>blue</i></p>	

triangle denotes the time in which L-serine is added. The pie charts show the percentage of *CW* (*red*), *CCW* (*green*) and pause (*white*) for every 20 seconds (thick *bars* at the bottom of the time series). (e) Instantaneous rotational speed of a tethered cell during ramp-down exposure in which M9 medium is flooded into the cell chamber. (f) Rotational profile of the cell being classified into *CW*, *CCW* or pause phases during the ramp-down experiments. The *blue triangle* denotes the time in which the chemoattractant was removed..... 157

Figure 6.6 Moving time window analysis of the rotational behavior of *P. Aeruginosa* during a (a,c) ramp up and (b,d) ramp down of chemoattractant concentrations within their surroundings. (e) Using the adaptation profile shown in (a-d), the adaptation time for both scenarios was determined for a population of 50 cells. 161

List of Tables

Table 1.1 Overview of the use of Navier-Stokes (N-S) equation in microfluidics ...	11
Table 1.2 Electric- hydraulic analogy and its applicability in microfluidic gradient generators	17
Table 1.3 Overview of the use of convection-diffusion (C-D) equation in microfluidic-based mass transport	20
Table 1.4 Overview of the characteristic time scales for microfluidic gradient generators	25
Table 1.5 Typical operation characteristics- flow velocity (U), characteristic length (L_c), <i>Péclet</i> number ($Pé$) and characteristic time (t_c) for gradient stabilization in convection and diffusion based gradient generators. Velocity values in parentheses are derived based on $\langle U \rangle = L_c/t_c$	26
Table 2.1 Meshing characteristics for simulating flow and concentration fields within the basic MCS device and the MCS device with cell chamber.	70
Table 2.2 Parameter values used to determine velocity and concentration fields.	71
Table 2.3 Boundary conditions for simulating steady-state velocity and concentration fields.....	73
Table 4.1 Correlation fitting (R^2) between the analytically calculated and experimentally measured concentration gradient profiles.	112
Table 4.2 Prediction of the gradient length, L_g , using the linear correlation, $L_g = C_w / \sqrt{Pé}$ where C_w is an empirically derived constant for each MCS device	114

Nomenclature

a	Hydrodynamic radius [m]	v_y	Flow velocity along y-axis [m s ⁻¹]
C	Concentration of sample solutes [M]	P	Pressure [Nm ⁻²]
D	Mass diffusion coefficient of solutes [m ² s ⁻¹]	t	Time [s]
\tilde{f}	Non-dimensionlized flow factor [m ³ /m ³]	I	Current [A]
L	Square chamber length [m]	V	Voltage [V]
L_d	Diagonal chamber length [m]	Re	Reynolds number
L_s	Length of stagnation well [m]	Pe	Peclet number
U	Velocity magnitude, $U = \sqrt{v_x^2 + v_y^2}$ [m s ⁻¹]	τ	Characteristic time [s]
\bar{U}	Mean flow velocity [m s ⁻¹]	ϕ	Flow potential [m ² s ⁻¹]
U_{max}	Maximum flow velocity [m s ⁻¹]	ψ	Flow stream function [m ² s ⁻¹]
s	Velocity well steepness near the stagnation point, $s = \Delta U / L_s$ [s ⁻¹]	$\dot{\epsilon}$	Flow strain rate [s ⁻¹]
d	Thickness of device chamber [m]	ρ	Medium density [kgm ⁻³]
ν	Medium kinematic viscosity [m ² s ⁻¹]	μ	Medium dynamic viscosity [kg m ⁻¹ s ⁻¹]
v_x	Flow velocity along x-axis [m s ⁻¹]	σ	Wall shear stress [Pa]

1 Introduction

1.1 Background and motivation

In microfluidics, small volumes of reagents in the range of nanolitres to microliters are manipulated through networks of sub-micron to micrometer sized channels. Through sequential and automated processes of mixing and interdiffusion, concentrations levels or gradients of multiple chemical species can be formed within a single device. In most cases, the resolution of concentration gradients formed range from several to hundreds of microns, and are efficiently controlled by channel geometries, configurations and flow rates. Concentration gradient generation in microfluidics enables the precise control of multiple design spaces, specifically, time, space and concentrations of chemical species, into a single platform (Chung & Choo, 2010; Gupta et al., 2010; Keenan, Hsu, & Folch, 2006; Toetsch, Olwell, Prina-Mello, & Volkov, 2009).

The precise control achieved by microfluidic gradient generators (μ CGG) has revolutionized how microenvironments are recreated for *in-vitro* biological studies. This was previously not possible with conventional platforms such as the Boyden chamber (Boyden, 1962), Dunn slide chamber (Zicha, Dunn, & Brown, 1991), Zigmond chamber (Zigmond & Hirsch, 1973), agarose/petri dish (S. Kim, Kim, & Jeon, 2010) and the micro-aspirator (Incropera, DeWitt, Bergman, & Lavine, 2006). Conventional platforms rely on transient diffusion, resulting in temporally saturating concentration gradients that obscure the extraction of quantitative data regarding cell responses to specific concentration levels. The transient problem is further exacerbated

when small molecules with high diffusivity are used, since concentration levels quickly saturate between chambers, even before cell assaying is complete. Furthermore, biologists using conventional platforms were not able to control concentration gradients as required, making it difficult to study dynamic cell responses to rapid changes in chemical stimuli- a scenario that features heavily in cell adaptation (Johnson-Chavarria, Agrawal, Tanyeri, Kuhlman, & Schroeder, 2014; Min, Mears, Golding, & Chemla, 2012). To this end, many μ CGG devices have been designed to study biological processes related to immune response (Kothapalli et al., 2011; Li et al., 2008; Lin et al., 2004; Wang et al., 2008a), embryogenesis (Heo et al., 2010), cancer metastasis (Mosadegh et al., 2008; Nandagopal et al., 2011; Saadi et al., 2006; Wang et al., 2004) and cell sensing (Kalini et al., 2009; Min et al., 2012).

One of the challenges faced by current microfluidic gradient generator (μ CGG) devices is the fast generation of concentration gradients without the introduction of physiologically unrealistic shear stress triggers (Hu et al., 2011). Characteristically, this is a fundamental mass transport problem since fast concentration gradient generation precludes the use of relatively high flow rates to transport concentration species. Consequently fast flow rates induce high levels of shear stresses on cells, which usually do not exist in their native microenvironments. For this particular reason, fast temporal control of concentration gradients has only been demonstrated on cells that natively experience significant shear stress latitudes (Walker et al., 2005). An early representation of the μ CGG was in the form of the “Christmas tree” device demonstrated by the Whitesides' team (Jeon et al., 2000).

The “Christmas tree” device has a series of parallel mixers that were cascaded to sequentially mix solute and buffer concentrations, and deliver flow streams consisting of varying concentration levels. These streams were then converged and eluted into a single laminar stream within the concentration gradient chamber (Jeon et al., 2000). Subsequent studies on this μ CGG device focused on correlating cell sensing behavior (chemotaxis) of neutrophils (Jeon et al., 2002), fibroblast (Kane et al., 2006) and cancer cells (Wang et al., 2004). These adherent cells have particularly robust tolerances to shear stresses within their physiologically microenvironments—although most of the aforementioned studies could not quantify shear stress effects on the cell responses measured.

Since the introduction of the “Christmas tree” μ CGG device, design improvements have been made to generate concentration gradients in a shear-free manner (Kothapalli et al., 2011; Li et al., 2008). μ CGG devices that seek to generate shear-free concentration gradients employ membranes (VanDersarl et al., 2011), hydrogels (Gabrielson et al., 2013) or deep bottom trenches (Hung, et al., 2005; Wang et al., 2008) to shield shear-sensitive cells from the high flow velocities. Predominantly, these structures deflect high fluid velocities away from cells thus reducing flow-induced shear stresses. As a consequence, however, precise dynamic control of the concentration gradient is sacrificed. For example, concentration gradients formed in hydrogels cannot be dynamically moved or varied once the concentration species has saturated the gel. Likewise, membranes or trenches also severely limit the temporal precision in which concentration gradients can be delivered to or away from cells.

To resolve the conflicting mass transport requirements of precise spatiotemporal control and low flow-induced shear stresses, a new class of gradient generation strategies has been proposed. These strategies utilize counteracting flow pairs to create a low shear, interdiffusion concentration gradient zone where each counteracting flow acts as either a source or sink. Device configurations using this strategy seek to reduce shear stresses within the gradient forming zone by the destructive superposition of flow shear present in each flow stream. Precise temporal control of concentration gradients using these devices has been applied to study axon guidance in neurons (Queval et al., 2010), stem cell differentiation (Park et al., 2009) and chemotaxis of highly motile non-adherent cells (Atencia et al., 2009).

Further to this concept of flow balancing, recent studies have demonstrated the balancing of opposing flow streams to generate velocity wells which confine nanoparticles in stagnation flows (Probst et al., 2012; Tanyeri & Schroeder, 2013). Deductively, such flows and their associated velocity wells could possibly be extended to the dynamic confinement and control of concentration gradients, in a low shear environment. An examination of the literature reveals a dearth of studies on how stagnation flow characteristics could influence convection-diffusion mass transport processes for concentration gradient generation. In the current narrative of μ CGG s, no studies have been endeavoured on using stagnation flows and their surrounding velocity wells to confine and control concentration gradients. There is also a lack of understanding on the physical parameters that influence the patterns of chemical diffusion across such flows. Furthermore, current gradient generation schemes utilizing either convection, diffusion transport or both transport mechanisms

in parallel, have not successfully demonstrated a fast control of combinational concentration landscapes, while suppressing flow-induced shear stresses. Most notably, due to the lack of such a gradient generation scheme, many questions that distinguish shear stress effects from dynamic cell responses in chemotaxis and adaptation remain unasked and unanswered. The key motivation of this thesis is thus, to develop a gradient generation technique that resolves shear stress effects which are associated with the fast convective mass transport of concentration species- a limitation in current μ CGG devices.

1.2 Objective and scope

The objective of this dissertation is to develop the fundamental framework for understanding the physical parameters that affect mass transport of concentration species across microfluidic stagnation flows. The objective will be achieved by utilizing laminar flow within microfluidic devices to demonstrate stagnation flow control and hence concentration gradients, thereby providing a low-shear microenvironment for biological studies. To fulfill the objective, the following research scope has been identified:

- (1) Development of a mathematical model to describe the physical parameters that influence the confinement and control of concentration gradients in stagnation flows.
- (2) Experimental, analytical and numerical studies of concentration gradient confinement across stagnation flow. Quantification of time dependent mass transport parameters with respect to the shear stress generated within the device.
- (3) Demonstration of stagnation flow to provide low shear and dynamically controllable concentration gradients for the study of *P. Aeruginosa* bacteria chemotaxis.

1.3 Outline of the dissertation

There are seven chapters in this dissertation. Chapter 1 introduces the background and motivation of this work. The latest developments in microfluidic concentration gradient generation are reviewed. The objectives and outline of this study are then described.

Chapter 2 details the theoretical modeling of concentration gradient generation based on stagnation flow kinematics. The modified cross-slot (MCS) device design and flow characteristics are described. The underlying flow mechanisms within the MCS device are introduced using a proposed analytical model. In addition, the numerical methods used for solving the transient and steady-state governing equations are described.

Chapter 3 describes the soft lithography processes used to fabricate three variants of the MCS device that were designed to achieve concentration gradient tuning across stagnation flow. This section includes details of the experimental setup, sample preparation and experimental methods used to characterize flow within the devices.

Chapter 4 presents the key findings associated with concentration gradient generation in stagnation flow for the MCS device. A systematic study on the effects of channel geometry and flow rate on concentration gradient generation was conducted. Experimental results were discussed in terms of the flow strain rate and a

proposed Péclet number. Both steady-state and transient convection-diffusion processes were discussed in terms of the characteristic length and time scale of the device. Experimental, analytical and numerical results obtained were compared and summarized.

Chapter 5 discusses the experimental and numerical studies that utilize the MCS device with valves to hydrodynamically control stagnation flow and entrain combinational concentration gradients. Experiment results highlighting the use of flow rates to directly tune concentration gradient lengths via velocity wells, are discussed. The experiment results were also compared to numerical simulation results. Experiment data on the effects of flow velocity on flow-induced wall shear stresses is also presented and discussed.

Chapter 6 demonstrates the use of stagnation flows to deliver rapid chemoattractant concentration ramps to *P. Aeruginosa* cells within the MCS device consisting of a cell chamber. Characterization of temporal concentration gradients was performed. These results were analyzed in parallel to the maximum flow-induced shear stresses within the MCS device. Individual cell rotation responses and chemotactic responses to the sudden chemoattractant ramp were analyzed and discussed.

Chapter 7 summarises all the key findings and major contributions of this thesis in the field of microfluidic concentration gradient generation. Future work based on concentration gradient control in stagnation flow is proposed.

1.4 Literature review¹

This section discusses the theory behind concentration gradient generation, state-of-the-art in concentration gradient devices and, the different device configurations applied in biological studies.

1.4.1 Introduction

A microfluidic gradient generator manipulates small volumes of reagents through networks of microchannels. The advances in microfabrication technology have led to the continuous miniaturization of channel geometries, thereby reducing gradient generating lengths down to micrometer or even nanometer resolutions. The miniaturization of channel dimensions directly correlates to a reduction in the time required to transport specific concentration doses to cells, thus enabling physiologically relevant time scales. Microfluidic gradient generators also enable the integration and manipulation of multiple design spaces, predominately: time, and the localization of chemical species and chemical concentrations, into a single platform (Chung & Choo, 2010; Gupta et al., 2010; Keenan & Folch, 2008; Toetsch et al., 2009). Precise control of these design spaces has revolutionized the way biologist control cell microenvironments for *in-vitro* studies. The benefits of minute time and length scales in microfluidics have translated into precise control of concentration gradients for drug development (Chen et al., 2012; Maguire et al., 2009; Mosadegh et

¹ This chapter is in part reproduced with permission from Springer [A.G.G Toh, Z.P. Wang, C. Yang and N-T Nguyen, *Microfluidics and Nanofluidics*, 16(1), pp. 1-18 (2014)].

al., 2008; Nandagopal et al., 2011; Sugiura et al., 2010) and chemotaxis studies (Ahmed et al., 2010b). Microfluidic gradient generators have also emerged as efficient platforms for controlling biomolecular microenvironments for cell culture viability studies (Chen et al., 2008; El-Ali et al., 2006; Gomez-Sjoberg et al., 2007; Ziolkowska et al., 2010) and stem cell development (Gupta et al., 2010; Park et al., 2007).

In the recent fifteen years, the use of microfluidic gradient generators has burgeoned in biological applications, prompting researchers in both the microfluidics and biological arena to publish several reviews (Beta & Bodenschatz, 2011; Keenan & Folch, 2008; Kim et al., 2010; Mark et al., 2010; Velve-Casquillas et al., 2010; Weibel & Whitesides, 2006). Many of these reviews have summarized key biological applications of microfluidic gradient generators with limited emphasis on how microfluidic-based mass transport phenomena could be effectively engineered for such applications. In this section, the core engineering aspects of designing and controlling gradient generators are analyzed for various applications. This literature review covers two main areas, namely: microfluidic-based mass transport phenomena and the use of gradient generator designs for specific biological applications.

1.4.2 Basic mass transport phenomena in microfluidic gradient generators

Fluid flow fields that transport concentration gradients within microfluidic devices are governed by the Navier-Stokes (N-S) equation (see Table 1.1). In

microfluidic flow of liquids, the N-S equation that is applied assumes that the fluids used are incompressible and Newtonian in nature. The assumption of incompressibility is made as liquids experience negligible volume changes in response to pressure changes (Incropera et al., 2006). Similarly, fluids used in gradient generators, for biological studies are usually Newtonian in nature and do not have viscosity values that vary with the flow velocity of the liquid. Examples of Newtonian fluids used in gradient generators include water-based fluorescent dyes (Morel et al., 2012), cell medium (Kilian et al., 2010; Park et al., 2009), dilute solutions of growth factors (Mosadegh et al., 2008; Wang et al., 2004) and proteins (Lin et al., 2004; Nandagopal et al., 2011) and medical drugs (Dai et al., 2010; Walsh et al., 2009; Wang et al., 2009). Applicable to incompressible Newtonian fluids, the constitutive N-S equation balances the rate of change in fluid momentum with the convective, viscous, and pressure forces, and other externally applied forces (see equation [1.1] in Table 1.1). In the absence of externally applied electrical or gravitational forces- as in the case of microfluidic gradient generators, the force term, \vec{F} , is omitted from analysis of the N-S equation.

Table 1.1 Overview of the use of Navier-Stokes (N-S) equation in microfluidics

Constitutive N-S equation (incompressible flow)	$\rho \frac{\partial \vec{u}}{\partial t} = -\rho(\vec{u} \cdot \nabla)\vec{u} + \mu \nabla^2 \vec{u} - \nabla P + \vec{F} \quad [1.1]$ where ρ is the density of the fluid, \vec{u} denotes the velocity vector of the fluid, μ is the dynamic viscosity of the liquid, ∇P is the pressure gradient, and \vec{F} is the external force applied to the fluid.
Microfluidics N-S equation (low Re number and transient flow)	$\rho \frac{\partial \vec{u}}{\partial t} = \mu \nabla^2 \vec{u} - \nabla P \quad [1.2]$
Microfluidics N-S equation (low Re number and steady-state flow)	$\nabla P = \mu \nabla^2 \vec{u} \quad (\text{E 1.1}) \quad [1.3]$

In general, fluid flow in microfluidic channels is slow and laminar due to small channel dimensions. The laminar flow within microfluidic devices is characterized by the Reynolds number, Re , that is often much smaller than 2.3×10^3 (Squires & Quake, 2005). The Re number is a dimensionless number that measures the relative importance between inertial $\left(\frac{\rho U^2}{L_c}\right)$ and viscous forces $\left(\frac{\mu U}{L_c^2}\right)$ and is defined in equation [1.4]. For Newtonian fluid flow ($\rho = 10^3 \text{ kg m}^{-3}$ and $\mu = 10^{-3} \text{ Pa} \cdot \text{s}$) in microfluidic systems, typical values for the characteristic length and velocity are $L=10^{-6}$ to 10^{-4} and $U=10^{-3} \text{ ms}^{-1}$, respectively. This typically results in a Re range of 10^{-2} to 10^0 .

$$Re = \left(\frac{\rho U^2}{L_c}\right) / \left(\frac{\mu U}{L_c^2}\right) = \frac{\rho U L_c}{\mu} \quad [1.4]$$

where ρ is the fluid density, U is the characteristic fluid velocity and L_c is the characteristic length of the fluidic channel. U may be determined from the inlet flow rate using the volumetric flow rate equation, $Q=U \cdot A$, where A is the channel cross-sectional area. In rectangular microfluidic channels, the characteristic length L is approximated as the hydraulic diameter, $D_h = \frac{4 \cdot A}{P_w}$, where P_w is the wetted perimeter of the channel.

Although the Re number is frequently associated with fluid dynamics and mechanics, the Re number has little relevance in the analysis of convection-diffusion driven mass transport in microfluidics. In the microfluidic domain, the small length scales and low flow rates used result in Re numbers that are usually less than 100.

During mass transport analysis of microfluidic channels, Re is used as an indication of the order of magnitude of flow velocities characterizing concentration gradient generation. In purely diffusion based microfluidic gradient generators, where $Re \ll 1$, negligible convective forces are present (*i.e.* $\rho \vec{u} \cdot \nabla \vec{u} \rightarrow 0$). When $Re \ll 1$, the viscous forces ($\mu \nabla^2 \vec{u}$) are dominant over convective forces ($\rho \vec{u} \cdot \nabla \vec{u}$) and the convective term is omitted from the constitutive N-S equation (see equation [1.2] in Table 1.1) (Deen, 1998). Further simplification of the constitutive N-S equation can be achieved by solving the flow velocity in steady-state (independent of time). The N-S equation representing steady-state, low Re flow in microfluidic channel is presented in equation [1.3] of Table 1.1. This form of the N-S equation is also known as the Stokes equation.

Flow velocities within microfluidic gradient generators are commonly solved by applying appropriate assumptions and simplifications to the constitutive N-S equations. These simplifications reduce the analytical or numerical computation time required to solve for the velocity field. The velocity field solutions form the basis for solving mass transport problems in microfluidic gradient generators. In the next section, the analytical solution for laminar and uni-directional flow within pressure driven convection- based concentration gradient generation is discussed.

1.4.3 Characterizing pressure driven flow in concentration gradient generators

In pressure driven gradient generators, the steady state N-S equation (equation [1.3]) is commonly used to define flow velocities for a known pressure drop (ΔP) across channel lengths, in the absence of externally applied forces, *i.e.* $\vec{F} = 0$. In low Reynolds number flows, the viscous terms in the N-S equations become dominant and the inertial terms become relatively unimportant. In such cases, the steady- state, incompressible N-S equation reduces to Stokes' equation. Stokes' equation can be analytically solved in one direction for gradient generators that have only one non-zero velocity component, *i.e.* unidirectional flow. By assuming fully developed fluid flow in long microchannels, the Stokes' equation can be solved along the channel length (x - direction in this case) to give an exact solution for the average flow velocity, U , or flow rate, Q (since $Q=U \times A$) for a known pressure drop (see equation [1.5]). In equation [1.5], the pressure drop along the channel length is only a function of channel length in the x - direction, *i.e.* $\frac{dP}{dx}$. Within a rectangular microchannel, the velocity profile (u) is a function of the channel width (w) in the y direction and the channel height (h) in the z direction, *i.e.* $u=u(y,z)$. The velocity profile and channel dimensions associated with pressure- driven flow in microchannels are illustrated in Fig. 1.1.

By implementing the no-slip boundary conditions at the walls of the microchannel, and applying finite Fourier transformation on equation [1.5], an exact solution showing a linear relationship between ΔP and Q can be derived (see

equation [1.6]). A detailed description of the derivations required to solve for equation [1.5] can be found in many textbooks (Nguyen & Wesley, 2002; Nguyen, 2012). This is one of the few exact solutions of the N-S equation that can be derived analytically. Equation [1.6] is also known as the Hagen-Poiseuille equation and defines the hydraulic resistance (R_f) of fluid flow within a microchannel. R_f is dependent on the dynamic viscosity of the fluid, μ , and the geometry of the microchannel.

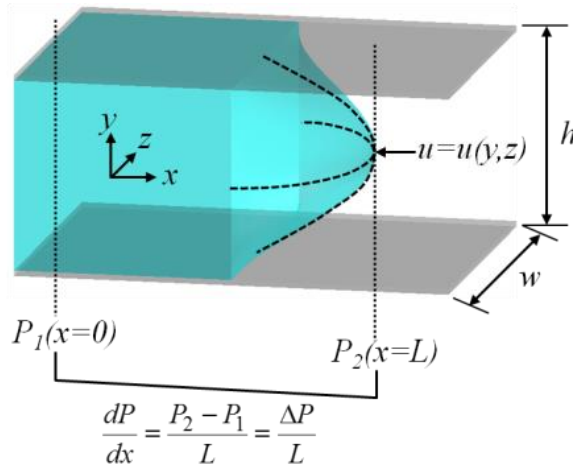


Figure 1.1 Fully developed laminar flow within a microchannel. Flow profile is defined with reference to the rectangular co-ordinates shown.

The Hagen-Poiseuille equation is commonly used to simplify fluid flow in microfluidic networks (Nguyen & Wesley, 2002):

$$\left(\frac{\partial^2 u}{\partial y^2} + \frac{\partial^2 u}{\partial z^2} \right) = \frac{1}{\mu} (\Delta P) \quad [1.5]$$

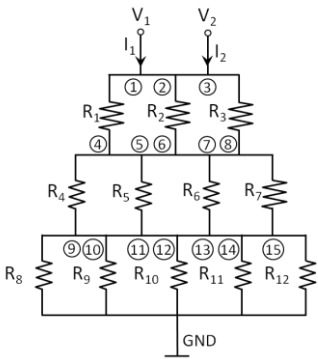
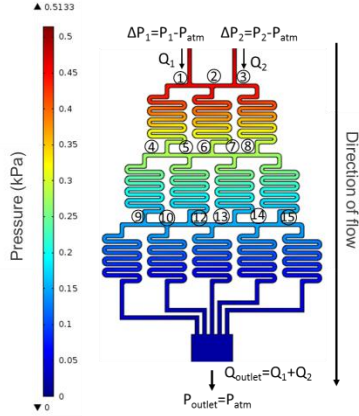
$$\Delta P = R_f Q \quad [1.6]$$

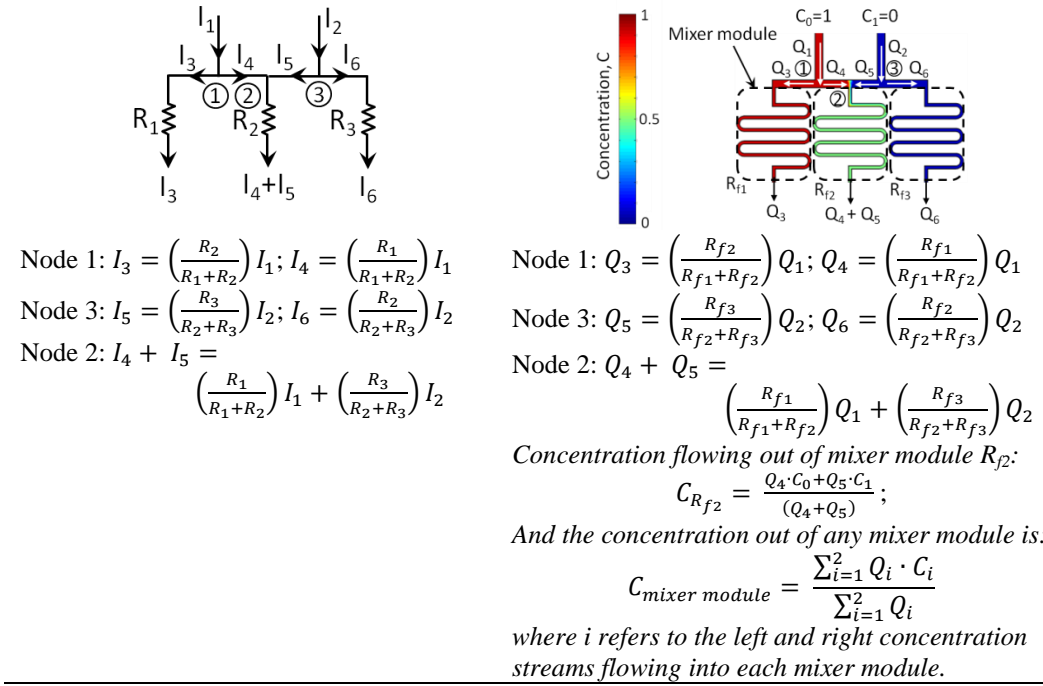
where $R_f = \left[\frac{12\mu L}{wh^3} \left\{ 1 - \sum_{i=1,3,5,\dots}^{\infty} \frac{192h}{i^5\pi^5 w} \tanh\left(\frac{i\pi h}{2w}\right) \right\}^{-1} \right]$ for rectangular microchannels. In cases where the channel aspect ratio, $\frac{h}{w} \rightarrow 0$, $R_f \approx \frac{12\mu L}{wh^3} [(1 - 0.63h)^{-1}]$. R_f is geometry dependent and is known as the hydraulic resistance.

Analogous to electric circuits, fluidic circuits can be dramatically simplified by hydraulic resistance, R_f , calculations (see Table 1.2). An electric circuit can be compared to a hydraulic circuit, where the electrical voltage, resistance and current, are respectively analogous to the hydraulic pressure drop, resistance and flow rate. Hydraulic circuits have been used in the direct evaluation of concentration profiles generated by sequential mixer networks- such as the “Christmas tree” design (Chung et al., 2005). An example of the use of the electrical-hydraulic resistance analogy in “Christmas tree” gradient generators is shown in Table 1.2. As illustrated in Table 1.2, the fluidic mixer networks produce hydraulic resistances which are analogous to the electrical resistance attributed to wires within electrical networks. The “Christmas tree” gradient generator shown in Table 1.2 illustrates the formation of a concentration gradient via sequential dilution of known input concentrations (C_0 and C_I) through a network of mixers. Downstream, the eluted streams experience fluidic lamination where adjacent concentration streams (from nodes 9 to 15) combine into a common reservoir. With such designs, the flow resistances of the horizontal channels are assumed to be negligible as compared to the vertical mixer channels. It is also assumed that the vertical mixer lengths are adequate to result in complete mixing of the two input concentrations. (Dertinger et al., 2001). With these assumptions applied, the resultant concentration of the solutes at the output streams is simply a factor of the downstream flow resistances, a concept termed here as concentration

division (Table 1.2). At each node, the flow rate splitting of the solute and diluent streams is determined by the relative hydraulic resistances downstream from the node. This is analyzed in a similar manner as current division in electrical circuits. Although concentration division is only shown for nodes 1 to 3 in Table 1.2, it is applicable to any of the 15 nodes within the gradient generator to determine the output concentrations from each mixer module.

Table 1.2 Electric- hydraulic analogy and its applicability in microfluidic gradient generators

Electric circuits	Hydraulic circuits
Ohm's law: $V = RI$ <i>where V=Voltage, R=electrical resistance and I=electrical current</i>	Hydraulic resistance equation: $\Delta P = R_f Q$ <i>where ΔP=Pressure drop, R_f=hydraulic resistance and Q=flow rate.</i>
Electrical network:  <p><i>Encircled numbers represent current nodes.</i></p>	Fluidic mixer network:  <p><i>Encircled numbers represent concentration nodes.</i></p>
Kirchoff current law: Node 1: $I - I_1 - I_2 = 0$ \vdots Node n: $\sum_{i=1}^n I_i = 0$ <i>where n is the total number of branches into or out of the node.</i>	Mass conservation: Node 1: $Q - Q_1 - Q_2 = 0$ \vdots Node n: $\sum_{i=1}^n Q_i = 0$ <i>where n is the total number of channels into or out of the node.</i>
Current division: <i>Applied at nodes 1, 2 and 3:</i>	Concentration division: <i>Applied at nodes 1, 2 and 3:</i>



One of the key benefits of analytical hydraulic circuits is the ease in which channel geometry (*i.e.* hydraulic resistance) can be designed to yield user-specified output concentrations. This presents a particularly easy method to design the gradient generator without the use of numerical stimulation tools or prior flow experiments. Although Table 1.2 illustrates the use of hydraulic circuit analysis that is specific to the “Christmas tree” gradient generator, such circuits can also be applied in the analysis of other designs of pressure-driven gradient generators (Atencia et al., 2012; Chau et al., 2011; Park et al., 2007). In most gradient generator designs involving pressure driven uni-directional fluid flow, the transport of solute concentrations can be simplified and analyzed as equivalent hydraulic circuits (Oh et al., 2012).

1.4.4 Mass transport in convection/ diffusion based gradient generators

The previous section shows how hydraulic circuit analysis is useful in designing and predicting the concentration of individual output streams in gradient generators such as the “Christmas tree” design. However, hydraulic circuit analysis does not account for the movement of solute species across adjacent output streams and does not describe the transport of solute species in the absence of pressure driven flow. The transport of a solute species within gradient generators occurs through diffusion and/or mass convection. This process is governed by the constitutive convection-diffusion (C-D) equation that superimposes the independent processes of convection and diffusion. By applying the conservation of mass to a control volume, the C-D equation for a solute species balances the rate of mass accumulation with the sum of convective mass flow ($\vec{v} \cdot \vec{\nabla} C$), diffusive mass flow ($D \nabla^2 C$) and the net rate of the species formation (R_g) (see equation [1.7] in Table 1.3). The velocity vector from the convective term, $(\vec{v} \cdot \vec{\nabla} C)$, is obtained from solving the previously introduced N-S equation for convective transport of solute species (see Table 1.1). The net rate of species formation, R_g , is usually present when there is a chemical reaction producing or consuming the solute species. This factor is omitted in the mass transport analysis of gradient generators as negligible chemical reactivity between the solute and diluting species is assumed. This assumption is valid in gradient assays for biological studies since most solutes: growth factors, cytokines or organic compounds, have negligible chemical reactivity with their diluents. The C-D equation also accounts for diffusion as the secondary mode of mass transport.

Diffusion of a single solute species in a diluent species is characterized by the diffusion coefficient, D . For instance, the concentration gradient formed due to the transport of fluorescein molecules (solute) in water (diluent) is determined by the diffusion coefficient of fluorescein molecules in water as described by Fick's first law of diffusion (Ahmed et al., 2010b). Fick's second law describes how mass transport via diffusion is non-steady and changes with time (Ahmed et al., 2010b). Central to the design of diffusion dominated gradient generators, Fick's first and second laws convey two general concepts on the diffusion process in the microfluidic domain. First, concentration gradients diffuse from regions of high concentration to regions of low concentration. And second, diffusion is a time evolving phenomenon which results in an equilibration between high concentration and low concentration regions.

Table 1.3 Overview of the use of convection-diffusion (C-D) equation in microfluidic-based mass transport

Constitutive C-D equation (binary diffusion within dilute mixtures)	$\frac{\partial C}{\partial t} + (\vec{u} \cdot \vec{\nabla} C) = D \nabla^2 C + R_g$ [1.7]
Microfluidics C-D equation ($Pé \gg 1$ and steady-state flow)	$\vec{u} \cdot \vec{\nabla} C = 0$ [1.8]
Microfluidics C-D equation ($Pé \ll 1$ and transient flow)	$\frac{\partial C}{\partial t} = D \nabla^2 C$ [1.9]

In mass transport analysis of gradient generators, it is often necessary to simplify the C-D equation such that flow characteristics of the device are adequately defined. This is usually performed via the analysis of the *Péclet* number ($Pé$). The $Pé$ number is a measure of the relative importance of convection to diffusion mass

transport (Deen, 1998). It is defined as the ratio between the characteristic velocity of convective flow, U_c and the characteristic velocity of diffusion, $\frac{D}{L_c}$:

$$Pé = U_c / \frac{D}{L_c} = \frac{U_c L_c}{D} \quad [1.10]$$

The $Pé$ number is often used as an indication of the relative order of magnitude between convective and diffusive transport processes. The $Pé$ number varies with the molecular diffusivity, D , of the chemical species and in the analysis of multiple chemical species, there exists more than a single $Pé$ number. Within the context of microfluidic gradient generators, the $Pé$ number is generally used to simplify the analysis of the convection-diffusion equation. When $Pé \gg 1$, the dominant mode of mass transport is convection and the diffusive mass transport term ($D\nabla^2 C$) can be omitted from the C-D equation. The C-D equation is further simplified when the steady-state assumption is applied to solve for the concentration field (see equation (E1.8) in Table 1.3). When $Pé \ll 1$, the dominant mode of mass transport is diffusion and the convective mass transport term ($\vec{u} \cdot \vec{\nabla} C$) is omitted from the C-D equation. In cases where convective and diffusive transport mechanisms are equally important, the C-D equation has to be solved in its full form by inserting the fluid properties and defining appropriate boundary/ initial conditions. Simplifications to the C-D equation can be achieved through appropriate reductions of the problem in terms of dimensions and/or directions (Deen, 1998). Analytical solutions to the C-D equation, with different mathematical simplifications applied, are frequently found in many mass transport textbooks (Ahmed et al., 2010b; Beta & Bodenschatz, 2011; Deen, 1998). However, in complex and multi-dimensional C-D transport problems, numerical methods are commonly applied to compute the velocity and concentration

fields formed within microfluidic gradient generators. In this respect, many papers (Boy et al., 2008; Hartin et al., 2010) and textbooks (Velve-Casquillas et al., 2010) provide details of the different numerical tools that are used to analyze microfluidic flow.

1.4.5 Shear stresses associated with mass transport in convective type gradient generators

In convective type gradient generators, the transport of concentration gradients depends on fluid flow velocity. During biological assays, the presence of flow velocities introduces shear stresses over cells residing on the fluidic channel bed. As such, convective type gradient generators have to be designed to provide cells with a physiologically relevant shear flow microenvironment, while achieving user-specified chemical concentration gradients (Shemesh et al., 2015). The maximum shear stress, τ_{\max} occurs at the microchannel walls and is determined in the following equation [1.11] (Deen, 1998). This equation is applicable for 2D microchannels where the characteristic length (L) is much smaller than the microchannel height (H) such $L/H \ll 1$.

$$\tau_{wss} = \frac{6\mu Q}{wh^2} \quad [1.11]$$

where τ_{wss} is the wall shear stress induced by the flow rate, Q , within a microchannel of height (h) and width (w). μ is the dynamic viscosity of the fluid flowing through the microchannel.

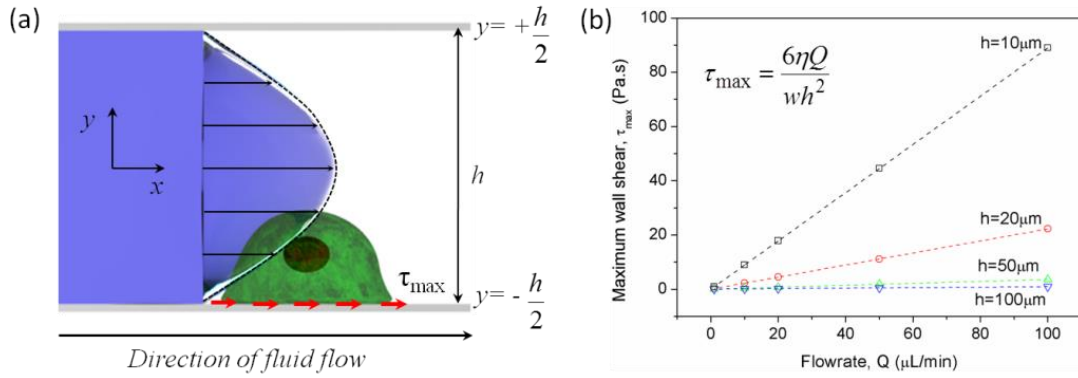


Figure 1.2 Shear stress in a microchannel: (a) Parallel plate flow induced shear stress on a cell residing on the bed of a microchannel. (b) Linear and proportional relationship between shear stress and flow rate. Change in maximum shear stress applied on cells when microchannel height, h is varied, for a fixed microchannel width of $w=1000\mu\text{m}$. The shear stress is plotted for water viscosity, $\mu=8.9\times 10^{-4}\text{ Pa}\cdot\text{s}$.

The velocity and dimensional parameters used in equation [1.11] is illustrated in Fig. 1.2(a). Equation [1.11] defines the linear and proportional relationship between shear stress and flow rate (*i.e.* an increase in flow rate results in a proportional increase in the shear stress induced on cells). The equation provides an estimate of the maximum shear stress applied on cells for cases where the height of microchannel, h , is at least one order of magnitude less than the microchannel width, w (*i.e.* $\frac{h}{w} < 0.1$). Fig. 1.2(b) plots the shear stress variation as channel height and flow rate are varied, for a constant channel width, w , of $1000\mu\text{m}$. Fig. 1.2(b) shows that an increase in microchannel height by one order of magnitude ($10\mu\text{m}$ to $100\mu\text{m}$) significantly reduces the shear stress applied on cells over a wide range of flow rates. As such, the selection of flow rates and microchannel geometry for gradient

generation should be carefully considered in order to recapitulate physiologically relevant shear conditions for cell studies.

1.4.6 Time scales associated with mass transport in gradient generators

The previous sections on mass transport introduced the basic concepts that form the foundation of concentration gradient formation in microfluidic devices. In those concepts, the analysis of the steady-state velocity and concentration fields includes time as an implicit variable. However, in actual gradient generation experiments, the time required to reach a steady-state or pseudo-steady state, as in the case of diffusion gradient generators, is finite and of importance. In biological studies, it is often important to have an indication of the time required to establish the concentration gradient- the characteristic time. The characteristic time provides an order of magnitude estimate of the time required for chemicals to form a stable concentration profile across a specified distance. The time scale of gradient generation is also important for determining the protocol, *i.e* “how” the biological experiment will be carried out (Gao et al., 2014). For instance, in cases where the time required for gradient stability is much longer than the response time of the cell assay, the cell would have to be introduced into the microfluidic device after a specified concentration gradient is formed. This prevents a convolution of cell response data- the cell response should be solely influenced by known concentration states, without any influence from unstable or transitional concentration states. In Table 1.4, the transport parameters and hence, characteristic time scales for different

types of gradient generators are summarized. The categorization of whether a gradient generator is diffusion or convection based is dependent on the $Pé$ number (as previously introduced in equation [1.10]).

Table 1.4 Overview of the characteristic time scales for microfluidic gradient generators

Gradient generator	Transport parameter	Characteristic time scales
Convection-based ($Pé > 1$)	Average velocity, U	$t_v = \frac{L_c}{U}$
Diffusion-based ($Pé < 1$)	Diffusion coefficient, D	$t_d = \frac{L_c^2}{2D}$

The characteristic time scale for microfluidic gradient generators is determined by the transport parameter and the characteristic length of the device. The transport parameter for convective type gradient generators is the flow velocity, U . The transport parameter for diffusive type gradient generators is the diffusion coefficient, D . The characteristic length, L_c , in time scale analysis is frequently chosen as the order of magnitude of distance in which the concentration gradient forms. Table 1.5 summarizes the typical operation characteristics of some convection-based and diffusion-based gradient generators used in biological studies of cell chemotaxis (Abhyankar et al., 2008; Jeon et al., 2002; Kothapalli et al., 2011; Lin et al., 2004) , migration/ wound-healing processes (Haessler et al., 2009; Haessler et al., 2011; Wang et al., 2004), cytotoxicity assays (Bang et al., 2004; Ziolkowska et al., 2010) and cell culture (Cimetta et al., 2010; Hung et al., 2005). The specific designs of convection-based and diffusion-based gradient generators are briefly described in Table 1.5 and explained in greater detail in the following section on gradient generator designs (see Fig. 1.3 to Fig. 1.7).

Table 1.5 Typical operation characteristics- flow velocity (U), characteristic length (L_c), *Péclet* number ($Pé$) and characteristic time (t_c) for gradient stabilization in convection and diffusion based gradient generators. Velocity values in parentheses are derived based on $\langle U \rangle = L_c/t_c$.

Reference	Type	U (mm s ⁻¹)	L _c (μm)	Chemical species	Pé	t _c (secs)
(Lin et al., 2004)	“Christmas tree”; <i>Convective</i>	0.38	350	Interleukin-8 ($D = 0.2\text{--}2.8 \times 10^{-10} \text{m}^2 \text{s}^{-1}$)	48- 665	0.92
(Jeon et al., 2002)	“Christmas tree”; <i>Convective</i>	1	500	Interleukin-8 ($D = 2.5 \times 10^{-10} \text{m}^2 \text{s}^{-1}$)	2000	0.5
(Walker et al., 2005)	“Christmas tree”; <i>Convective</i>	0.33, 6.67	500	FITC- dextran ($D = 8 \times 10^{-11} \text{m}^2 \text{s}^{-1}$)	2063, 41688	1.51, 0.07
(Walsh et al., 2009)	T-junction; <i>Convective</i>	1.7	350	Doxorubicin ($D = 2.5 \times 10^{-11} \text{m}^2 \text{s}^{-1}$)	23800	0.2
(Long & Ford, 2009)	T-junction; <i>Convective</i>	n/r	n/r	α- Methylasparate ($D = 8.6 \times 10^{-10} \text{m}^2 \text{s}^{-1}$)	20 to 154	n/r
(J. Y. Park et al., 2007)	Y-junction; <i>Convective</i>	0.22, 7.25	250	Polyethylene Glycol ($D = 5 \times 10^{-10} \text{m}^2 \text{s}^{-1}$)	3.63, 10.9	1.14, 0.03
(Qasaimeh et al., 2011)	2D pressure balance; <i>Convective</i>	2	1075	Fluorescein sodium ($D = 5 \times 10^{-10} \text{m}^2 \text{s}^{-1}$)	5602	0.4
(Atencia et al., 2009)	2D pressure balance; <i>Diffusive</i>	$<1.67 \times 10^{-3}>$	1500	Carboxyfluorescein ($D = 5 \times 10^{-10} \text{m}^2 \text{s}^{-1}$)	<1	9×10^2
(Du et al., 2009b)	1D flow balance; <i>Diffusive</i>	$<6.76 \times 10^{-3}>$	50000	FITC- dextran ($D = 1.7 \times 10^{-10} \text{m}^2 \text{s}^{-1}$)	<1	7.4×10^6
(Ahmed et al., 2010a)	1D gradient in hydrogel; <i>Diffusive</i>	$<0.98 \times 10^{-3}>$	1000	Fluorescein sodium ($D = 5 \times 10^{-10} \text{m}^2 \text{s}^{-1}$)	<1	1.02×10^3
(Ma et al., 2010)	1D gradient in 3D porous scaffold; <i>Diffusive</i>	$<4.76 \times 10^{-5}>$	1000	20% Fetal Bovine Serum (FBS) ($D = 2.35 \times 10^{-11} \text{m}^2 \text{s}^{-1}$)	<1	2.1×10^4
(Kothapalli et al., 2011)	2D gradient in collagen gel; <i>Diffusive</i>	$<5.00 \times 10^{-7}>$	900	Neurite-repellant slit-2 ($D = 5.1 \times 10^{-11} \text{m}^2 \text{s}^{-1}$)	<1	1.8×10^3
(Abhyankar et al., 2008)	3D gradient in agarose gel; <i>Diffusive</i>	$<7.78 \times 10^{-5}>$	2000 0	Epidermal growth factor (EGF) ($D = 3.5 \times 10^{-10} \text{m}^2 \text{s}^{-1}$)	<1	2.57×10^5
(Haessler et al., 2009)	3D gradient in collagen matrix; <i>Diffusive</i>	$<3.7 \times 10^{-5}>$	400	CCL19 chemokine ($D = 1.11 \times 10^{-10} \text{m}^2 \text{s}^{-1}$)	<1	1.08×10^4

n/r: not reported; n/a: not applicable

Time scale analysis is important in determining the mass transport mechanism used for gradient generation. Most application specific gradient generators select mass transport modes that produce the most physiological accurate gradients for the biological cells being studied (Shemesh et al., 2015). The different transport modes

result in vastly different characteristic times due to the range of values of the transport parameters. During microfluidic gradient generation, the typical flow velocities range from 10^{-7} to 10^{-2} m s⁻¹ while typical solute diffusion coefficients range from 10^{-8} to 10^{-11} m² s⁻¹. Table 1.5 shows that diffusive mechanisms are several orders of magnitude slower than convective mechanisms. As such, convective type gradient generators are widely adopted for dynamic control of concentration gradients; flow rate directly maneuvers the spatial delivery of concentration gradients. On the other hand, diffusive type gradient generators predominantly produce static concentration gradients in low shear environments. In addition, diffusive concentration gradients can be maintained at a pseudo-steady state for time intervals ranging from several minutes to hours, depending on the solute diffusivity. In particular cases where diffusive concentration gradients are sustained within hydrogels, high molecular weight solutes having a small diffusivity, D , results in concentration gradients that do not evolve significantly over the time scale of the experiment. By leveraging on this pseudo-steady state, a known concentration gradient can be sustained through periodic, rather than continuous fluid replenishment. Diffusion-based gradient generators are thus cost-effective platforms for performing biological experiments that involve expensive or limited reagent volumes. However, a caveat for diffusion-based gradient generators is its lack of applicability to chemical gradients consisting of small molecular sizes, which may saturate quicker than the intended assay duration.

Characteristic time scales also help in determining the appropriate temporal resolutions of fluidic control tools to be used. In general, most microfluidic gradient

generators rely on fluidic control tools to generate and maintain concentration gradients for biological experiments. Fluidic control tools such as syringe pumps, pressure pumps, peristaltic pumps and/or valves are commonly used in controlling fluid flow for microfluidic applications. Each of these flow control tools have temporal resolutions that limit the minimum response time for fluid flow control. Therefore, decisions on tool selection should be based on the intended time required for gradient generation. For instance, in convective type generators, on-chip integrated fluid control such as membrane microvalves/ micropumps- rather than external counterparts- are frequently used to ensure minimum response lag in dynamic gradient generation (Chen et al., 2012; Dai et al., 2010; Du et al., 2009a; Frank & Tay, 2013). On-chip microvalves and micropumps have extremely low dead volumes and can be integrated in direct vicinity to gradient generation chambers, thereby reducing flow response lag caused by tubing lengths. On the other end of the spectrum, diffusion-based generators transport gradients across larger time scales and seldom require rapid on-chip flow control. Many diffusion-based gradient generators utilize slow and passive tools to deliver concentration gradients. These include mechanisms such as electro-osmotic pumping (Park et al., 2009) and passive capillary pumping (Abhyankar et al., 2008; Berthier et al., 2010; Kim & Kim, 2010) of concentration gradients. The following section reviews how the previously discussed engineering aspects are used in gradient generator designs to study biological problems.

1.4.7 Types of gradient generator designs used in biological applications

1.4.7.1 Convective type gradient generators for investigating cell responses to chemical stimuli

Convective type ($Pé > 1$) gradient generators are frequently used to study the responses of cells that experience flow-induced shear stress in their native, *in-vivo* microenvironments. One of the most popular designs for convective type gradient generators is based on the integration of multiple mixer networks (the previously discussed “Christmas tree” design) (Jeon et al., 2002). The design, first developed by Jeon *et al.*, was used to generate a concentration gradient of hydrofluoric (HF) acid to etch a glass coverslip to depths proportional to the HF concentration gradients (Jeon et al., 2000). “Christmas tree” designs have since been used to study a plethora of biological phenomena due to its elegance in performing concentration dosing and gradient generation in a single device. The serial mixer networks within the “Christmas tree” design allow a single concentration of the solute/s to be serially diluted by diluent/s, into a range of concentration doses. The concentration doses that travel into the output chamber consequently form one-dimensional lateral gradients perpendicular to the direction of the flow. In biological studies, interrogated cells were inserted into the output chamber where the concentration gradient was formed. “Christmas tree” gradient generators have been used to study the dosing effect of chemical stimuli to adherent cells such as MCF-7 cells (Ruan et al., 2009), neural stem cells (Chung et al., 2005), MDA-MB-231 breast cancer cells (Saadi et al., 2006) and neutrophils (Lin et al., 2004). Recently, “Christmas tree” gradient generators

have been used in the study of motile, non-adherent bacteria suspensions (Englert et al., 2009; Englert et al., 2010), representing a paradigm shift in its application (Fig. 1.3(a)). “Christmas tree” gradient generators have predominately been used in studies related to adherent cells (Jeon et al., 2002; Lin et al., 2004; Wang et al., 2004). A study using “Christmas tree” gradient generators found that cell migration could be biased by the shear force induced by flow velocities and affect cell responses to concentration gradients (Walker et al., 2005). This bias would be exacerbated in the analysis of motile cells. However, a recent study on motile *E.coli* bacteria proposed that an additional control experiment, with reversed gradient directions could be used to quantify the flow- induced bias in chemotactic responses (Englert et al., 2010).

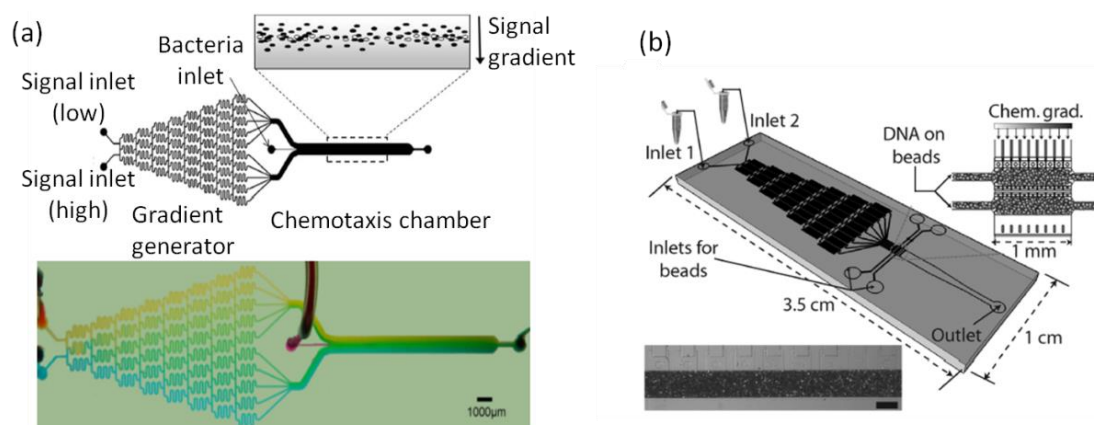


Figure 1.3 (a) “Christmas tree” gradient generators used in chemotaxis studies of *E. coli* RP437 cells in response to singular and competing chemoeffector concentrations (Englert et al., 2010). Figure reproduced with permission from the American Society for Microbiology. (b) “Christmas tree” gradient generators used to conduct parallel melting curve analysis of matched and mismatched DNA oligonucleotides (Russom et al., 2009). Figure reproduced with permission from John Wiley and Sons.

In a recent study, the “Christmas tree” generator’s ability to provide temporally stable chemical gradients was applied to the discrimination of SNPs within target DNA oligonucleotides (Russom et al., 2009). The gradient generator (shown in Fig. 1.3(b)) was used to produce the required concentration gradients of either urea or formamide. Through fluorescent detection of the allele specific probe intensity during exposure to urea or formamide gradients, the degree and speed of target DNA denaturation (and associated decay of fluorescent intensity) was observed. The rate of DNA denaturation was directly correlated to the presence of a Single nucleotide polymorphism (SNP) in the target DNA. By using gradient generators to produce precise doses of urea or formamide, the denaturation of DNA duplexes could be analyzed chemically instead of thermally- abrogating the need for heating control

elements that are frequently used in melting curve analysis of DNA. In addition to one-dimensional gradient generation, the “Christmas tree” design has also been employed in a high-throughput manner to produce two-dimensional concentration landscapes in cell culture microwells (Hung et al., 2005; Lee et al., 2006). Fig. 1.4(a) (right) depicts how one-dimensional gradient generators can be redesigned to produce two-dimensional concentration landscapes.

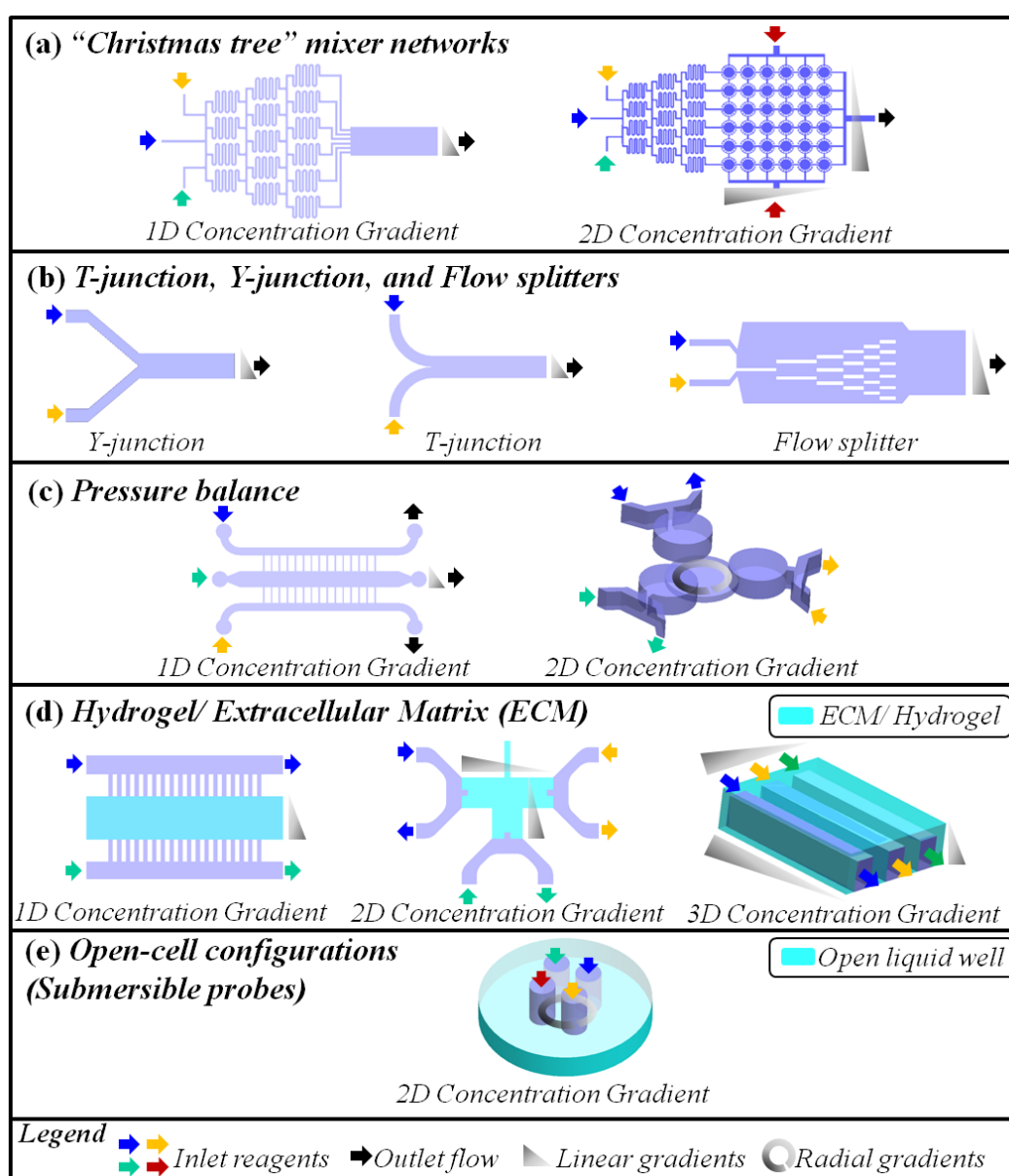


Figure 1.4 Microfluidics based gradient generator designs: (a) (*left*) “Christmas tree” design for 1D (Jeon et al., 2000) and (*right*) 2D gradient generation (Hung et al., 2005); (b) (*left*) Y- junction (Atencia et al., 2012), (*centre*) T-junction (Long & Ford, 2009) and (*right*) flow splitter designs (Irimia et al., 2006); (c) (*left*) 1D gradient generation and (*right*) 2D gradient generation through pressure balance designs; (d) Molded gels for (*left*) 1D (Ahmed et al., 2010a), (*centre*) 2D (Kothapalli et al., 2011) and (*right*) 3D gradient generation (Haessler et al., 2011), and (e) Submersible microfluidic probes (Qasaimeh et al., 2011).

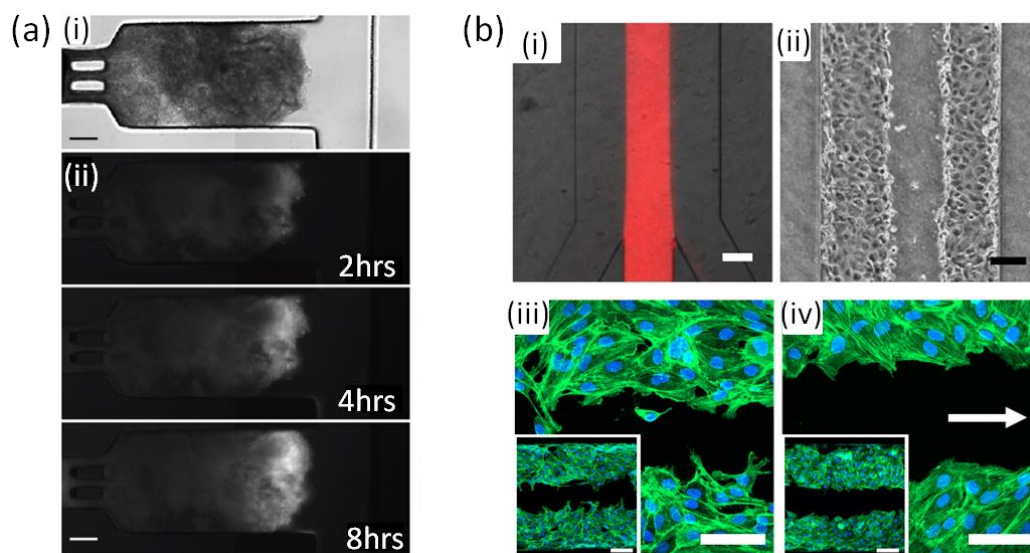


Figure 1.5 (a) (i) T-configuration design that produces (ii) drug gradients along the length of an isolated cancer tumour mass. (Walsh et al., 2009). Figures reproduced with permission from the Royal Society of Chemistry. (b) (i) Y-configuration device used for performing wound healing assays. Centre microchannel of the Y-device transports a stream of trypsin that detaches cells previously adhered to the channel substrate to artificially create a wound (ii). (iii) & (iv) show actin filament stains of

endothelial cells under (iii) quiescent and (iv) shear flow conditions (Meer et al., 2010).

Other convective type gradient generators have also been reported. These generators utilize different microchannel geometries and configurations to generate concentration gradients. More common designs include T or Y channel configurations (Fig. 1.4(b)) to produce concentration gradients that form interdiffusion concentration zones that are perpendicular to the flow field (Long & Ford, 2009; Meer et al., 2010; Walsh et al., 2009). T-configuration gradient generators (Fig. 1.5(a)) have been utilized to recreate the microenvironment surrounding tumour masses (Walsh et al., 2009). In an effort to study the effect of a chemotherapeutic drug (Doxorubicin) and anti-cancer bacteria (*S. typhimurium*) on solid tumour masses, Walsh *et al.* developed a multipurpose T-junction microfluidic device. The device was used to entrap and grow tumour masses; linear gradients of nutrients and drugs were generated and exposed to the isolated tumour mass (Walsh et al., 2009). The T-junction generator produced a stable drug concentration gradient that could be sustained for 45 hours, demonstrating the use of convective type generators in extended biological studies. Recently, van der Meer and co-workers have also demonstrated an innovative method of performing wound healing assays through the use of a Y-junction gradient generator (Meer et al., 2010) (Fig. 1.5(b)). The Y-junction generator consisted of three input channels that merged into a main fluid stream. A confluent layer of Human umbilical vein endothelial cells (HUVECs) was first cultured on the bed of the Y-junction gradient generator. In order to conduct a wound-healing assay, a “wound” was simulated within the layer of HUVECs by

applying a stream of trypsin protease. This trypsin stream was enveloped by parallel streams of cell medium. HUVECs that were exposed to the trypsin stream lost their adhesion to the channel surface and were subsequently washed away, leaving behind a “wound”. Using this device, the authors were able to generate a “wound” and subsequently apply a growth factor (VEGF₁₆₅) gradient to study HUVEC migration vis-à-vis wound-healing (Meer et al., 2010). Compared to conventional wound-healing assays such as the transwell cell migration assay, the microfluidic assay demonstrated temporally stable gradients and tunable cell shear stresses that could be used to closely mimic *in-vivo* physiological conditions (Meer et al., 2010).

The transport dynamics of convective type gradient generators are also extremely amenable to single cell studies. In convective type gradient generators, flow rates in parallel concentration streams can be dynamically tuned to focus on single cells. This typically involves a Y junction design with a minimum of three inlet flow channels. The flow of solutes in the middle stream is enveloped by flow from parallel diluent streams; this focuses the width of solute stream. The width of the solute stream can be hydrodynamically focused to single cell resolutions of several microns, by controlling the comparative flow rates of the solute and diluent streams (Nguyen, 2012). Y junction gradient generators have been used to study isolated cell responses to dynamic chemical stimuli (Lucchetta et al., 2005; Rosa et al., 2012; Takayama et al., 2003; Tong et al., 2012). Control of gradient generation on the length scale of single cells (~1-100µm) is simple in microfluidic channels as the transport of concentration streams occurs in a laminar manner. Laminar flow allows the direct control of diffusion between parallel concentration streams, without

the presence of chaotic advection that is dominant in macroscale flows. In a similar manner, the length scales of microfluidic gradient generators also shorten the time to deliver or move concentration gradients- an important feature in mimicking *in-vivo* biological states.

1.4.7.2 Convective type gradient generator designs for studying cell responses to pulsatile and temporal stimuli

Convective type gradient generators that are capable of delivering pulsatile biomolecular gradients are elegant solutions to mimicking dynamic signaling processes in cell microenvironments. In these microenvironments, pulsatile variations in biomolecular gradients regulate cell functions and are pivotal in maintaining homeostasis within a biological system. An example of this in vertebrate organisms is the homeostatic regulation of blood glucose levels by cells within the pancreas. Pancreatic islets (a group of cells within the pancreas) secrete multiple peptides, and hormones such as somatostatin, glucagon and insulin. Disrupted insulin secretion is a sign of the onset of type II diabetes mellitus, and studies related to deciphering the causes of impaired insulin secretion are of clinical importance. To gain insight into the dynamics of *in-vivo* insulin secretion, the oscillatory release of intracellular calcium ions (Ca^{2+}) by pancreatic islets, in response to oscillatory glucose concentrations has been studied using gradient generators (Dishinger et al., 2009; Zhang et al., 2011; Zhang et al., 2010). *In-vivo*, the release of intracellular Ca^{2+} is followed by insulin secretion and it is commonly used as an ionic marker of insulin secretion. In the report by Zhang *et al.*, a Y-junction mixer device (shown in Fig.

1.6(a)) delivered pulsatile glucose concentrations at frequencies ranging from 0.0033 Hz to 0.0056 Hz to elicit the release of intracellular Ca^{2+} from the islets (Zhang et al., 2010). Their temporal gradient generator produced glucose concentration frequencies that were similar to *in-vivo* glucose oscillations. On-chip pumping frequencies and mixer channel lengths (that act as a low-pass frequency filter) were optimized to produce glucose concentration levels that were minimally attenuated and yet, retained *in-vivo* pulse frequencies. Through optimization of the generator's frequency characteristics, Zhang et al. found that the release of intracellular Ca^{2+} by single pancreatic islets closely followed the generated glucose concentration signals with frequencies of 0.0056Hz. This was further demonstrated by applying an abrupt 180° phase shift (time shift of half the cycle time, i.e. $t=0.5*(1/0.0056)$) in the generated glucose concentration signal. Islets released Ca^{2+} concentrations that registered a time shifted response, corresponding to the time shift in glucose concentration signals. Further studies by Zhang *et al.* have also yielded evidence that heterogeneous islet populations- which resemble *in-vivo* states even more closely than single islets- released intracellular Ca^{2+} in synchrony to glucose concentration frequencies of (Zhang et al., 2011). In such studies, gradient generators were used to provide temporally precise concentration landscapes for quantitative investigations of complex and dynamic biological systems.

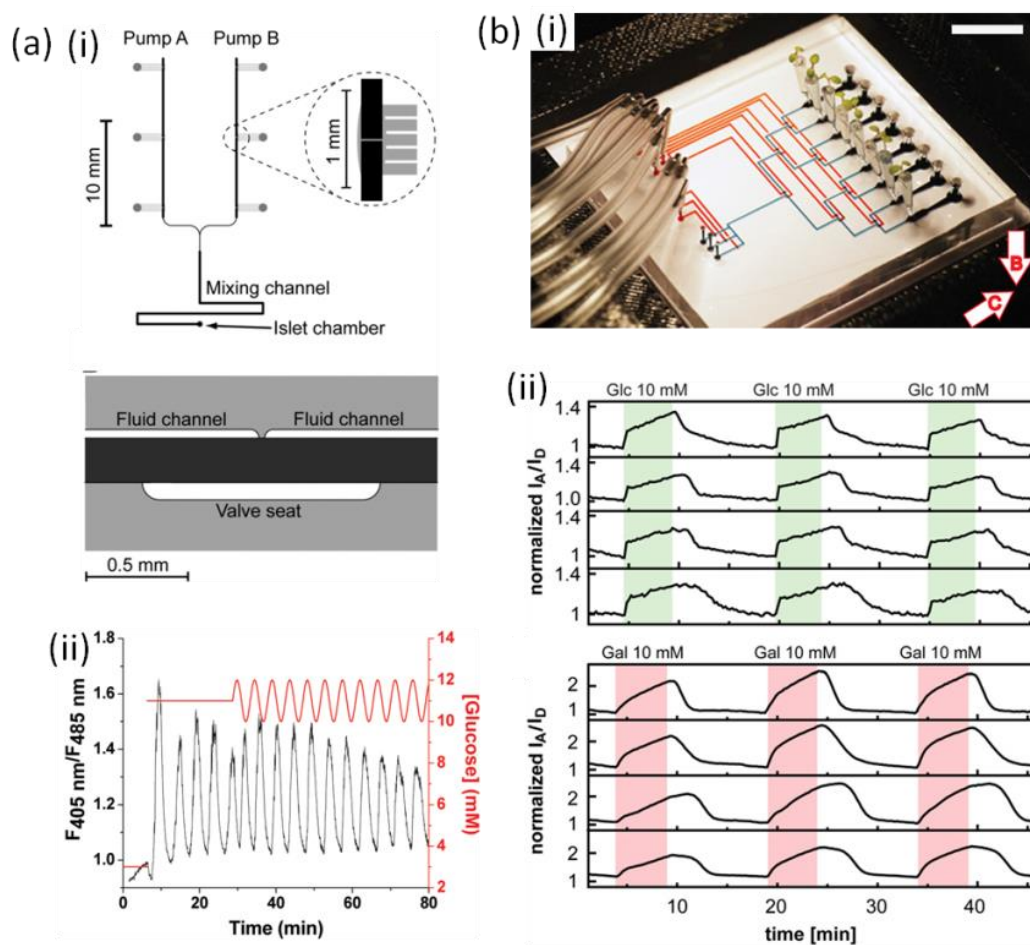


Figure 1.6 (a) (i) Microvalve embedded device for generating pulsatile concentration gradients and (ii) Increase in glucose concentrations from 3mM to pulsing concentrations with a mean of 11mM (red line) applied to entrain intracellular Ca^{2+} oscillations from single islets of Langerhans. Reprinted with permission from (Zhang et al., 2010). Copyright (2010) American Chemical Society. (b) (i) Rootchip device used to incubate *Arabidopsis thaliana* root seedlings and expose them to (ii) temporal concentration gradients of glucose (Glc) and galactose (Gal) .

Recently, microfluidic platforms have emerged as powerful tools for the study of entire organisms (Chung et al., 2011; Hulme et al., 2010) or part of tissues/ organs (Crane et al., 2010) on the size order of several millimeters. The microfluidic

platforms are often fabricated with larger culture wells that are flanked by microchannels which deliver the reagents of interest at different concentration levels. These microchannels are designed to deliver concentration gradients, dynamic or otherwise, across segmented areas or the entire area of the large cell culture zone. Dynamic gradient generators have been used in “large-scale” biological studies involving worms (Dirk & Cornelia, 2011), mammalian embryos (Heo et al., 2010), and even an entire plant organ (Grossmann et al., 2011; Meier et al., 2010). In the RootChip designed by Grossmann *et al.* (shown in Fig. 1.6(b)), *Arabidopsis thaliana* roots were integrated into a microfluidic device to study root metabolism in response to pulses of 10mM glucose (Glc) or galactose (Gal) (Grossmann et al., 2011). The Rootchip provided a platform to cultivate miniature *Arabidopsis* seedling roots of ~ 5mm in length, and to perform subcellular observations of cystolic Glc and Gal expression during dynamic switching of Glc and Gal concentrations in the root’s external environment. After performing separate experiments that exposed seedling roots to pulses of either Glc or Gal, Grossmann *et al* found that cystolic Glc accumulation and elimination was notably faster than that of Gal - suggesting differences in the metabolic pathways of these two types of sugars (Grossmann et al., 2011).

Other gradient generators have also been designed to study the adaptation characteristics of whole organisms to dynamic chemical changes in their extracellular environment (Dirk & Cornelia, 2011; Nagai et al., 2010). In the report by Dirk and Cornelia, the behavioural dynamics of *Caenorhabditis Elegans* (*C. Elegans*) nematodes were observed in response to odor gradients and odor pulses

within a microfluidic gradient generator (Dirk & Cornelia, 2011). *C. Elegans* are frequently used as model organisms for animal development (Sulston, 2003) and neuronal studies (Brenner, 1974). Because these organisms are small (~1mm in length), PDMS microfluidic platforms serendipitously provide viable whole-animal incubation environments along with the dynamic chemical microenvironments required for biological studies. Based on the study by Dirk and Cornelia, new locomotion patterns of *C. Elegans* were observed in response to controlled temporal pulses of odor concentrations. In this study, pillar embedded incubation chambers were fabricated to resemble the native soil conditions of *C. Elegans*, recapitulating physiologically relevant microenvironments within the gradient generator. This aspect was lacking in earlier agarose-based studies (Dirk & Cornelia, 2011). Such behavioral biology investigations on miniature organisms are increasingly being performed on microfluidic platforms. Dynamic gradient generators are expected to play a key role in recapitulating dynamic microenvironments in emerging “large scale” biological studies.

1.4.7.3 Gradient generator designs for low shear biological experiments

Diffusion type (with $Pe < 1$) gradient generators are commonly used in low shear biological studies to prevent the exposure of non-native shear stresses on cells. Cells that experience shear stresses which are not present in their native environments have been shown to respond differently to chemical gradients, as compared to *in-vivo* cells (Walker et al., 2004). To this end, diffusion-based gradient

generators have been designed to leverage on the diffusive transport of chemicals in the absence of flow velocities and thus large hydrodynamic shear stresses. In diffusion type gradient generators, porous materials are commonly used to form concentration gradients between high concentration sources and low concentration sinks (see Fig. 1.4(d)). Porous materials such as hydrogels (containing extracellular matrix proteins), matrigel and agarose are frequently used in gradient generators to mimic the cellular microenvironments within the extracellular matrix. Diffusion-based gradient generators based on such materials have been tuned to contain multiple chemical species (Hamid et al., 2010; Keenan et al., 2006; Suri & Schmidt, 2010) and biophysical cues (Connelly et al., 2010; Guilak et al., 2009; Kilian et al., 2010; Tripathi et al., 2009), thereby mimicking the *in-vivo* microenvironment of specific cell types. Microfluidic gradient generators containing gel materials have been designed to test a single cell population with a range of drug species or drug concentrations (Abhyankar et al., 2008; Ahmed et al., 2010a; Cheng et al., 2007; Haessler et al., 2009; Haessler et al., 2011; Ricart et al., 2011; Vazquez & Paull, 2010). In these studies, gel-based gradient generators were chosen to conserve the autocrine and paracrine factors released by the cell population- autocrine, and paracrine factors may be differentially regulated at different combinatory drug concentrations and are therefore, of importance in drug development studies (Paguirigan & Beebe, 2008). Gradient generators incorporating gel materials provide a platform to perform biological experiments faster and more controllably as compared to conventional gel-based assays due to the miniaturization of channel geometries.

Apart from simpler designs involving porous gels, other microfluidic designs have recently been designed to deliver concentration gradients from balance flow across multiple chemical sources (see Fig. 1.4(c)). By balancing the fluid pressure between multiple concentration sources and sinks as illustrated in Fig. 1.7(a), overlapping diffusive gradients of multiple chemical species have been achieved (Atencia et al., 2009; Morel et al., 2012). Pressure balance (PB) within a diffusion chamber can be maintained by decoupling source flow rates around a static concentration sink. Alternate source flows at equivalent flow rates can be flowed into a static concentration sink, thereby setting up a low or no shear concentration gradient environment. Conversely, PB may also be achieved along microchannels by matching the flow rates of cross flowing source and sink channels. Such device configurations reduce the flow shear of the gradient forming microchannel by the destructive superposition of flow shear present in each opposing channel. PB gradient generators have been used to provide sustained chemical gradients for biological assays that lasts several hours (Brett et al., 2012; Cimetta et al., 2010). Thus far, PB gradient generators have been used in low shear biological assays to study axon guidance in neurons (Queval et al., 2010), stem cell differentiation (Park et al., 2009) and chemotaxis of highly motile non-adherent cells (Atencia et al., 2009). Atencia and co-workers demonstrated the formation of a 2D diffusive concentration gradient through a balance of input flow pressures between three opposing flow inlets, (Fig. 1.7(a)). The PB scheme improves the dynamic response of diffusive gradients, as diffusive gradients often require long durations for stabilization. Dynamic chemotaxis of *Pseudomonas aeruginosa* was demonstrated by periodic switching of glucose sources within rotations of approximately 45 minutes

(Atencia et al., 2009). Diffusion type generators that utilize PB schemes are attractive alternatives to convection type generators as they allow a compromise to be reached between fast gradient stabilization and low shear flow velocities.

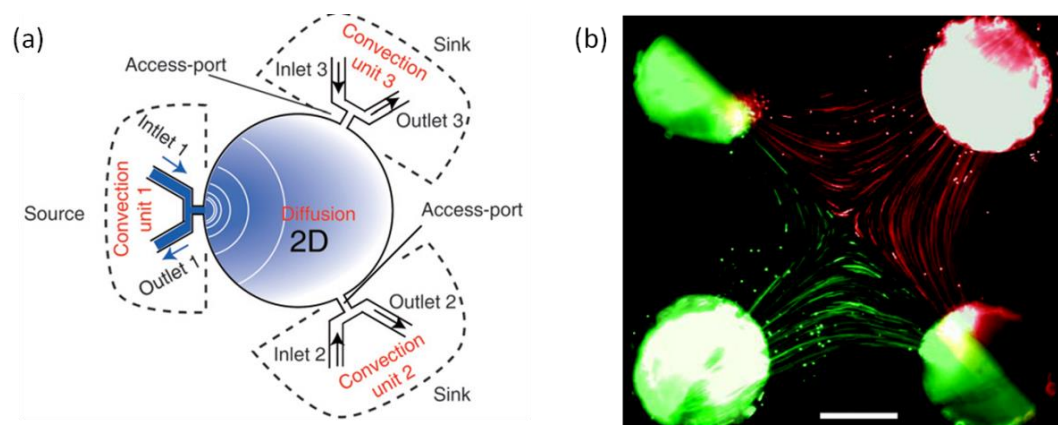


Figure 1.7 (a) The “microfluidic palette” that provides spatiotemporal of overlapping concentration gradients for bacteria chemotaxis experiments (Atencia et al., 2009). (b) Fluorescent bead images highlighting the stagnation point created by the “microfluidic probe” to produce a binary concentration gradient (Qasaimeh et al., 2011).

Furthermore, PB schemes have also been demonstrated in open chamber configurations (Fig. 1.4(e)) that are easily amenable to biological experiments involving large tissue samples (Juncker et al., 2005; Qasaimeh et al., 2011; Queval et al., 2010). Juncker *et al.* introduced the concept of a microfluidic probe (MFP) that generated overlapping concentration gradients by leveraging on Hele-Shaw flows between the MFP and an adjacent glass slide. During biological experiments, the cells/ tissues under interrogation would be affixed onto a glass slide that was separated from the MFP by several microns. Diffusion gradients are generated across

the stagnation point that resulted from balancing the cross-flow of two injection and aspiration ports. Using the MFP, successful microperfusion of Hippoorganotypic brain slices to low shear, fluorescent dextran gradients were demonstrated in open chambers (Queval et al., 2010). PB gradient generators are unique as they bypass the longer gradient establishment durations of hydrogel, agarose or matrigel diffusion type gradient generators. At the same time, PB gradient generators provide low or no shear environments for cells located at fluid stagnation wells. In addition, PB designs prevent time evolving concentration gradients that are prevalent in diffusive mass transport through porous materials. In PB gradient generators, sources and sinks are in continuous flow, thereby preventing the depletion of molecules in the sources and the accumulation of molecules in the sinks. This circumvents the time evolving nature of diffusion-based mass transport in gel-based diffusion type gradient generators.

Hitherto, diffusion type gradient generators have been widely used in low shear biological assays. While most diffusion-based gradient generators rely on gel-like materials to form diffusive gradients, new designs have been introduced to provide improved dynamic control of diffusive gradients. New designs based on pressure balance greatly improve the ability of diffusion-based generators to engineer dynamically controllable and stable gradients. Another class of gradient generators has been specifically designed for low shear, yet dynamic, biological experiments. These gradient generators utilize convection-based designs to quickly generate concentration gradients and include device features that shield cells from the shear flow environment (Atencia et al., 2012; VanDersarl et al., 2011; Zheng et al., 2012).

Typical designs include a high shear flow zone in which concentration gradients are generated, and a low shear flow zone with features such as deep wells (Hung et al., 2005; Wang et al., 2008) or porous membranes (VanDersarl et al., 2011). These features block high flow velocities but allow upstream chemical concentrations to diffuse to the cells. Convective type “Christmas tree” gradient generators with deep micro-well reservoirs, as depicted in Fig. 1.8(a), have been used to culture and shield neuronal cells from the effects of shear flow (Wang et al., 2008b). Neuronal cells that were seeded in the 100 μ m deep stagnation wells experienced negligible flow shear stresses as solute concentrations were delivered to cells via convective flow. Flow shear shielding of cells within the “Christmas-tree” gradient generators has also been demonstrated through the integration of a flow restricting nano-porous membrane above the gradient delivery chamber (see Fig. 1.8(b)) (VanDersarl et al., 2011). Cells that are seeded on the nano-porous membrane experience negligible flow shear from the underlying convective flow. These devices highlight the use of convective type gradient generators in low shear biological experiments requiring better temporal resolutions than that achieved by diffusion-based gradient generators.

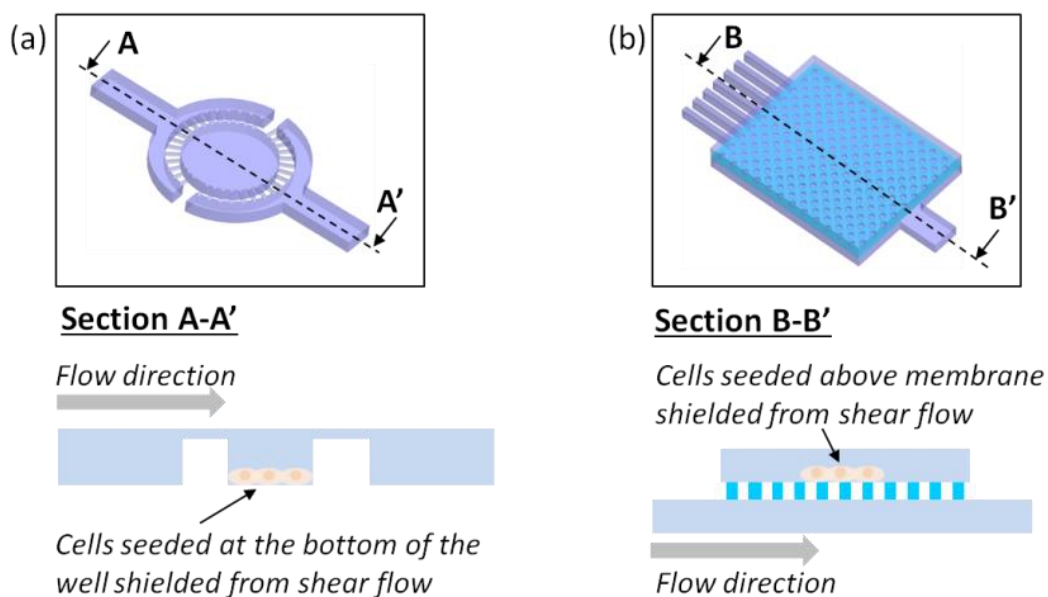


Figure 1.8 Shear flow shielding by seeding cells in (a) deep microwells (Hung et al., 2005; Wang et al., 2008) or (b) on porous membranes (VanDersarl et al., 2011).

1.4.8 Summary

Microfluidic concentration gradient generation overcomes the shortcomings of conventional macroscale devices used in cell studies. Most notably, microfluidic gradient generators have been employed to study biological processes, with unprecedented spatio-temporal resolutions. While gradient generator designs seem to be innately driven by application needs, this research space is still in its early stages, with more technological advances to be leveraged from microfluidics. In particular, microfluidics can be used to realize the manifestation of stable concentration gradients, within short time scales, in a low flow shear environment. Fig. 1.9 shows a summary of the shear stresses induced during concentration gradient stabilization in the various types of microfluidic concentration gradient generators.

Based on the summary of temporal and flow shear characteristics within the various gradient generator types, several insights can be gleamed. Firstly, long durations for gradient steady-state are hallmarks of diffusion –based gradient generators, and the use of these generators usually do not entail flow- induced high shear stresses. Secondly, diffusion and convection gradient generators sit at opposite spectrums of each other- convection-based gradient generators tend to require short durations to reach gradient steady-state but also induce higher flow-induced shear stresses. Last and most notably, there is currently a lack of microfluidic technologies

which address fast gradient stabilization, without the generation of flow-induced high shear stresses. These temporal and shear stress characteristics would be ideal in dynamically precise studies involving moving and unaffixed cells. Furthermore, current gradient generators do not allow the concentration gradients or landscapes to be moved, in a low shear manner, in response to real-time experimental observations. In this respect, pressure-balance gradient generators are good demonstrations of how faster gradient stabilization durations can be reached without inducing higher flow-induced shear stresses. However, work in this area has been extraordinarily lacking and further study is required to present a novel solution that can address fast gradient stabilization without inducing flow-induced high shear stresses during cell studies.

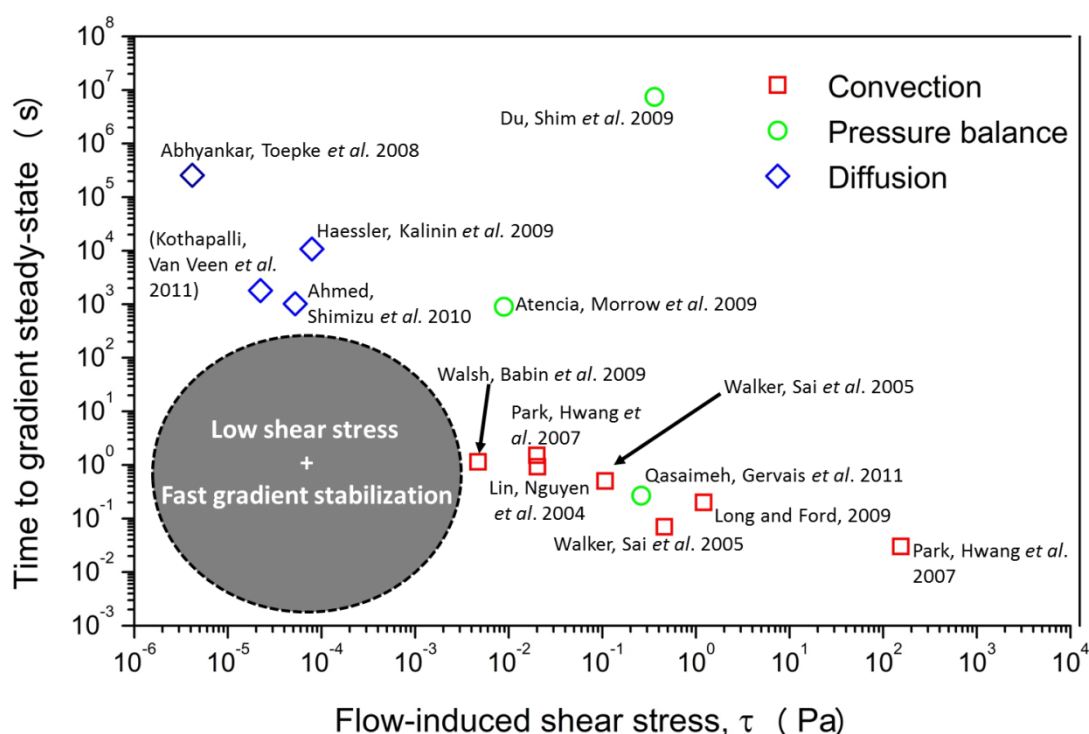


Figure 1.9 A summary of temporal and shear stress characteristics in convection, pressure- balance and diffusion microfluidic gradient generators. Grey circle covers

the void in concentration gradient generators which can quickly stabilize concentration gradients, while maintaining low shear stresses.

2 Theoretical Modelling of Convective-Diffusion Mass Transport in Stagnation Flow Concentration Gradient Generation

This chapter is split into six sections. Section 2.1 introduces the device geometry used to generate stagnation flow and the operating flow conditions. Section 2.2 describes the governing equations associated with fluid flow and concentration species transport during concentration gradient generation across the stagnation flow. Following which, section 2.3 provides a simplification of these equations and boundary conditions to gain physical insights into the mass transport processes occurring within the device. Section 2.4 introduces the Navier-Stokes equation used to map velocity and concentration field within the two-dimensional device geometry. This last section also describes the numerical methods and boundary conditions used to solve for the velocity and concentration fields within the two-dimensional device geometry, along with the calculations used to determine the wall shear stress.

2.1 Introduction

Rapid mass transport, under low shear stress conditions is an intractable problem in many microfluidic gradient generator devices. Rapid transport of concentration species relies on fast flow velocities yet increases in flow velocities induces an increase in shear stresses. In this project, it was hypothesized that the characteristics of stagnation flow could be used to reconcile the contradicting parameters of fast mass transport and low flow- induced shear stress. Stagnation

flows are flow fields that exist around singularities known as stagnation points. In theory, stagnation points are points where the local flow velocity is zero. While fluid far from the stagnation point can move rapidly, fluid velocity near the stagnation point drops drastically, resulting in the formation of a velocity well. In this sense, concentration species can be transported quickly to the stagnation point while the velocity well encircles a low shear flow environment.

Stagnation flow in microfluidics has predominantly been demonstrated in cross-slot devices (shown in Fig. 2.1 (a)). Within the cross-slot device, the stagnation flow is formed in the intersection of the orthogonal microchannels as fluid streams from opposite directions converge and exit the outlets. In this thesis, the conventional cross-slot device was modified to accommodate more than one concentration source-sink pair. As shown in Fig. 2.1 (b), the MCS device consists of four separate delivery channels that transport fluid flow into the centre stagnation flow chamber via narrow diffusion channels. With the modified cross-slot design, there are four inlets and four outlets, allowing the formation of binary and combinational concentration gradients across the stagnation flow.

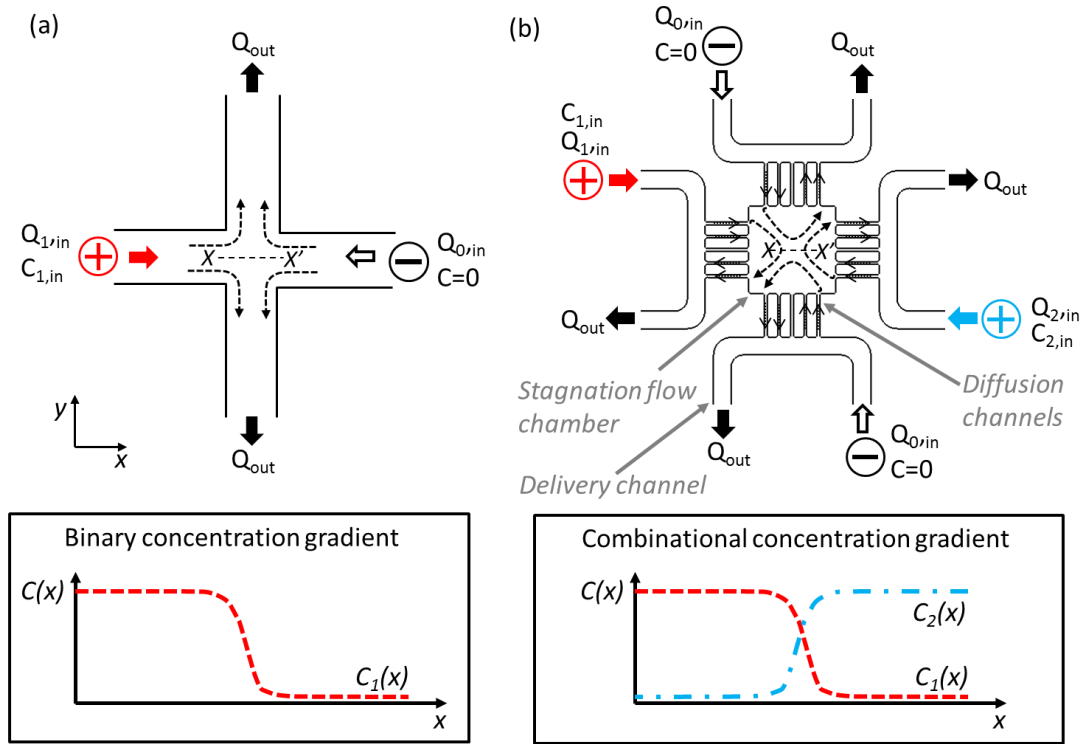


Figure 2.1 (a) Conventional cross-slot device and (lower) concentration profile of the binary concentration gradient formed across line X-X'. (b) Modified cross-slot (MCS) device designed in this thesis consists of a main stagnation flow chamber that is linked to wide delivery channels via several narrow diffusion channels. (lower) Concentration profile of combinational concentration gradients formed across line X-X'.

In order to characterize the transport of concentration species across the flow, the governing equations for conservation of mass and conservation of momentum have to be solved first to derive the flow field within the MCS device. Subsequently, the flow field can be coupled to the convection- diffusion equation to solve for mass transport across the stagnation flow.

2.2 Governing equations

This section introduces the main parameters that influence the physics of stagnation flow and the transport of chemical species through diffusion and convection. This first sub-section describes the physics that govern fluid motion while the second sub-section covers the physics that govern mass transport phenomena that occurs during diffusion and convection.

2.2.1 Equations that govern fluid motion

Stagnation flow belongs to a unique class of flows that result in the formation of one or several stagnation points within its flow pattern. Such flows was first demonstrated and quantified by Taylor (Taylor, 1934) using a four-roll mill apparatus to show how droplets break up in a purely extensional flow. Later experiments have since shown that such stagnation flows can be broadly categorized into three types: extensional, shearing and rotational (Astarita, 1979; Hudson et al., 2004; Lee et al., 2007). A common feature of each of these flow types is the presence of a stagnation point within the flow pattern. In stagnation flows of incompressible fluids, the velocity field, \vec{v} , follows that of a linear flow such that:

$$\vec{v} = \Gamma \cdot \vec{x}_i \quad [2.1]$$

where \vec{v} is the velocity field, Γ is the flow type tensor and \vec{x}_i is the position vector.

The flow-type tensor classifies the type of linear two-dimensional flow, *i.e.* whether the flow type is extensional, shearing or rotational. It is defined as (Marrucci & Astarita, 1967):

$$\Gamma = \frac{\dot{\epsilon}}{2} \begin{bmatrix} 1 + \xi & 1 - \xi & 0 \\ -(1 - \xi) & -(1 + \xi) & 0 \\ 0 & 0 & 0 \end{bmatrix} \quad [2.2]$$

where $\dot{\epsilon}$ is the flow strain rate and ξ is the flow type parameter that defines the relative effects of strain and vorticity in the linear flows (Hudson et al., 2004).

The flow type parameter is defined as (Marrucci & Astarita, 1967):

$$\xi = \frac{|\bar{E}| - |\bar{\Omega}|}{|\bar{E}| + |\bar{\Omega}|} \quad [2.3]$$

where $|\bar{E}|$ is the eigenvalue of the deformation tensor and $|\bar{\Omega}|$ is the eigenvalue of the vorticity tensor. The deformation tensor describes the local rate of deformation between two neighbouring material points in a fluid undergoing rigid-body rotation and is defined as:

$$\bar{E} = \frac{1}{2} \left[\bar{\nabla} \vec{v} + (\bar{\nabla} \vec{v})^t \right] \quad [2.3a]$$

where $\bar{\nabla} \vec{v}$ is the velocity gradient.

The vorticity tensor describes the local rate of rotation of a fluid element undergoing rigid-body rotation and is defined as:

$$\bar{\Omega} = \frac{1}{2} \left[\bar{\nabla} \vec{v} - (\bar{\nabla} \vec{v})^t \right] \quad [2.3b]$$

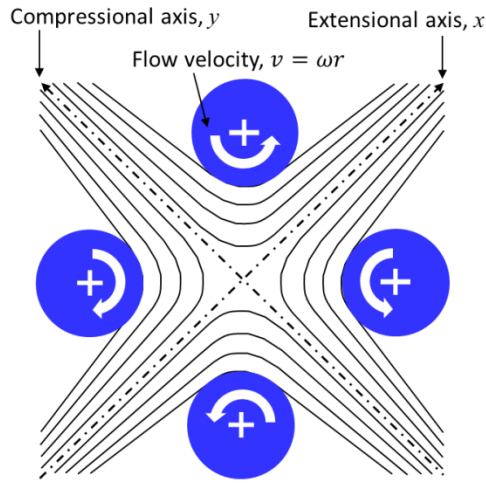
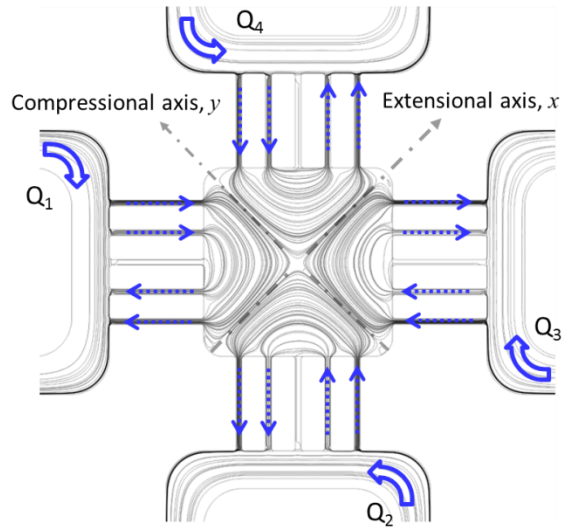
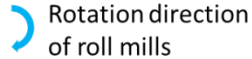
The flow type parameter, ξ , classifies linear flows based on the relative eigenvalues of the deformation tensor, $|\bar{E}|$ and the vorticity tensor, $|\bar{\Omega}|$. The flow type parameter has a range of $-1 \leq \xi \leq 1$ and categorizes the following linear flow types:

For purely extensional flow where $|\bar{E}| \gg |\bar{\Omega}|$; $\xi \rightarrow 1$

For purely rotational flow where $|\bar{E}| \ll |\bar{\Omega}|$; $\xi \rightarrow -1$

For simple shear flow where $O(|\bar{E}|) \sim O(|\bar{\Omega}|)$; $\xi \rightarrow 0$

Stagnation flow that is produced within the MCS device replicates the extensional flow (i.e. $\xi = 1$) that was first demonstrated by Taylor's four roll mill experiments (Taylor, 1934). The similarities between the flows produced by the four roll mill apparatus and the microfluidic MCS device are highlighted in Fig. 2.2. In Taylor's experiments, an extensional flow forms when each of the four roll mills are rotated at equivalent angular velocities, ω . As the roll mills turn, they move their surrounding fluid at a velocity of $v = \omega r$, where r is the radius of the roll mills. The fluid streams surrounding each of the roll mills converge, and result in the formation of a stagnation point at the intersection of the compressional and extensional axis shown in Fig. 2.2. In a similar manner, as shown in Fig. 2.2, the flow patterns within the MCS main chamber replicates the extensional flow pattern formed in four roll mill experiments when $Q=Q_1=Q_2=Q_3=Q_4$. One key difference between the four roll mill apparatus and the MCS device is that extensional flow within the microfluidic analog can be assumed as planar (since $z \ll x, y$) whereas Taylor's experiments have to take into account three dimensional flow effects.

G.I. Taylor's four roll mill apparatus**Microfluidic MCS device equivalent****Legend**

Flow direction in MCS device inlets

Figure 2.2 G.I. Taylor's macro-scale four roll mill apparatus (in planar view) and the MCS device equivalent for producing stagnation flow in microfluidics. Rotation of the four roll mills (with a radius, r) at an equivalent angular velocity of ω , results in the surrounding fluid to flow at a velocity, v . Analogous to the four roll mill, the MCS device produces stagnation flow of a purely extensional nature when $Q=Q_1=Q_2=Q_3=Q_4$.

The planar extensional flow produced within the MCS device is characterized by a flow type parameter of $\xi = 1$. Substitution of $\xi = 1$ into equation [2.2] results in:

$$\Gamma = \begin{bmatrix} \dot{\epsilon} & 0 \\ 0 & -\dot{\epsilon} \end{bmatrix} \quad [2.4]$$

Substitution of equation [2.4] into [2.1] results in the planar extensional flow field:

$$\vec{v} = \begin{bmatrix} \dot{\epsilon} & 0 \\ 0 & -\dot{\epsilon} \end{bmatrix} \begin{pmatrix} x \\ y \end{pmatrix} \quad [2.5]$$

where x and y are rectangular co-ordinates defined by the co-ordinate system shown in Fig. 2.2.

The velocity field defined by equation [2.5] is subsequently substituted into the convection-diffusion equation (see Chapter 2.2.2.2) to obtain the mass transport parameters of the MCS device.

2.2.2 Equations that govern mass transport phenomena

2.2.2.1 Mass transport due to diffusion

The diffusion of particles in a solution was first defined by Einstein using the diffusion constant, D , such that (Einstein, 1905):

$$D = \frac{RT}{N} \cdot \left(\frac{1}{f}\right) = k_B T \left(\frac{1}{f}\right) \quad [2.6]$$

where R is the gas constant, T is the absolute temperature, N is Avogadro's number and k_B is the Boltzmann constant. f is the frictional coefficient experienced by a particle travelling through a viscous liquid, assuming a perfectly spherical particle.

According to Stoke's law (Stokes, 2009), the frictional coefficient is given by:

$$f = 6\pi\mu a \quad [2.7]$$

where μ is the fluid dynamic viscosity and a is the hydrodynamic radius of the particle.

Inserting [2.7] into [2.6] gives the Stokes-Einstein relation for the diffusion coefficient:

$$D = \frac{k_B T}{6\pi\mu R} \quad [2.8]$$

In dilute solutions, the diffusion coefficient defines the transport of a solute particle in a solvent and is the proportionality constant associated with the molar flux due to molecular diffusion and the gradient of the species concentration. Prior experiments for fluorescein and rhodamine 6G dyes in water have found the diffusion coefficient for the fluorescein and the rhodamine to be $5 \times 10^{-10} \text{ m}^2 \text{ s}^{-1}$ (Culbertson et al., 2002) and $4 \times 10^{-10} \text{ m}^2 \text{ s}^{-1}$ (Müller et al., 2008), respectively. These values of diffusion coefficient were used in the analytical and numerical calculations of concentration gradients formed within the MCS device (see Chapters 2.3, 2.4).

2.2.2.2 Mass transport due to the convection and diffusion

Within the MCS device, both convection and diffusion processes play a part in transporting solute concentration across the stagnation flow. The convection-diffusion equation can be derived from the conservation of chemical species equation (Deen, 1998):

$$\frac{\partial C_i}{\partial t} = -\vec{\nabla} \cdot \vec{N}_i + R_{vi} \quad [2.9]$$

where C_i is the molar concentration of chemical species i , N_i is the total flux and R_{vi} is net rate of formation of chemical species i during chemical reactions.

In the case of mass transport across the stagnation flow, no chemical reactions occur, therefore:

$$R_{vi} = 0 \quad [2.10]$$

The total flux due to convective and diffusive mass transport is:

$$\vec{N}_i = C_i \vec{v} + \vec{J}_i \quad [2.11]$$

Fick's law defines the concentration flux due to diffusion as:

$$J_i = -D_i \vec{\nabla} C_i \quad [2.12]$$

Submitting equations [2.10], [2.11] and [2.12] into [2.9] results in the convection-diffusion equation:

$$\frac{\partial C_i}{\partial t} = -\vec{\nabla} \cdot (C_i \vec{v} - D_i \vec{\nabla} C_i) = D_i \vec{\nabla}^2 C_i - \vec{v} \cdot \vec{\nabla} C_i \quad [2.13]$$

Inserting the velocity field (shown in equation [2.5]) into the convection-diffusion equation [2.13] solves for the concentration field within the MCS device. The following chapter (Chapter 2.3) discusses how the C-D equation in equation [2.13] can be simplified to solve for the mass transport of concentration species across the stagnation flow.

2.3 Analytical solution for mass transport across the stagnation flow

The mass transport of a single concentration species across the planar stagnation flow can be defined by the two dimensional form of the C-D equation shown in equation [2.14].

$$\frac{\partial C}{\partial t} = D \left(\frac{\partial^2 C}{\partial x^2} + \frac{\partial^2 C}{\partial y^2} \right) - \dot{\epsilon} \left(x \frac{\partial C}{\partial x} - y \frac{\partial C}{\partial y} \right) \quad [2.14]$$

where C is the concentration, D is the diffusion coefficient and $\dot{\epsilon}$ is the homogenous flow strain rate. x and y are the rectangular co-ordinates that are defined in Fig. 2.2.

Equivalent flow conditions in each of the inlets imply that near the stagnation point, the flow strain is homogenous such that $\dot{\epsilon} = \dot{\epsilon}_x = -\dot{\epsilon}_y$. The flow strain rate is defined as (Deen, 1998):

$$\dot{\epsilon} = \frac{\partial u}{\partial x} = -\frac{\partial v}{\partial y} \quad [2.15]$$

Near the stagnation point at the chamber centre, and based on the rectangular co-ordinate system defined, the value of this homogeneous strain rate was reduced to a single scalar function:

$$|\dot{\epsilon}| = \left| \frac{\Delta u}{\Delta x} \right| = \left| \frac{\Delta v}{\Delta y} \right| \quad [2.16]$$

By formulating equation [2.14], several key assumptions were made when considering mass transport across stagnation flow within the MCS device. Firstly, an assumption was made on fluid incompressibility. This was considered to be a valid assumption since fluid temperature and hence fluid density change was insignificant

during experiments, and experiment conditions would not produce foreseeable increases in fluid temperature. Secondly, the flow entering the chamber was considered to be fully developed; subsequent experiment results would prove this to be a valid assumption. Thirdly, mass diffusion effects throughout the depth of the device are sufficiently small such that a two-dimensional flow field may be considered. With the designed device geometry, the square stagnation flow chamber has length of $L=1\text{mm}$ and a device depth of $H=12\mu\text{m}$, such that the $L/H \gg 1$, thereby validating this approximation (Deen, 1998). Another assumption made was that the concentration gradient generated across the stagnation flow occurred near the stagnation point such that the extensional flow field adequately described the convective flux of the concentration species. Implicit in this assumption is that edge effects on the flow field, due to the chamber corners is negligible, and occurs sufficiently far away from the concentration gradient formed. This last assumption will later be validated by comparisons to the experimental and numerical data obtained for the MCS device (see Chapter 4).

In order to understand the physical mass transport phenomenon occurring across the stagnation flow, the C-D equation in equation [2.14] was non-dimensionalized by introducing the following parameters:

$$P\dot{\epsilon} = \frac{\dot{\epsilon}d^2}{D} \quad [2.17]$$

$$x_0 = \frac{d}{\sqrt{P\dot{\epsilon}}} \quad [2.18]$$

$$y_0 = \frac{d}{\sqrt{P\dot{\epsilon}}} \quad [2.19]$$

$$t_0 = \frac{d^2}{P\dot{\epsilon} \cdot D} \quad [2.20]$$

where d is the half the diagonal length of 1mm square chamber (*i.e.* $d = \frac{1}{2}\sqrt{2} = 0.707mm$), and $\dot{\epsilon}$ (s^{-1}) is the homogeneous flow strain rate.

The dimensionless length and time scale were defined as:

$$\tilde{x} = \frac{x}{x_0} = x \sqrt{\frac{\dot{\epsilon}}{D}} \quad [2.21]$$

$$\tilde{y} = \frac{y}{y_0} = y \sqrt{\frac{\dot{\epsilon}}{D}} \quad [2.22]$$

$$\tilde{t} = \frac{t}{t_0} = t\dot{\epsilon} \quad [2.23]$$

Inserting the dimensionless length scales (\tilde{x}, \tilde{y}) and time scale (\tilde{t}) into equation [2.14] results in the dimensionless C-D equation:

$$\frac{\partial C(\tilde{x}, \tilde{y}, \tilde{t})}{\partial \tilde{t}} = \frac{\partial^2 C(\tilde{x}, \tilde{y}, \tilde{t})}{\partial \tilde{x}^2} + \frac{\partial^2 C(\tilde{x}, \tilde{y}, \tilde{t})}{\partial \tilde{y}^2} - \tilde{x} \frac{\partial C(\tilde{x}, \tilde{y}, \tilde{t})}{\partial \tilde{x}} + \tilde{y} \frac{\partial C(\tilde{x}, \tilde{y}, \tilde{t})}{\partial \tilde{y}} \quad [2.24]$$

Although Equation [2.24] describes mass transport across the stagnation flow in its entirety, it is difficult to solve analytically since there are multiple variables ($u(\tilde{x}, \tilde{y}, \tilde{t}), v(\tilde{x}, \tilde{y}, \tilde{t}), C(\tilde{x}, \tilde{y}, \tilde{t})$) to solve for with limited initial and boundary conditions. In order to gain insight into the physical mass transport phenomenon occurring across the stagnation flow, the number of directions analyzed was reduced

by applying symmetrical boundary conditions for flow and concentration. Fig. 2.3 shows how the problem can be analyzed along one direction (*i.e.* y -direction) since symmetrical boundary conditions for concentration input imply that concentration variation along the x -direction is much smaller than that along the y -axis such that

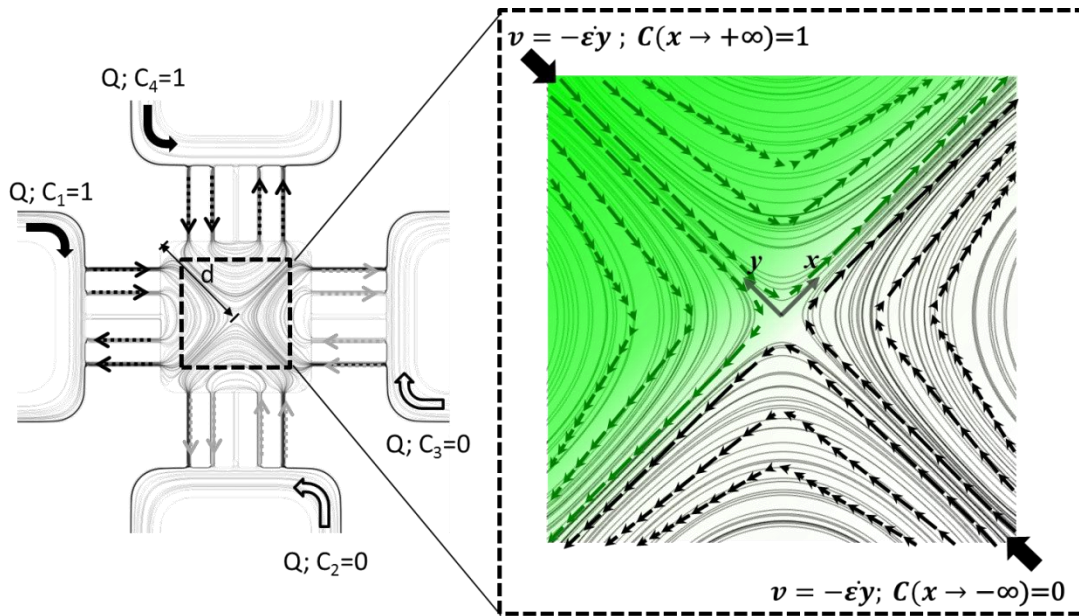
$$\frac{\partial C}{\partial x} \ll \frac{\partial C}{\partial y}.$$


Figure 2.3 Symmetrical boundary conditions that are applied to the modified cross-slot (MCS) device- shown with flow streamlines. The characteristic length for mass transport within the MCS device is defined as d , half the diagonal length of the 1mm square chamber.

Analyzing the problem along the y -axis results in the following C-D equation:

$$\frac{\partial C(\tilde{y}, \tilde{t})}{\partial \tilde{t}} = \frac{\partial^2 C(\tilde{y}, \tilde{t})}{\partial \tilde{y}^2} + \tilde{y} \frac{\partial C(\tilde{y}, \tilde{t})}{\partial \tilde{y}} \quad [2.25]$$

Based on the time and length scales defined, it can be seen that the concentration profile is a function of the Péclet number, *i.e.* $C(\tilde{y}, \tilde{t}) = f(Pé)$ and, neither dimensions y nor t appear in equation [2.25]. Equation [2.25] can be further simplified to the steady-state form in which the steady state concentration profile along the y axis is discoverable:

$$\frac{\partial^2 C(\tilde{y})}{\partial \tilde{y}^2} = -\tilde{y} \frac{\partial C(\tilde{y})}{\partial \tilde{y}} \quad [2.26]$$

Later experiments (discussed in Chapter 4) will show that increasing flow rates from $Q=100nl\ s^{-1}$ to $300nl\ s^{-1}$ could result in an increase in the measured flow strain, $\dot{\epsilon}$, from $O(10^{-1})$ to $O(10^1)$. Considering the smallest order of magnitude for $\dot{\epsilon} \sim O(10^{-1})$, the order of magnitude for the Péclet number was $\sim O(10^3)$, thus resulting in a characteristic time $\sim O(10^1)$. This means that within several of seconds, the concentration gradient within the MCS should stabilize, even at the lowest flow rate tested, validating the assumption of a pseudo steady-state problem.

Equation [2.26] can be integrated through a transfer variable $g(\tilde{y}) = \frac{\partial C(\tilde{y})}{\partial \tilde{y}}$. This transforms [2.26] into:

$$\frac{\partial g(\tilde{y})}{\partial \tilde{y}} = -\tilde{y} g(\tilde{y}) \quad [2.27a]$$

$$\frac{1}{g(\tilde{y})} \partial g(\tilde{y}) = -\tilde{y} \partial \tilde{y} \quad [2.27b]$$

Integrating [2.27b] on both sides results in:

$$\log g(\tilde{y}) = \frac{-\tilde{y}^2}{2} + B \quad [2.27c]$$

where B is the integration constant.

Taking the inverse logarithm for [2.27c] results in a solution for $g(\tilde{y})$:

$$g(\tilde{y}) = B \cdot \exp^{\frac{-\tilde{y}}{2}} \quad [2.27d]$$

Transferring $g(\tilde{y}) = \frac{\partial C(\tilde{y})}{\partial \tilde{y}}$ back into [2.27d] and integrating for $C(\tilde{y})$ results in:

$$C(\tilde{y}) = B \int \exp^{\frac{-\tilde{y}}{2}} d\tilde{y} \quad [2.27e]$$

The concentration profile can be determined by considering the following Dirichlet boundary conditions (also shown in Fig. 2.3):

$$C(y \rightarrow +\infty) \equiv C(\tilde{y} \rightarrow +\infty) = 1 \quad [2.28]$$

$$C(y \rightarrow -\infty) \equiv C(\tilde{y} \rightarrow -\infty) = 0 \quad [2.29]$$

Substituting the boundary conditions [2.28] and [2.29] into equation [2.27] allows for the determination of the integration constant, B :

$$C(\tilde{y}) = B \int_{-\infty}^{+\infty} \exp^{\frac{-\tilde{y}}{2}} d\tilde{y} = 1 - 0 \quad [2.30]$$

$$B = \frac{1}{\sqrt{2\pi}} \quad [2.31]$$

The concentration profile along the y -axis bounded by the range of $-\infty$ to y results in the following concentration profile:

$$C(\tilde{y}) = \frac{1}{2} \left[1 + \operatorname{erf} \left(\frac{\tilde{y}}{\sqrt{2}} \right) \right] \quad [2.32]$$

$$C(y) = \frac{1}{2} \left[1 + \operatorname{erf} \left(\sqrt{\frac{Pe}{2}} \cdot \frac{y}{d} \right) \right] \quad [2.33]$$

where erf is the error function and the dimensionless variable, $\tilde{y} = \sqrt{Pe} \cdot \frac{y}{d}$.

It should be mentioned that the scaling parameters selected to define this mass transport problem, were chosen after performing initial experiments on the MCS device. In this sense, the choice of the scaling parameters was based on trial and error substitution of several probable candidates for plausible characteristic length and time scales. Later experiments (discussed in Chapter 4) will prove the validity of the scaling technique with respect to the convective-diffusive processes occurring across the stagnation flow within the MCS device. The aforementioned analytical model, is however, only valid in one direction, under the application of symmetrical flow and concentration boundary conditions. In order to model the convection and diffusion process within the entire area of the stagnation flow chamber, numerical analysis was performed.

2.4 Numerical analysis of mass transport across stagnation flows

To gain insight into the velocity and concentration fields within the device, a numerical method was used to solve and couple equations for laminar flow and transport of dilute chemical species. The finite-element software, COMSOL MultiphysicsTM, was used to solve for the velocity field and concentration field within the device. The following governing equations for fluid flow were applied:

$$\vec{\nabla} \cdot \vec{v} = 0 \quad [2.34]$$

and

$$\rho \left(\frac{\partial \vec{v}}{\partial t} + \vec{v} \cdot \vec{\nabla} \vec{v} \right) = -\vec{\nabla} \mathcal{P} + \mu \nabla^2 \vec{v} \quad [2.35]$$

where \vec{v} is the velocity field and $\vec{\nabla} \mathcal{P} = \vec{\nabla} P - \rho \hat{g}$ is the dynamic pressure. μ is the dynamic viscosity of the fluid.

Once the velocity field was numerically calculated, the velocity field was coupled with the governing equation for the conservation of mass transport. Assuming that there was no adsorption of the solute species into the device walls, and no interaction between the solute species (Fluorescein-Na, Rhodamine 6G or *L*-Serine) and deionized water, the concentration field is governed by the following mass transport equation:

$$\frac{\partial C}{\partial t} = D \nabla^2 C - \vec{\nabla} \cdot (\vec{v} C) \quad [2.36]$$

where C is the molar concentration of the solute species, and D is the mass diffusion coefficient of the solute species.

2.4.1 Time scale analysis

Prior to performing the numerical simulations, time scale analysis was performed to determine if the velocity field and concentration field could be coupled and solved in a pseudo-steady state manner. The analysis was performed by considering the convective time scale (τ_c), the diffusive time scale (τ_d) and the viscous time scale (τ_v). It is known from flow analysis that stagnation flow occurs within the stagnation flow chamber and consequently, it can be deduced that the order of magnitude for time scales would range between that for a purely convective flux (τ_c) and that for a purely diffusive flux (τ_d). Calculating the order of magnitude

for each of the mass transport processes, using the characteristic length, d , results in the following time scales in terms of order of magnitude;

$$\tau_c = \frac{d}{U} \sim \frac{O(10^{-4})}{O(10^{-3})} = O(10^{-1}) \quad [2.37]$$

$$\tau_D = \frac{d^2}{D} \sim \frac{O(10^{-8})}{O(10^{-10})} = O(10^2) \quad [2.38]$$

$$\tau_v = \frac{d^2}{\vartheta} \sim \frac{O(10^{-8})}{O(10^{-6})} = O(10^{-2}) \quad [2.39]$$

where the characteristic length is taken as half the diagonal length of the square stagnation flow chamber (d) and has an order of magnitude of $O(10^{-4})$. U is the flow velocity and has the order of magnitude of $O(10^{-3})$. ϑ is the kinematic viscosity and has the order of magnitude of $O(10^{-6})$.

Based on the time scales shown in equations [2.37], [2.38] and [2.39], it is evident that $\frac{\tau_v}{\tau_c} \ll 1$ and $\frac{\tau_v}{\tau_D} \ll 1$, suggesting that the rate of momentum transfer is much faster than either convective and diffusive processes. In such a case the time to reach the steady-state velocity field would be much faster than that for the steady-state concentration field. Thus the velocity field was first solved in its steady-state form and was subsequently coupled to the time-dependent analysis of the concentration field. Furthermore, it was deduced that during experiments, concentration fields experimentally measured at durations greater than the diffusion time scale could be compared to the numerical data for the steady-state concentration field.

2.4.2 Mesh generation and domain setting

The mesh that was generated for flow field and concentration field simulations was three-dimensional. Fig. 2.4 shows the mesh generated in COMSOL MultiphysicsTM for the MCS device. A three-dimensional mesh geometry was chosen instead of a two-dimensional geometry as this accounted for depth effects during the calculation of shear stress within the stagnation flow chamber (see section 2.4.5 for shear stress calculations). Within this thesis, two variants of the MCS device geometry were designed (shown in Fig. 2.4 (a, b)). Fig. 2.4 (a) shows the basic design of the MCS device consisting of four flow inlets and four flow outlets. In Fig. 2.4(b), the MCS device geometry is slightly modified with the addition of two cell inlets and two outlets to allow the injection of the bacteria cell, *P. Aeruginosa* into the stagnation chamber (see Chapter 6 for more details). Two cell inlets and outlets were inserted such that the symmetry of the device was maintained, thus allowing stagnation flow to form within the square chamber. This device geometry had an extended stagnation flow chamber depth, which had to be simulated with a 3D mesh in order to account for flow velocity effects along the chamber depth.

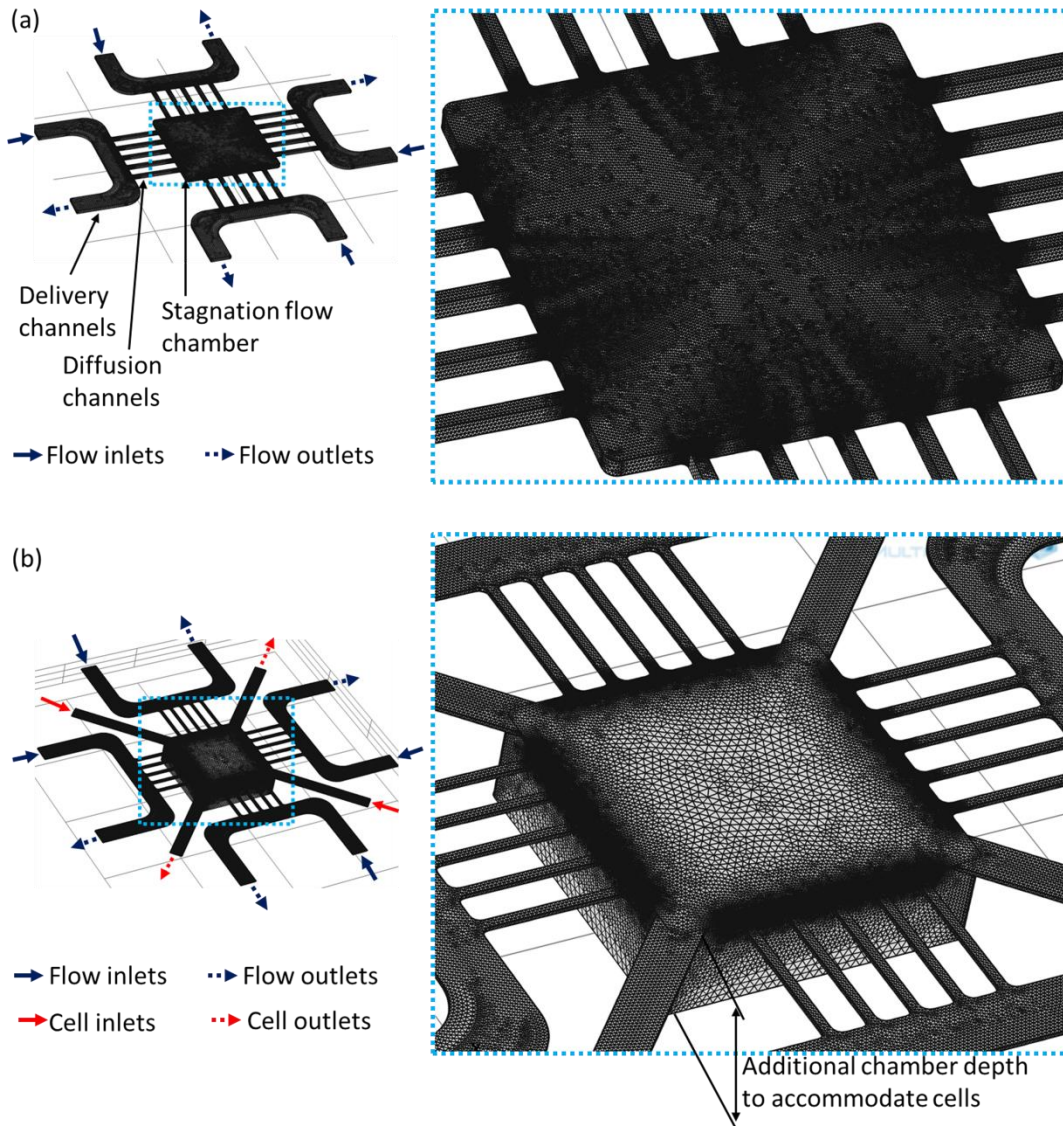


Figure 2.4 (a) 3D tetrahedral mesh for the MCS device which has a uniform depth of 12μm. (b) 3D tetrahedral mesh for the MCS device with cell chamber- Additional inlets for injecting cells are added to prevent cells from clotting the narrow diffusion channels. The cell chamber has a depth of 350μm while diffusion and delivery channels both have a depth of 12μm. (Right a,b) Zoomed-in mesh of the stagnation chamber for each device design.

For the basic MCS device (shown in Fig. 2.4(a)), the diffusion channels' width were varied at 20μm, 30μm and 50μm. The MCS device with the cell chamber

had diffusion channels' width of 30 μm . The mesh degree of freedom and total number of mesh elements for each device configuration are summarized in Table 2.1. The elements used to mesh the various device configurations consisted of tetrahedral, prism, triangular and quadrilateral elements. For each of the mesh geometries, a grid size independent test was conducted to ensure the accuracy of numerical results obtained. In order to reduce the total number of elements and prevent the simulation from encountering "out of memory" problems, only the MCS geometry that contained fluid flow was analyzed. The enclosing PDMS material or glass coverslip was not modelled as it was assumed that interaction effects due to the elasticity of the surrounding PDMS and any absorption of solute species into either the PDMS device or the coverslip were considered to be negligible.

Table 2.1 Meshing characteristics for simulating flow and concentration fields within the basic MCS device and the MCS device with cell chamber.

Device Type	Diffusion channel width (μm)	Mesh degree of freedom	Total number of elements
MCS	20	800,921	370,910
	30	934,366	429,850
	50	853,656	396,922
MCS with cell chamber	30	3,788,520	1,334,211

The entire MCS device domain was assigned as an incompressible fluid with the same viscosity and density as water (see Table 2.2). As the solutes (Fluorescein-Na, Rhodamine 6G or L-Serine) were diluted with water to less than 10% molarity, the bulk fluid properties were assumed to be those of water. (COMSOL, 2012) Table 2.2 lists the values that were assigned for the material properties used in the numerical simulations.

Table 2.2 Parameter values used to determine velocity and concentration fields.

Parameters	Values	Reference
Diffusion coefficient(D)	$5 \times 10^{-10} \text{ m}^2 \text{ s}^{-1}$ for Fluorecein-Na in deionized water	(Culbertson et al., 2002)
	$4 \times 10^{-10} \text{ m}^2 \text{ s}^{-1}$ for Rhodamine 6G in deionized water	(Gendron, Avaltroni, & Wilkinson, 2008)
	$8.8 \times 10^{-10} \text{ m}^2 \text{ s}^{-1}$ for L-Serine in M9 buffer	(Ma, Zhu, Ma, & Yu, 2005)
Dynamic viscosity (μ)	$1 \times 10^{-3} \text{ Pa} \cdot \text{s}$ for Fluorescein-Na, Rhodamine6G and L-serine solutions	(Kestin, Sokolov, & Wakeham, 1978)
Density (ρ)	$1000 \text{ kg} \cdot \text{m}^{-3}$ for Fluorescein-Na, Rhodamine 6G and L-serine solutions	(Archimedes, 2009)

2.4.3 Boundary conditions for steady state analysis

The velocity field within the MCS device was obtained by solving the N-S equations using the stationary solver with a relative residual of 1.0×10^{-6} . The boundary conditions used to stipulate flow at the device inlets, outlets and channel walls are summarized as follows:

Initial value (entire device): $\vec{u} = 0; P = 0$

Inlets: $\vec{u} = -\hat{n}U_0$

Channel walls other than inlets and outlets: $\vec{u} = 0$

Outlet: $P = 0$

where \vec{u} is the velocity field and $U_0 \text{ (m/s)}$ is the user specified velocity magnitude. U_0 is calculated from the flow rate, $Q \text{ (m}^3/\text{s)}$ and cross-section area of the delivery channels, $A \text{ (m}^2)$ such that $U_0 = \frac{Q}{A}$. \hat{n} is the unit vector that is normal to the surface where the boundary condition is applied. $P \text{ (Pa)}$ is the pressure.

At the initial time, there is no flow within the MCS device and the flow velocity is zero within the entire device domain. To simulate the steady-state velocity field, an inlet flow velocity, $\vec{u} = -\hat{n}U_0$, is assigned to the flow inlets and cell inlets (shown in Fig. 2.4). At the outlet, boundary conditions are set to zero gauge pressure such that $P=0$. No slip condition, $\vec{u} = 0$, is applied to all the channel walls unless over-rided by inflow or outflow boundary conditions.

The boundary conditions for the steady-state transport of concentration species are:

$$\text{Initial value (entire device): } \vec{u} = \vec{u}_{ss}; C = 0 \quad [2.40]$$

Concentration inflow:

$$C=0 \text{ (for deionized water injection)} \quad [2.41]$$

$$C=C_1 \text{ (for concentration species injection)} \quad [2.42]$$

$$\text{Concentration outflow: } \hat{n} \cdot (-D\nabla C) = 0 \quad [2.43]$$

Channel walls other than concentration inflow or outflow surfaces:

$$\hat{n} \cdot (C\vec{u} - D\nabla C) = N_0 \quad [2.44]$$

where \vec{u}_{ss} is the simulated steady-state velocity and C_l is the user specified molar concentration for the concentration species of interest. \hat{n} is the unit vector that is normal to the surface where the boundary condition is applied. D is the diffusion coefficient of the concentration species. N_0 specifies the jump in flux that is evaluated at the channel walls.

Based on time scale analysis, it was found that a steady-state velocity could be first solved and subsequently used as an initial condition for simulating the

concentration field. To simulate the concentration field, an inlet concentration flux, is assigned to the flow/ cell inlets (shown in Fig. 2.4). For flow inlets acting as concentration sources, a concentration inflow of $C=C_I$ is applied; C_I is the molar concentration of the concentration species studied. For flow inlets acting as concentration sinks, a concentration inflow of $C=0$ is applied. At the outlets, concentration outflow, $\hat{n} \cdot (-D\nabla C) = 0$ is applied to fulfil the conservation of concentration species. Zero flux permeability, $\hat{n} \cdot (C\vec{u} - D\nabla C) = 0$, is applied to all the channel walls unless over-riden by inflow or outflow boundary conditions. Table 2.3 summarizes the boundary conditions applied for solving the N-S and conservation of chemical species equations.

Table 2.3 Boundary conditions for simulating steady-state velocity and concentration fields.

	Inlet reservoir	Outlet reservoir	Wall
Flow field	Laminar velocity	Zero gauge pressure	No slip velocity
Solute concentration field	Molar concentration	Zero concentration flux	Impermeable

2.4.4 Boundary conditions for transient analysis

Based on the time scale analysis (section 2.4.1), the transient term is only considered in the mass transport equation. Thus the steady-state velocity is applied as an initial condition to solve the time-dependent concentration field. At the initial time, the steady-state velocity field is applied to the MCS device. In order to study the transient response of the concentration field in stagnation flow, a time dependent concentration inflow boundary condition was defined as:

$$C(t) = \begin{cases} 0, & 0 \leq t \leq 2 \\ C_1, & 2 < t < 30 \end{cases} \quad [2.45]$$

The concentration field of the solute species was then solved by applying the converged results for the stationary velocity field into a time-dependent solver with a time step of 0.1s. The total duration that was calculated in the time-dependent solver was set at 30s. The total process duration was initially guessed by analyzing the order of magnitude of time taken for a purely diffusive flux, *i.e.* $O(10^2) \sim 100s$ (see equation [2.38]); this was considered to be the longest time scale for the concentration field to stabilize without any contributions from the convective flux. After analyzing initial results obtained from the time-dependent simulations, the time for transient analysis was reduced to 30s. Later experiment results also found that the time scale for time-dependent numerical simulations could be adequately approximated using the analytical characteristic time for mass transport within the MCS device (see equation [2.20]).

2.4.5 Wall shear stress calculations from velocity fields

The COMSOL Multiphysics GUI does not automatically generate an expression for the wall shear stresses since wall shear stress varies along the 3D mesh geometry (COMSOL, 2012). For the basic MCS device (shown in Fig. 2.4(a)), the maximum wall shear stress within the stagnation chamber was derived by defining a wall shear stress expression during results post-processing. The maximum wall shear stress was calculated from the velocity field at the mid-plane of the chamber depth (see Fig. 2.5). The mid-plane of the device chamber was chosen as it

is the location where the velocity magnitude, and hence wall shear stress is maximum (Bacabac et al., 2005). For instance, in the MCS device with a stagnation chamber of depth, $H=12\mu\text{m}$, the simulated velocity field at the mid- plane, $H_{0.5}=6\mu\text{m}$, was extracted to calculate the maximum wall shear stress. Assuming fully developed Poiseuille flow, the maximum shear stress, τ_{wss} , evaluated at the wall is :

$$\tau_{wss}|_{Z=0} = 6\bar{U} \cdot \frac{\mu}{H} \quad [2.46]$$

where \bar{U} is the mean velocity, μ is the fluid dynamic viscosity and H is the depth of the stagnation flow chamber. Assuming fully developed Poiseuille pressure-driven flow, \bar{U} is derived from the velocity magnitude, U such that $\bar{U} = \frac{2}{3}U$. Z is the global co-ordinate of the mesh geometry shown in Fig. 2.5.

The wall shear stress for the MCS with cell chamber device was also obtained in a similar manner. The simulated velocity field was obtained at the mid-plane ($H_{midplane}=150\mu\text{m}$) of the cell chamber with a depth of $300\mu\text{m}$. The velocity field was subsequently used to calculate the maximum shear stress within the cell chamber, using equation [2.46].

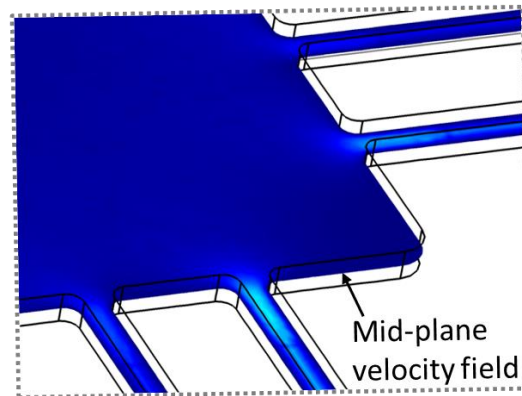
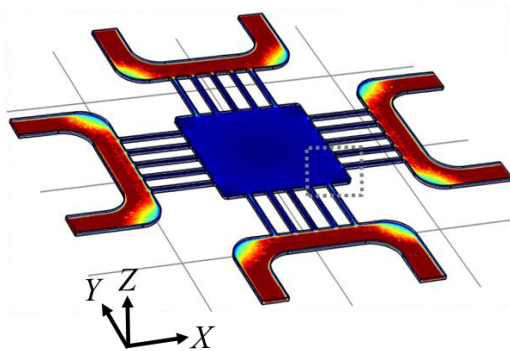


Figure 2.5 Mid-plane slice of the velocity field within the MCS device. The velocity magnitude is subsequently used to map the maximum wall shear stress occurring chamber at the base. X , Y and Z are the global co-ordinates of the mesh geometry.

2.4.6 Summary

In this chapter, a theoretical framework was developed for describing the mass transport of concentration species within the MCS device. An analytical model was developed to gain insights on the reference time and length scale of the MCS device. Both time and length scales were found to be intrinsically linked to the Pé number. Later experiment results (Chapter Four) will show the relevance of the analytical model to characterizing mass transport within the MCS device. In order to evaluate and couple the 3D incompressible Navier–Stokes equations for flow velocity to the mass conservation equations for concentration species, a numerical model was also developed using COMSOL MultiphysicsTM. Time scale analysis was implemented to simplify the numerical model and reduce computation loading. The numerical model was used to predict the velocity and concentration fields for various solutes that were experimentally tested. The model was also used to evaluate the maximum wall shear stress within the stagnation flow chamber of the MCS device. The analytical and numerical velocity, concentration and wall shear stress field will be validated by comparisons to the experimental results shown in the following Chapters four, five and six.

3 Modified Cross-Slot (MCS) Device Design, Fabrication and Experimental Setup

This section summarizes the design and fabrication processes of the MCS device, the experimental setup and the protocols used to test for the steady-state and transient responses of the concentration and velocity fields within the device. Image processing and particle image velocimetry techniques used to characterize the fields are defined. This section also includes the protocols used for adaptation studies of *P. Aeruginosa* cells that were performed using the MCS device.

3.1 MCS device design

In this thesis, as previously mentioned in Chapter 2, two variants of the MCS device were studied- the MCS device with homogeneous device depth and the MCS device with a step-down cell chamber (see Section 2.4). The MCS device with homogeneous device depth was used for microfluidic experiments that characterized velocity and concentration fields within the stagnation flow. The MCS device with a step-down cell chamber was used to accommodate the introduction and attachment of *P. Aeruginosa* cells to the centre stagnation chamber.

Prior to fabricating the devices through soft lithography techniques (Xia & Whitesides, 1998), a mask design with the MCS design and geometrical dimensions was made. The geometrical dimensions of the device designs are shown in Fig. 3.1. The mask designs for the MCS devices were designed using the Solidworks

software. All the device variants consisted of four delivery channels, five diffusion channels and a centre stagnation flow chamber. The delivery channels had a width of $200\mu\text{m}$ and the centre stagnation chamber was a square of $1000\mu\text{m}$. Using the basic MCS device (Fig. 3.1 (a)), the effect of diffusion channel width (w) was studied and varied at $20\mu\text{m}$, $30\mu\text{m}$ and $50\mu\text{m}$. For the MCS device with a uniform depth of $12\mu\text{m}$, a sub-variant consisting of an additional layer of microvalves was introduced (Fig. 3.1(b)). The MCS device with valves was introduced to enable fast hydrodynamic positioning of the stagnation flow (discussed in Section 5). Fig. 3.1(b) shows the MCS device that was modified with an additional layer of Quake valves (Unger, Chou, Thorsen, Scherer, & Quake, 2000). Due to the extremely low dead volume of the Quake valves (Unger et al., 2000), this variant of the MCS device allowed the study of fast hydrodynamic positioning of stagnation flows and confined concentration gradients. The MCS fluidic channels with Quake valves had the same dimensions as the basic MCS device but were bonded to a PDMS membrane and control channel layer (shown in Fig. 3.1(b)). During valve actuation, pneumatic pressure was pumped into the control channels, and the flexible PDMS membrane ($15\mu\text{m}$ in thickness) deflected to constrict the flow rate in the overlying fluidic channels. The amount of pressure required for the valves to constrict flow in the overlying channels was calibrated prior to performing microfluidic experiments (later discussed in Section 3.3.1.1.2).

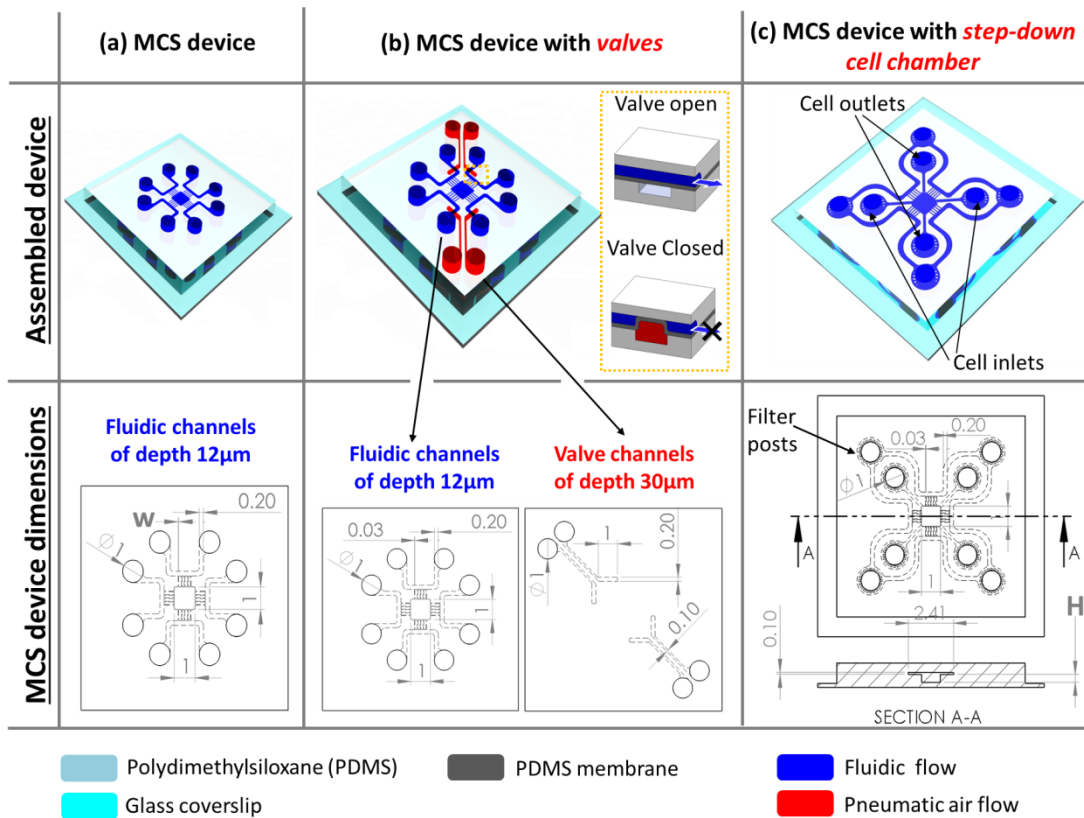


Figure 3.1 Device assembly and dimensions of (a) the MCS device, (b) the MCS device with valves and (c) the MCS device with a step-down cell chamber. All device dimensions shown are in *mm*.

In order to study *P. Aeruginosa* cells in stagnation flow, minor modifications were made to the basic MCS device design. The modifications included two additional cell inlets and outlets, filter posts at each cell inlet/ outlet to prevent cell clumps from clogging the diffusion channels, and a step-down cell chamber (shown in Fig. 3.1 (c)). The step-down chamber had a depth of $H=350\mu\text{m}$ while delivery and diffusion channels both had a depth of $12\mu\text{m}$. All the device variants had the features of the basic MCS device (shown in Fig. 3.1 (a)) as the basic device structure was derived based on results obtained from iterative cycles of numerical modeling. Once

numerical results confirmed that a purely extensional stagnation flow pattern could be achieved by the device, the device fabrication process was started.

3.2 MCS Device Fabrication and Materials

In this thesis, all the variants of the modified cross-slot (MCS) device were fabricated using the soft lithography process (Xia & Whitesides, 1998). In general, the soft lithography process includes firstly fabricating a Silicon (Si) mold consisting of lithographically developed photoresist patterns and subsequently molding the polydimethylsiloxane (PDMS) devices from these Si molds. For the photolithography fabrication of the MCS device mold (Fig. 3.2(a), step (i, ii)), negative-tone KMPR 1010 photoresist was spin coated onto a dehydrated Si wafer at a speed of 1200rpm, resulting in a photoresist layer that was 12 μ m thick. The photoresist was then soft-baked at a temperature of 95 °C for 15mins. Following which, the wafer was exposed to I-line (365 nm) light through a negative-tone mask containing the MCS device pattern (Fig. 3.2(a), step (ii)). The exposed wafer was then soft-baked at 95°C for 9 mins to promote photoresist crosslinking. The crosslinked (light exposed) photoresist areas experienced a solubility difference with the uncrosslinked (light blocked) areas, when submerged in the SU-8 developer. After submersion development for 1 min, the crosslinked areas were removed in the developer and revealed raised photoresist features of the MCS device design. The developed Si mold was then hardbaked at 95°C in a fluoro-octyl-trichloro-silane (FOTS) vapour oven. FOTS coating was performed by aliquoting 60 μ l of FOTS solution into a petri dish and vapourizing the solution within a vacuum oven that contained the Si wafer molds. (see Appendix A for more details). The hardbaking

with FOTS anti-stiction coating ensured the longevity of the mold and complete demolded of the PDMS devices.

All MCS devices were made from polydimethylsiloxane (PDMS) and molded from Si molds. PDMS is a liquid silicone rubber that is formed from a mixture of 10:1 weight ratio of elastomer and curing agent. In its liquid state, the PDMS was poured over the Si mold to a liquid height of $\sim 3\text{mm}$. The Si mold together with PDMS was cured in an oven at 80°C for one hour and the molded PDMS devices ($\sim 3\text{mm}$ thickness) were peeled off from the mold. Inlet and outlet holes of 1mm diameter were punched through the thickness of the device using a micropuncher (Harris). After this, the PDMS (molded channels side) and a glass coverslip was plasma treated using an atmospheric air plasma (Inspiraz). The plasma treatment was activated at an RF voltage of 100W and for a duration of 15s. In the final step the plasma activated PDMS channels were sealed with the coverslip and the device bonding step was concluded with oven baking of 110°C for 1 hour. The fabrication process flow for the PDMS molding and device bonding of all the MCS device designs is similar and schematically shown in Fig. 3.2 (a: steps(iii- vii), (b: steps(iii-x)), (c: steps(iv-viii)).

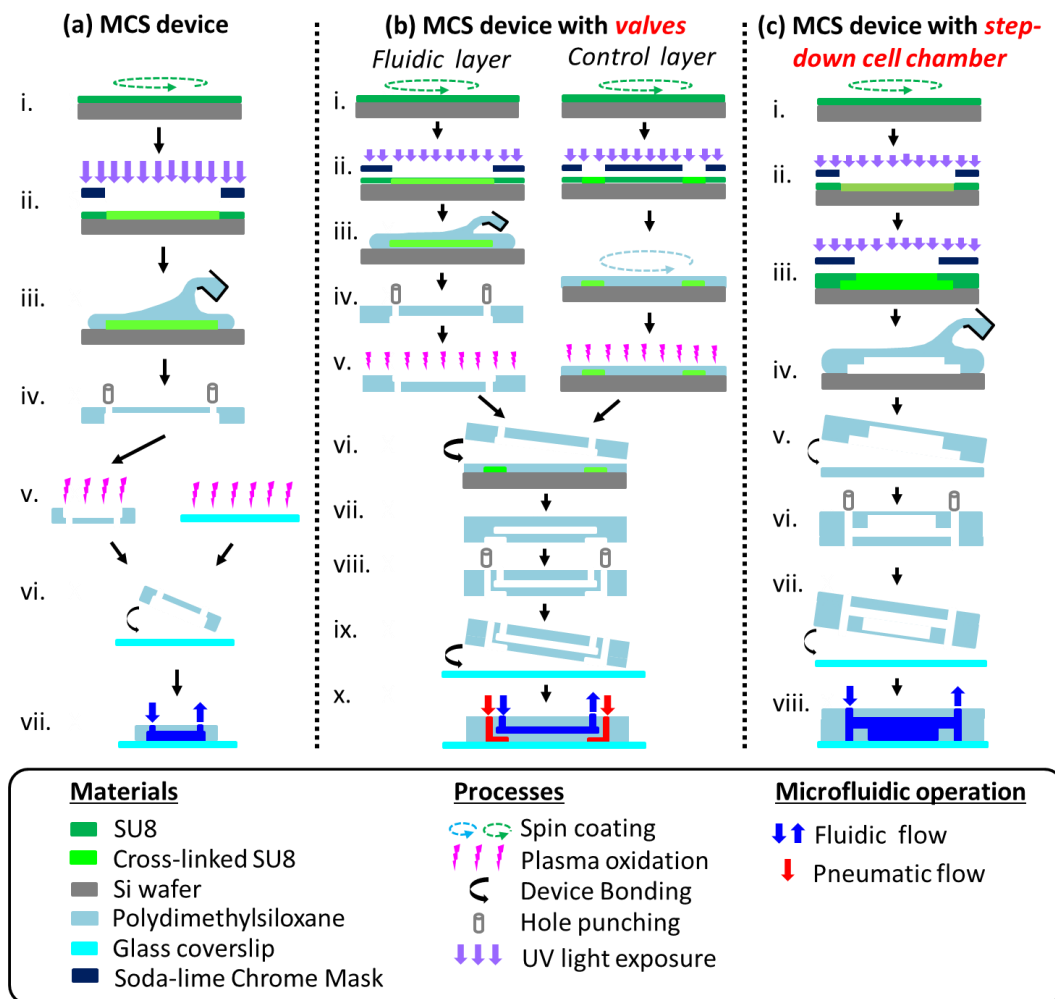


Figure 3.2 Schematic illustration of the soft lithography process that was used to fabricate (a) the MCS device, (b) the MCS device with valves and (c) the MCS device with step-down cell chamber.

For the MCS device with valves, an additional Si mold was fabricated to define the control valve layer. As shown in Fig. 3.2 (b: steps(i-ii)), an additional mold with control channel features of $30\mu\text{m}$ in height was fabricated to mold the control layer. In order to create an embedded membrane within the assembled device (see Fig. 3.2(b)), a thin layer of PDMS ($\sim 45\mu\text{m}$ thick) was spin coated onto the control layer Si mold to form a $15\mu\text{m}$ thick membrane over the control channel features. Once the PDMS was cured for both the fluid and control layer, they were

plasma treated and bonded together (Fig. 3.2 (b: steps(iv-vi))). For the MCS device with the extended cell chamber, a dual step lithography process was required to fabricate the additional chamber feature height. The MCS device design shown in Fig. 3.2(c) was first lithographical formed to a feature height of 12 μ m. After this first layer of lithography was completed (Fig. 3.2(c: steps(i,ii))), a second layer of photoresist was spin coated onto the developed features. This second layer was developed to form an extended chamber depth (Fig. 3.2(c: steps(iii,iv))). The Si mold with dual feature heights was then used to mold the PDMS device. In order to obtain a flat viewing plane at the base of the step-down cell chamber, the molded PDMS device was first bonded to a featureless PDMS layer that was ~2mm thick (Fig. 3.2(c: steps(v))). After this bonding step, the inlet and outlet holes were punched through the PDMS ensemble and subsequently bonded to a glass coverslip (Fig. 3.2(c: steps(vi-viii))).

Prior to performing the microfluidic experiments, the devices were pre-filled with food dye to ensure that they were leak-proof and did not have any unbonded surfaces. Fig. 3.3 shows a photograph of each of the MCS device variants- each MCS device was bonded to a glass coverslip that was 25mm by 75mm, with a thickness of 1mm. The experiment results and analysis for the MCS device, the MCS device with valves and the MCS device with cell chamber will be discussed in detail in Chapters 4, 5 and 6, respectively.

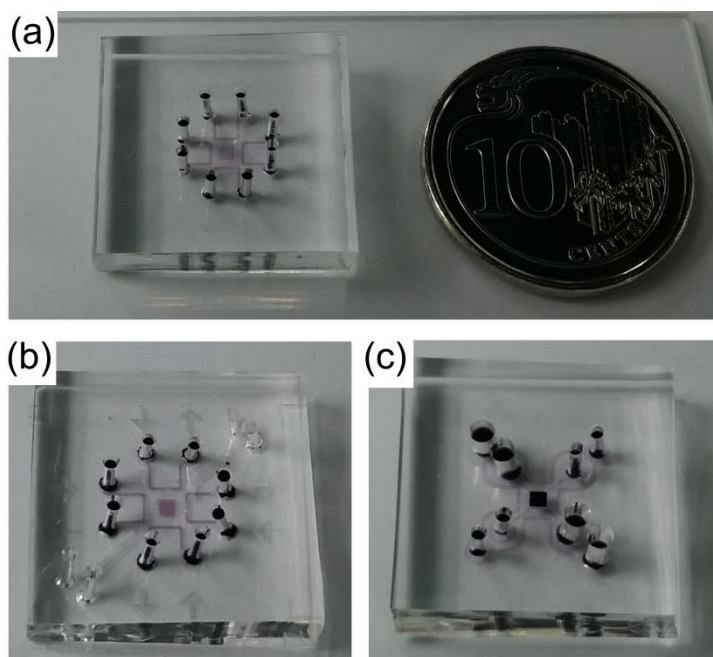


Figure 3.3 Photograph of pre-filled PDMS devices consisting of (a) the Modified Cross-slot (MCS) design, (b) the MCS with valve design and (c) the MCS with step-down cell chamber.

3.3 Experimental Setup

This section is split into two major sections; the first section discusses the setup, calibration and testing protocols used in microfluidic experiments while the second section discusses the experimental protocols used in the biological experiments involving the study of *P. Aeruginosa* cells.

3.3.1 Microfluidic experiment setup

The microfluidic experiment setup consisted of a customized pressure pump that was digitally controlled to pump fluid or air (in the case of valve actuation) into the MCS device. The experimental setup is shown in Fig. 3.4. A fluorescence microscope (Olympus) that was illuminated with a mercury lamp was used to view

fluid flow within the device. In order to view the fluorescein and Rhodamine 6G solutes during concentration gradient experiments, the microscope was fitted with filter cube to emit different excitation light wavelengths. An excitation wavelength of 385nm and 580nm was used to excite Fluorescein and Rhodamine 6G dyes respectively. Fluorescein beads used in particle velocimetry (PIV) studies were also illuminated with 385nm light. The microscope was fitted with a CCD camera (Lumera, Germany) that could acquire images at a maximum frame speed of 40fps. The CCD camera was linked to a computer via an image processing software (Streampix) that processed and stored the images. In order to perform transient flow analysis, each captured image was time-stamped with the time of capture. All images were captured using an objective lens of 10x.

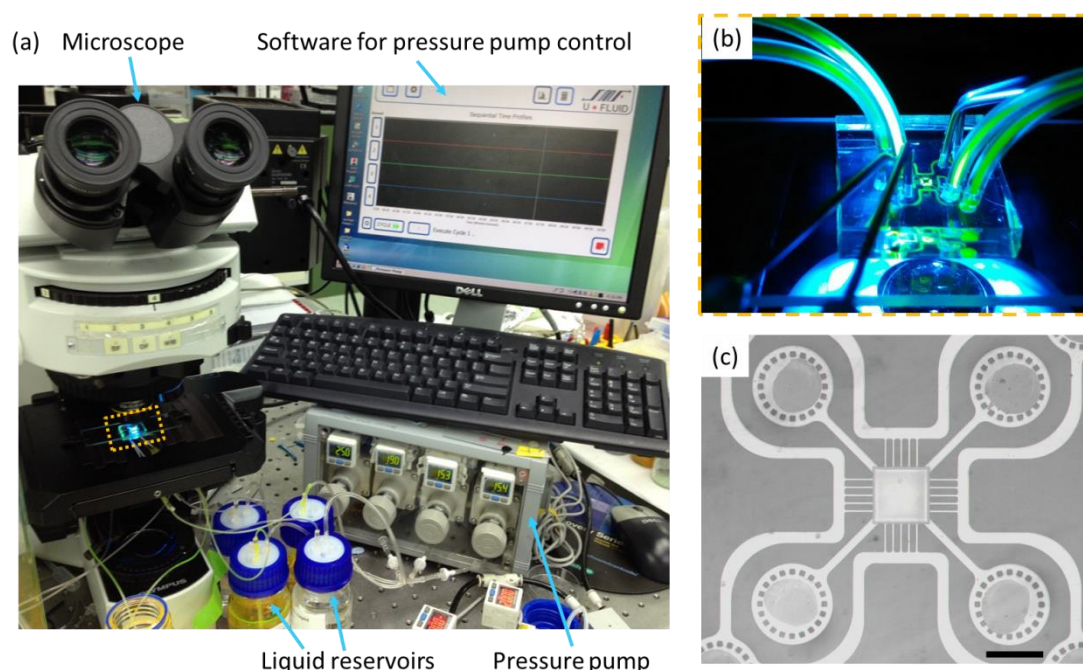


Figure 3.4 (a) Equipment and experimental setup. (b) Zoomed-in view of the MCS device that is encircled in the orange box in (a). The fluorescein dye injected into the MCS device is illuminated with the excitation wavelength of 480nm and emits a

yellow/ green fluorescent wavelength (~520nm). (c) Microscopy image of the MCS device. Scale bar shown in (c) is 1000 μ m.

In order to temporally control stable fluid injection into the MCS device, a customized pressure pump was designed and fabricated. Prior to developing the pressure pump, syringe pumps were initially tested and found to produce unstable stagnation flow. For stable stagnation flow to occur, each of the four inlets in the MCS device had to be injected with temporally stable and equivalent flow rates. This was difficult to achieve with syringe pumps due to the non-tandem flow fluctuations that resulted from non-synchronized motor stepping of the syringe pumps. An earlier report has also observed these flow irregularities in syringe pumps (Z. Li, Mak, Sauret, & Shum, 2014). Conversely, the pressure pump configuration (shown in Fig. 3.4 (a)) provided precise and pulse-less control for inlet flow injections ranging from 30 $nl\ s^{-1}$ to 1000 $nl\ s^{-1}$. The pressure pump injected air pressure into the liquid reservoirs (see Fig. 3.4(a)) and volume displacement resulted in liquid injection into the MCS device. The pressure pump could be manual controlled through external pressure regulators or programmed through the digital user interface. The user interface was created using LabVIEW and controlled the electronic components within the pump. The pump consisted of electronic solenoid valves, pressure actuators and regulators that were linked to a NI DAQ module, which in turn communicated with the LabVIEW software. The components and technical designs for the customized pressure pump is included in Appendix B. The pressure pump was also used to control valve actuation within the MCS device with valves. As the

pressure pump could only control injection pressure, a calibration step was required to convert the injection pressure to injection flow rate.

3.3.1.1 Pressure versus flow rate calibration of the MCS devices

3.3.1.1.1 Fluidic pressure calibration

For each of the MCS device designs, a calibration of pump pressure to inlet flow rate was performed using a flow rate sensor. The flow rate sensor was selected to measure a flow range of 1- 50 μ l min⁻¹ and had a flow rate accuracy of 5% full scale flow rate (Mitos flow sensor, Dolomite). The flow rate sensor was factory calibrated to detect flow with the viscosity of water, and at a room temperature of 27°C. In experiments that were performed on the basic MCS device, flow rates were calibrated for each of the designs where the diffusion channel width was adjusted at 20 μ m, 30 μ m and 50 μ m. The pressure versus flow rate calibration for each diffusion channel width is plotted in Fig. 3.5. The inset in Fig. 3.5 shows the microscope images of diffusion channels having channel widths of 20 μ m, 30 μ m and 50 μ m. The pressure versus flow rate calibration curves for the MCS devices followed an allometric fit as shown in the data legend within Fig. 3.5.

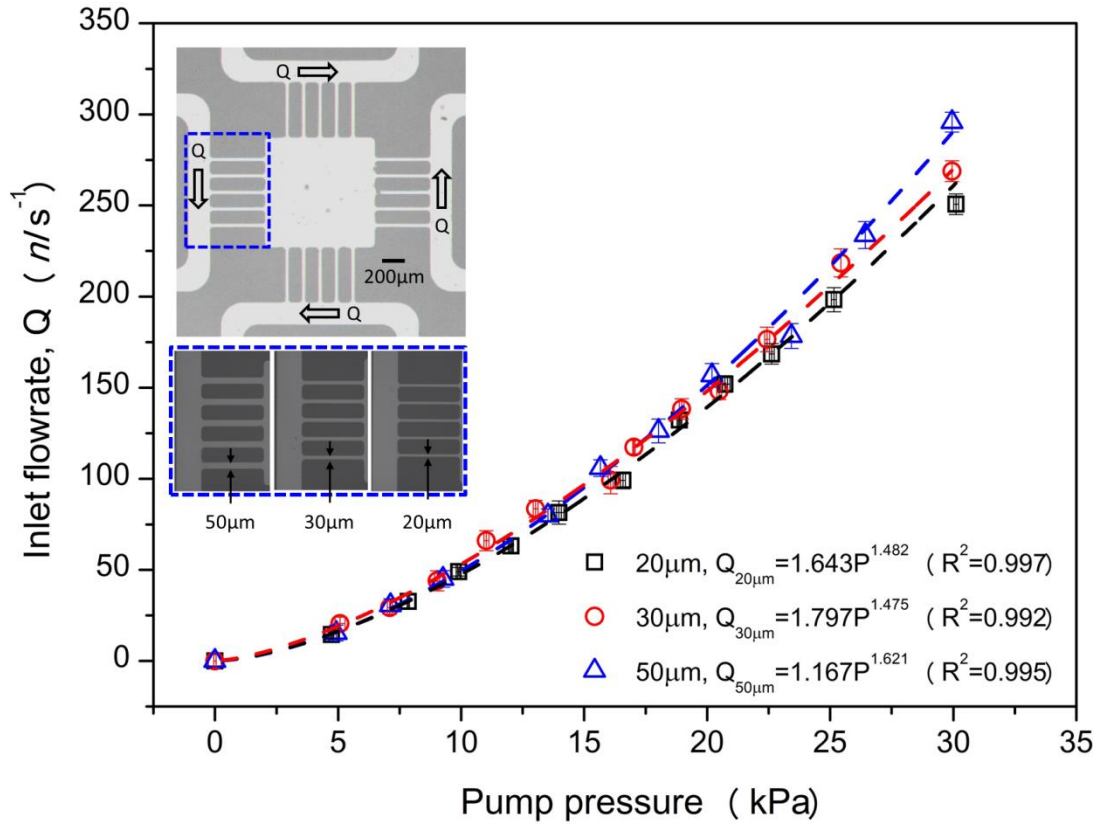


Figure 3.5 Inlet flow rate versus pump pressure calibration curve for MCS devices having diffusion channels widths of $20\mu\text{m}$, $30\mu\text{m}$ and $50\mu\text{m}$. (Inset) Microscope images the MCS device with zoomed-in view (blue dotted box) of the different channel widths tested.

The flow rate within the MCS device with valves were also calibrated with respect to the pump pressure. The calibration curve for the MCS device with valves is plotted in Fig. 3.6 and was also found to follow an allometric fit. The calibration curve for the MCS devices with step-down cell chamber is plotted in Fig. 3.7. These calibrated flow rates for all the MCS devices will be used in later Chapters to describe the concentration gradient formation in stagnation flows, under various flow rate conditions.

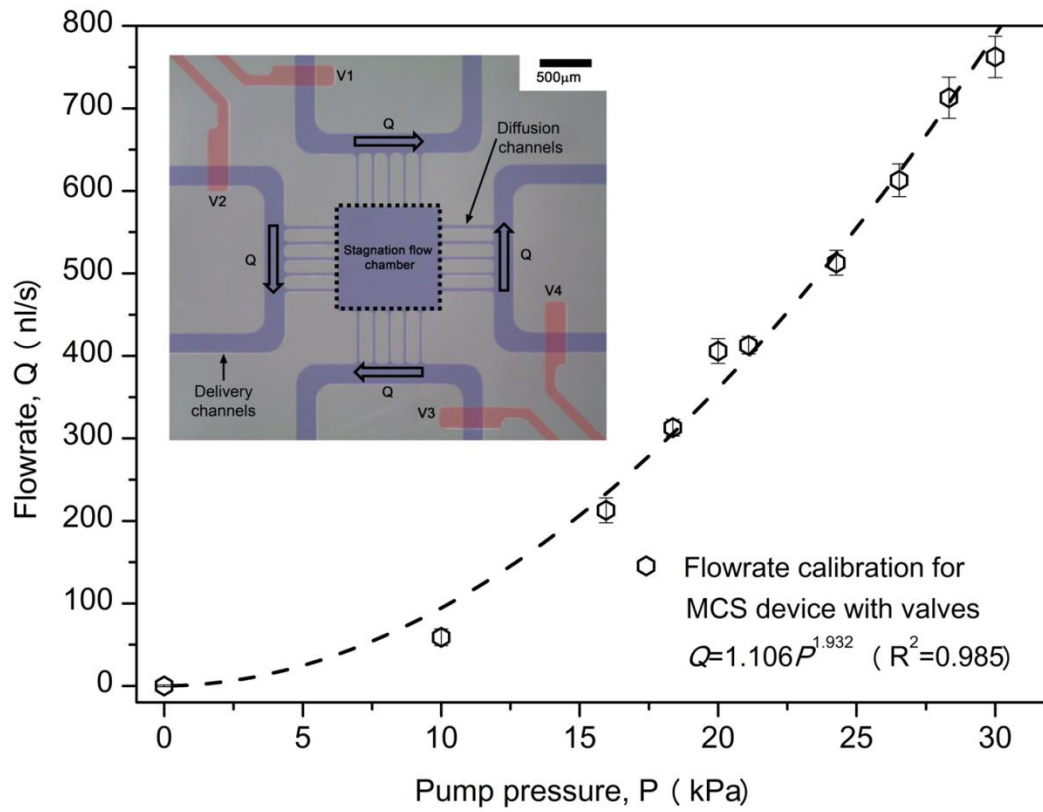


Figure 3.6 Inlet flow rate versus pump pressure calibration curve for MCS devices with valves. (*Inset*) Microscope image of the MCS device with fluidic channels (filled with blue dye) and underlying valve control channels, V_1 - V_4 (filled with red dye).

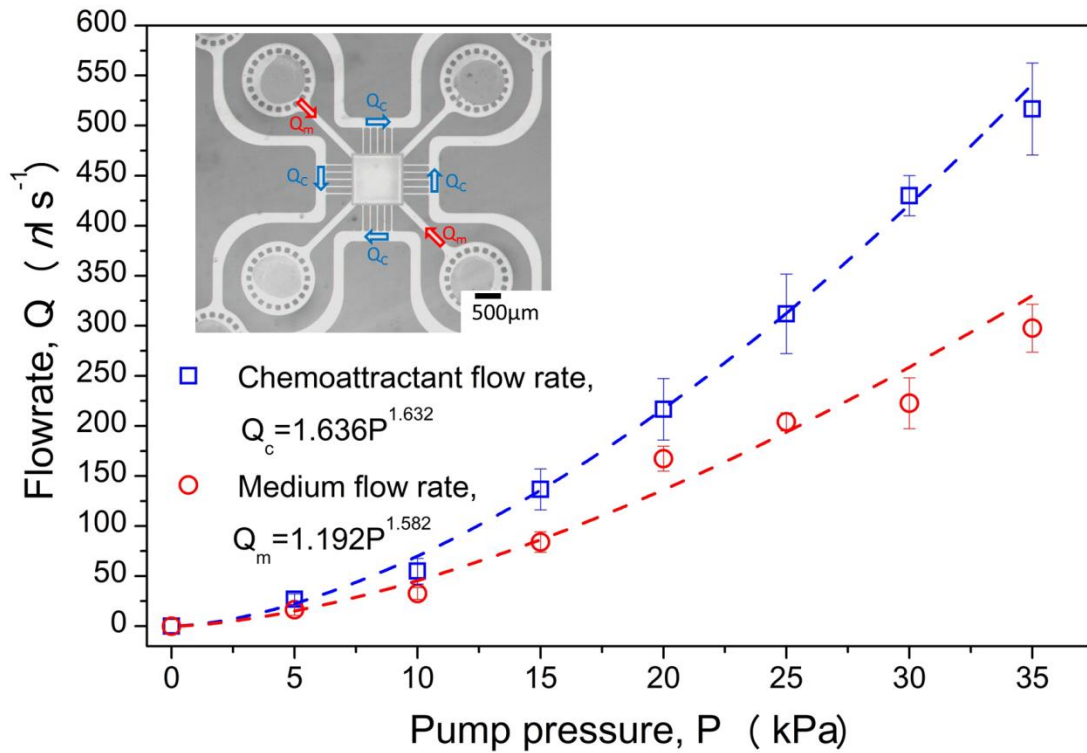


Figure 3.7 Inlet flow rate versus pump pressure calibration curve for MCS devices with extended cell chamber. (*Inset*) Microscope image of MCS device with flow inlets for the cell medium, Q_m and chemoattractant, Q_c .

Contrary to the linear Hagen-Poiseuille equation of correlating pressure to flow rate (Sutera & Skalak, 1993), a linear calibration curve did not fit the experimental data points well. This non-linearity has previously been attributed to the bulging of PDMS microchannels during pressure-driven flow (Holden et al., 2003; Gervais et al., 2006; Inglis, 2010). During calibration experiments, pressure-driven flow resulted in the expansion of microchannels and membrane valve chambers, allowing more flow to enter the device as flow pressure increased. Additionally, the use of elastic (deformable) tubings to connect the pump to the device may also contribute to the non-linearity of the Hagen-Poiseuille equation.

3.3.1.1.2 Valve pressure calibration

In experiments performed on the MCS device with valves, the pump pressure was used to deflect the PDMS membrane valves unto the overlying fluidic channel. The cross-section of each of the four membrane valves within the MCS device is schematically shown in Fig. 3.8(a). When the valves are not pressurized, the overlying fluidic channels are not constricted and fluid flows freely into the stagnation chamber. When valve control channels are pressurized, the overlying fluidic channel is constricted and fluid flow into the stagnation chamber is reduced. For example, when the inlet flow rate, Q was set at 100nl s^{-1} , valves pressurized at 16kPa resulted in a chamber flow rate of 50nls^{-1} (50% valve closure). In order to calibrate valve closure with respect to overlying fluid channel flow rate, the valving closure was measured at different inlet flow rates (see Fig. 3.8(b)). The valving closure (η) of the membrane valves were defined as:

$$\eta = \frac{Q_{P_v=0} - Q_{P_v}}{Q_{P_v=0}} \times 100\% \quad [3.1]$$

where $Q_{P_v=0}$ is the flow rate entering the device before the valve is actuated and Q_{P_v} is the flow rate entering the device after the valve is actuated at a valve actuation pressure (P_v).

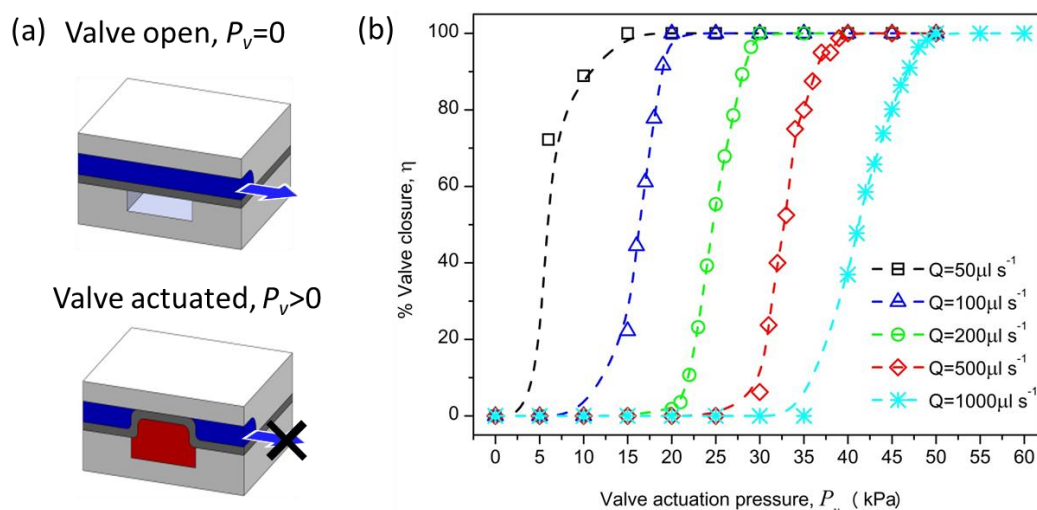


Figure 3.8 (a) Principle of membrane valve actuation within the MCS devices with valves- blue channel is filled with fluid and red channel is pressurized with air. (b) Valve closure (η) calibration plot with respect to inlet flow rate (Q) and valve actuation pressure (P_v).

3.3.1.2 Sample preparation and fluorescence calibration

Fluorescein-Na (Sigma-Aldrich) and Rhodamine 6G (Sigma-Aldrich) were used as sample solutes in concentration gradient generation experiments. Fluorescein-Na is a water-soluble fluorescent dye, which has an excitation wavelength of 485 nm and an emission wavelength of 521 nm. 1mM Fluorescein solution and 0.1mM of Rhodamine 6G solution were used to test the concentration gradients across the stagnation flow. The Fluorescein solution was made by dissolving 0.376g of Fluorescein-Na dye into 1L of deionized water. The Rhodamine 6G solution was made by dissolving 0.048g of Rhodamine 6G dye into 1L of deionized water. The dye solutions were stored at 4°C prior to use in experiments. During concentration gradient generation experiments, it was imperative to

determine if the intensity fluorescence emitted from the dye varied linearly with changes in dye concentration. If a linear relationship exists, the normalized intensity of the dye fluorescence could be directly used to derive the actual concentration of dye present. Using a spectrophotometer (Nanodrop 3300, Thermo Fisher Scientific), the fluorescence emission of each dye was calibrated. Fig. 3.9 shows the fluorescence emission plot for Fluorescein and Rhodamine 6G solutions. For the concentration limit of 1mM of fluorescein solution, the fluorescence emission had a linear relationship to dye concentration, with a R^2 fit of 0.995 (see Fig. 3.9(a)). For Rhodamine 6G solutions, it was found that dye concentrations greater than 0.12mM resulted in a saturated fluorescence response. However, using a Rhodamine 6G solution with a concentration limit of 0.1mM resulted in a linear relationship (with an R^2 fit of 0.999) between the dye concentration and fluorescence emission. It was found that at the concentration used for Fluorescein and Rhodamine 6G solutions, the actual dye concentrations could be directly derived from the normalized intensity measurements of concentration gradients.

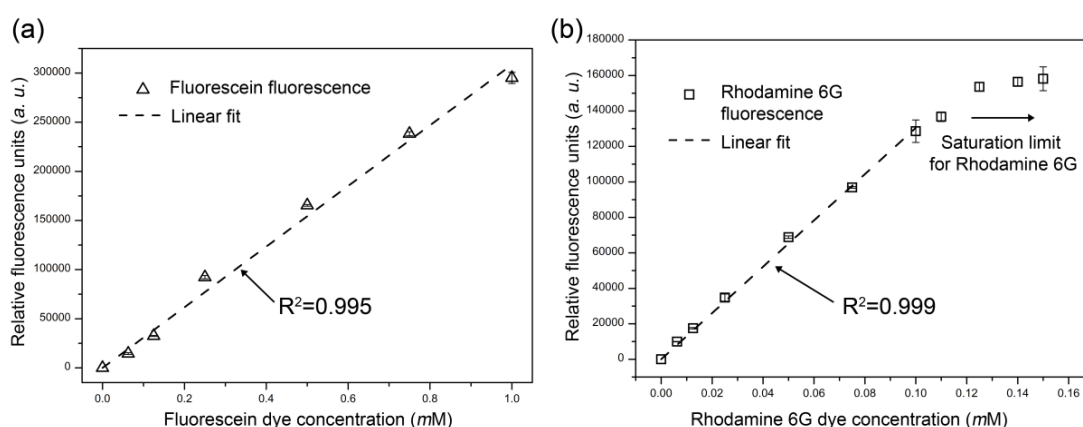


Figure 3.9 Fluorescence emission calibration curve for (a) Fluorescein and (b) Rhodamine 6G solutions.

In order to quantify the flow velocity and flow strain rate within the MCS devices, Fluorescein labeled carboxylate beads (2 μm diameter, Polybead, Polysciences, Inc.) were used to trace the flowpaths. Carboxylate coated beads were used to prevent beads from sticking to the surface of the MCS device channels and subsequently clogging the channels. The tracer beads were mixed with deionized water to a concentration of 1×10^4 beads ml^{-1} . In order to prevent bead aggregates from entering the device and clogging the channels, a $10\mu\text{m}$ track etched in-line filter was used to filter the solution.

3.3.1.3 Experimental procedure and image processing

Prior to concentration gradient experiments, the MCS devices were primed with deionized water to ensure that no bubbles were trapped within the device and in-line tubings. This process ensured that bubbles did not form within the device and prevented pressure instability attributed by the presence of bubbles. Pressure instability affects the formation of stable stagnation flows and concentration gradients. Once the device was primed, user-specified pressure settings were programmed into the pressure pump software and flow within the device was imaged.

The concentration gradients formed were measured from CCD images captured during experiments. The images captured were 8 bit grayscale images with

an image pixel size of 1048x1048. At the 10x magnification used, this translated to pixel resolutions of 1.136 μ m/pixel. Concentration gradient lengths that formed across the stagnation flow were analyzed using ImageJ software (Schneider et al., 2012). The raw intensity profile of the concentration gradient was normalized prior to data plotting. Earlier calibration experiments (Fig. 3.9) showed that the dye concentration had a direct and linear relationship to the fluorescence emitted by the dye. This implies that the concentration could be directly derived from fluorescence intensity such that:

$$\text{Normalized Concentration, } C = \frac{C_i - C_0}{C_{max} - C_0} = \frac{I_i - I_0}{I_{max} - I_0} \quad [3.2]$$

where C_i is the dye concentration measured, C_0 is the minimum concentration and C_{max} is the maximum dye concentration within the MCS device. I_i is the intensity value measured, I_0 is the minimum intensity value and I_{max} is the maximum intensity of the captured images.

From the normalized concentration profile measured, the concentration gradient length was measured as the distance between 5% and 95% of the maximum normalized concentration (see Fig. 3.10).

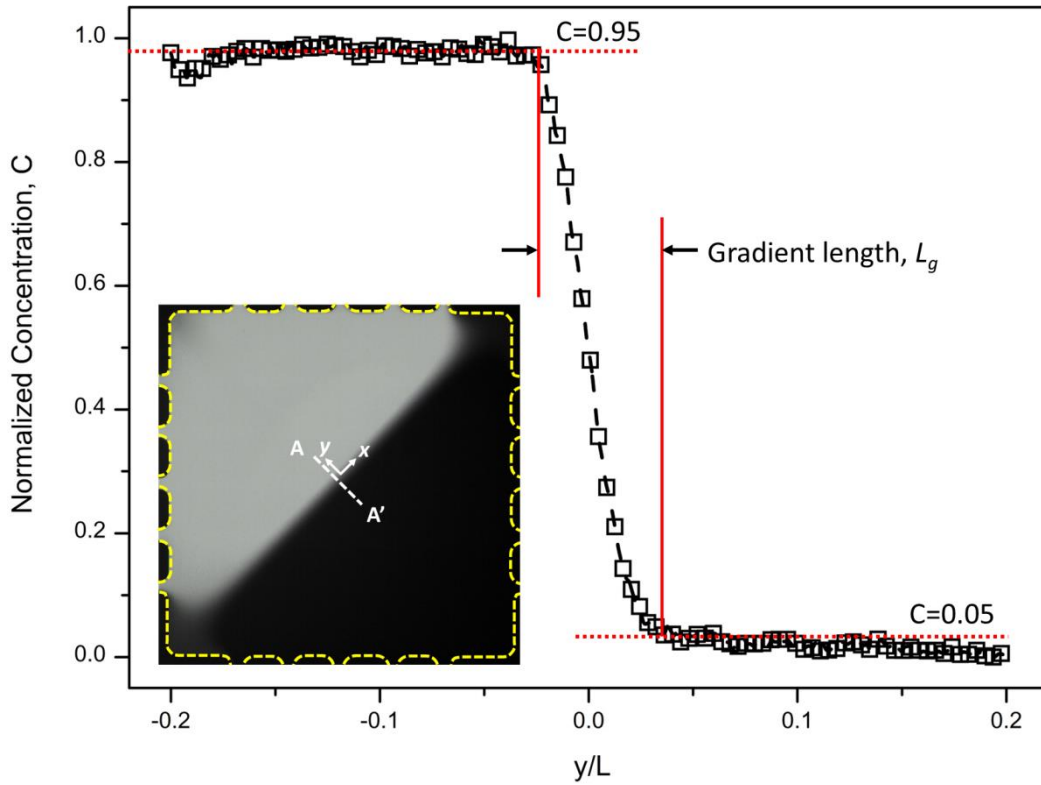


Figure 3.10 Measurement of the gradient length, L_g across the stagnation flow. The gradient length is obtained as the distance between 95% (*i.e.* $C=0.95$) and 5% (*i.e.* $C=0.05$) of the maximum normalized concentration. The abscissa of the plot is non-dimensionalized by the total diagonal length of the chamber, along the y -axis. (*Inset*) Typical grayscale image of fluorescein concentration gradient formed in MCS device; Line A-A' highlights the measurement of the concentration gradient along the y -direction.

During image processing for transient concentration gradient experiments, time-lapsed images captured the stabilization of concentration gradients across the stagnation flows. ImageJ was used to analyze the time stacked images. Briefly, a square window of 1 pixel ($1.134\mu\text{m}$ by $1.134\mu\text{m}$) was positioned in centre of the stagnation flow chamber and the concentration variation across the time stack was analyzed. Using the time intervals between images within the time stack, the

temporal change in concentration at the stagnation point was plotted with respect to the time elapsed. The time for concentration stabilization was defined as the time between 5% and 95% of the steady-state concentration value at the stagnation point location (see Fig. 3.11).

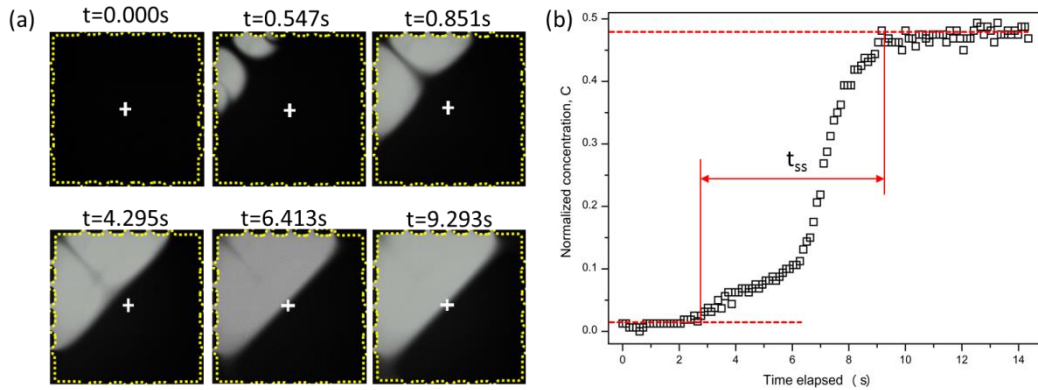


Figure 3.11 (a) Progression of fluorescein concentration stabilization across the stagnation point (marked by a white cross). (b) Plot of the normalized concentration level of the image pixel situated at the stagnation point (denoted by a white cross in (a)). The time for concentration stabilization at the stagnation point is defined by t_{ss} .

3.3.1.4 Particle image velocimetry (PIV) analysis

Stagnation flow within all the MCS device designs was visualized using carboxylated fluorescent tracer beads (2 μm diameter, Polybead, Polysciences, Inc.). 2 μm diameter tracer beads were chosen such that bead weight was negligible and bead velocity could be approximated to the velocity of the surrounding fluid. Streaklines that traced stagnation flow pathlines were obtained by digitally superimposing the individual trajectories of beads in 200 sequential images (recorded at a time intervals of 16.67ms) via ImageJ software (National Institutes of Health

Maryland, USA) (Schneider et al., 2012). Flow velocities within the MCS devices were quantified by digitally correlating image pairs that were captured at a time interval of 30ms. Images pairs were correlated using a Matlab open source particle image velocimetry (PIV) software (Thielicke & Stamhuis, 2014). Experimental error bars for the measured flow velocities or flow strains were calculated across 100 image pairs using experimental uncertainty analysis (see Appendix C).

3.4 Protocols used for biological experiments

The MCS device with cell chamber was used to compare temporal responses of *P. Aeruginosa* cells during chemotaxis. Cells were first filled into the cell chamber and their flagellum was allowed to tether to the base of the cell chamber. During chemotaxis experiments, tethered cells were exposed to a sudden change in chemoattractant concentrations in their microenvironment and their flagellum rotation responses were compared temporally. Near the stagnation point, cells could be exposed to a rapid in flow of chemoattractant or medium concentrations, without significant perturbations due to fluid shear stress. The following sections describe the cell culture and chemotaxis experimental conditions, and the microfluidic experiment and single cell image analysis processes.

3.4.1 *P. Aeruginosa* cell culture and chemotaxis

Pseudomonas aeruginosa PA01 wild-type cells from single colonies were cultured overnight in 10 ml of Luria-Bertani (LB) broth (BD Biosciences) at 37°C, 250 rpm. Cultures were diluted to O.D.₆₀₀ = 0.2 using M9 media (MP Biomedicals)

and grown at 37°C, 250 rpm until the cells reached the late-exponential growth phase at O.D.₆₀₀ = 0.8. Cell cultures were then diluted 1:10 prior to usage in microfluidic experiments. During chemotaxis experiments, 10mM of *L*-Serine diluted in M9 medium buffer was used as the chemoattractant. M9 medium was used as a buffer to provide a zero chemoattractant microenvironment around the tethered cells.

3.4.2 Experimental process and analysis of cell responses

MCS devices with a step-down cell chamber were used to determine how *P. Aeruginosa* single cells respond to sudden and sustained chemical changes in their microenvironments. In this series of experiments, a population of *P. Aeruginosa* cells was exposed to a sudden ramp-up or ramp-down in chemoattractant concentrations. During microfluidic experiments, the cells were first injected into the device and their flagellum was allowed to tether onto the bottom surface of the cell chamber. After a settling period of 5 minutes, the chamber was flushed with medium from the cell inlets. During each experiment, a population of 10 to 15 *P. Aeruginosa* cells was tethered onto the chamber surface. Of these tethered cells, ~5 to 8 cells could be found within a 200µm square at the centre of the cell chamber. Experiments were repeated for a sample size of 50 cells for both ramp-up and ramp-down conditions. Ramp-up and ramp-down in *L*-Serine chemoattractant within the cell chamber were achieved using a fluidic gating mechanism. Fluidic gating of *L*-Serine within the cell chamber was achieved via flow deflection between cell inlets and flow inlets (discussed in detail in Section 6.2). The two medium inlets (Q_m) are flowed with M9 medium and acts as flow deflection streams for the four chemoattractant flow inlets (Q_c). When $Q_c > Q_m$, chemoattractant floods into the cell chamber. When $Q_c < Q_m$, M9

medium floods the cell chamber. Toggling between these two states exposes cells to either a ramp-up or ramp-down signal in *L*-Serine concentrations. This flow deflection scheme (discussed in detail in Fig. 6.2) was used to initiate the ramp-up or ramp-down of *L*-Serine chemoattractant during chemotaxis experiments.

In order to study the adaptation of cell responses to their microenvironment, the flagellum rotation of each *P. Aeruginosa* cell was analyzed through time-lapsed imaging. At a frame speed of 40fps, single *P. Aeruginosa* cells were imaged for 120s (the duration of ramp-up or ramp-down signals). Videos of individual tethered cells were converted to grayscale and the contrast of images were improved by adjusting the saturation pixels to 0.4 using ImageJ software (Schneider et al., 2012). From the videos of individual tethered cells, the rotation profiles were extracted using an in-house bacteria tethering analysis program (*BTAP*) that was written in Matlab (Qian et al., 2013). *BTAP* was used to chart the rotation speed and frequency in which the cell rotates in either the clockwise (*CW*) or counterclockwise (*CCW*) direction. In order to quantify the rotation bias from frequency plots, a value of 1 or -1 was assigned to cells which rotate exclusively in either *CW* or *CCW* direction. This rotation bias (an assigned value ranging from 1 to -1) is quantified within a time window of 20s. The time window is moved at a time step of 0.025s, along the entire duration of the chemotaxis experiment, to measure rotation bias with respect to time.

The adaptation time of individual cells, in response to either a ramp up or ramp down in *L*-serine concentrations, was extracted from the rotation bias plots. A key characteristic of adaptation is the decay of rotation bias to pre-stimulus levels after

sustained nutrient conditions (Segall et al., 1986). The adaptation time is obtained by fitting the decay of rotation bias decay to an exponential curve. This curve is denoted by $|F| = |F_0|e^{-\frac{t}{\tau}}$, where F and F_0 are the rotation bias and the maximum value of rotation bias attained respectively. t denotes the time elapsed during chemotaxis, and τ denotes the adaptation time.

4 Steady-state and transient concentration gradient confinement through stagnation flow

In this chapter, the time and length scales of concentration gradient generation in the MCS device are quantified. Section 4.1 introduces how microfluidic devices can be used to create micro-analogs of G. I. Taylor's four-roll mill macroscale experiments and the current work in microfluidic stagnation flows. Section 4.2 covers the experimental results obtained from the MCS device and discusses the convective-diffusive (C-D) processes occurring across the stagnation flow. The C-D processes are described and quantified based on the natural length scales of the MCS device and the corresponding Péclet number. Section 4.3 discusses the dynamic C-D process across the stagnation flows. The C-D dynamics are quantified by experimental, analytical and numerical approaches. Alignment of the three approaches is discussed with a focus on determining an accurate time scale for describing C-D across the stagnation flow. Section 4.4 summarizes the results and discusses how the experimental, analytical and numerical results can be applied to extensional flows of a similar nature.

4.1 Introduction

As earlier presented in Chapter 2, the first demonstration of stagnation flows was achieved using the four-roll mill device (Taylor, 1934). Miniaturization of stagnation flows have since been demonstrated in microfluidic cross-slot devices (Deschamps et al., 2009; Hudson et al., 2004; Lee et al., 2007; Tanyeri & Schroeder,

2013). Stagnation flows, in particular those of an extensional nature, have been used to study the extensional dynamics of viscoelastic polymers (Dylla-Spears et al., 2010) and DNA (Perkins et al., 1997). Further applications of stagnation flows include trapping and steering single particles (Tanyeri & Schroeder, 2013) or cells (Johnson-Chavarria et al., 2014; Roth et al., 2013)/ vesicles (Deschamps et al., 2009). While the flow and force fields within stagnation flows have been extensively studied, mass transport of chemical species across stagnation flows is not well understood. Even lesser is known about the dynamics of competing convective and diffusive mass transport across such flows. In this section, a microfluidic analog to Taylor's four-roll mill experiments is designed. Using a highly precise and controllable microfluidic setup, the steady-state and transient confinement of chemical species across the stagnation flow is studied. Furthermore, an analytical model is sought to gain insight into convection-diffusion processes occurring at the stagnation point.

The modified cross-slot (MCS) device that was used to control stagnation flow is shown in Fig. 4.1. The MCS device consists of a main stagnation flow chamber that is connected by narrow adjoining diffusion channels that are in turn connected to a wider delivery channel. The effect of diffusion channels' widths, w , on stagnation flow characteristics was studied (see Fig. 4.1(b)). The stagnation flow experiment setup is shown in Fig. 4.1(c). In order to form a purely extensional stagnation flow within the main chamber, an equivalent flow rate, Q , is injected into each of the device inlets. The injection flow rates were adjusted using a programmable pressure pump controller. The flow rates were calibrated with respect to the pump pressure and plotted in Fig. 3.5. A symmetrical concentration flow

boundary condition was created to simplify analytical and numerical modeling of convection- diffusion processes across the stagnation point. This symmetry was achieved by injecting two inlets with fluorescein dye and the other two inlets with deionized water as shown in Fig. 4.1(c). In an effort to study the transient mass transport of fluorescein dye across the stagnation point, a flow deflection strategy was employed to purge the chamber prior to allowing fluorescein concentrations to entering the main chamber. The pump controller was programmed to first inject deionized water (C_0) into the device. In the presence of the check valves (shown in Fig. 4.1(a)), all the deionized water flows out into outlets and does not contaminate the fluorescein dye reservoirs (C_1). After a time lag of 5s, fluorescein dye is injected into the main chamber. The transient mass transport of fluorescein concentration into the chamber is recorded at $60fps$ ($16.67ms$ time interval).

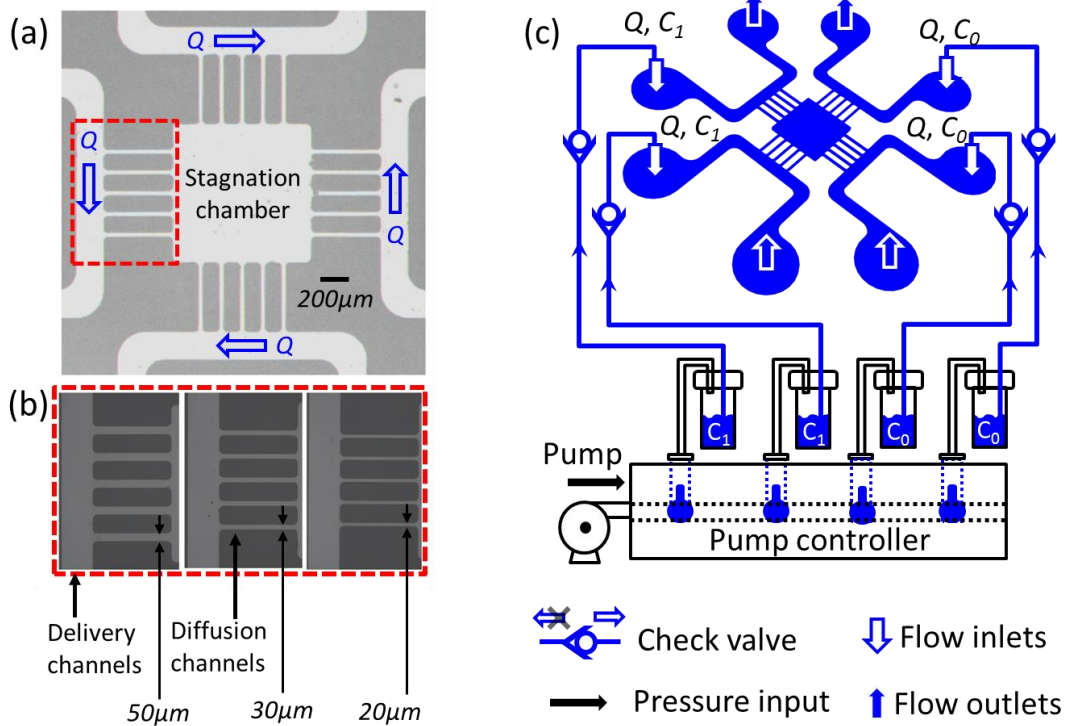


Figure 4.1 (a) Design of the modified cross-slot device with (b) zoomed-in diffusion channels (in a dotted box). Diffusion channel width, w , is varied at $50\mu m$, $30\mu m$ and $20\mu m$. (c) Flow configuration used to form stagnation flow at the centre chamber. Flow rates in all the inlets, Q , are equivalent, resulting in a stagnation point forming at the centre of the chamber. The pump controller injects fluorescein, C_I and deionized water, C_0 from the liquid reservoirs and into the device inlets.

4.2 Stagnation flow characteristics and their role in convection-diffusion mass transport

4.2.1 Stagnation flow characteristics

Stagnation flows are characterized by linear velocity gradients with respect to the flow direction. Within the MCS device, a two-dimensional stagnation flow is formed within the centre chamber as equivalent flow rates are injected into the four inlets (see Fig. 4.2(a)). The streamlines formed in Fig. 4.2(a) manifest when two opposing streams of flow enter along the y -axis (compressional axis) and leave the chamber along the x -axis (extensional axis). This flow is characterized by a linear and directionally homogeneous velocity gradient such that $\vec{v} = \dot{\epsilon}(x - y)$, where the flow strain, $\dot{\epsilon} = \frac{\partial u}{\partial x} = -\frac{\partial v}{\partial y}$. Quantification of the stagnation flow velocities was achieved by microparticle image velocimetry (μ PIV) and is shown in Fig. 4.2(b). Within the chamber, flow velocities dramatically diminish towards a local minimum—a stagnation point that is located at the centre of the chamber. Theoretically, a stagnation point is a singularity where $\vec{v}(x, y) \rightarrow 0$. However, this is not possible to

prove experimentally since flow velocities are tracked based on beads movement and each bead has a finite volume. In this series of experiments, the stagnation point is considered to be the position in which the flow velocity was ~ 4 -5 orders of magnitude smaller than the maximum velocities within the chamber. As shown in the two-dimensional velocity map (Fig. 4.2(b)), an inverted conical velocity well surrounds the stagnation point. Implicitly, this conical shape of the velocity well is the result of a flow strain rate (*i.e* velocity gradient) that is homogeneous near the stagnation point.

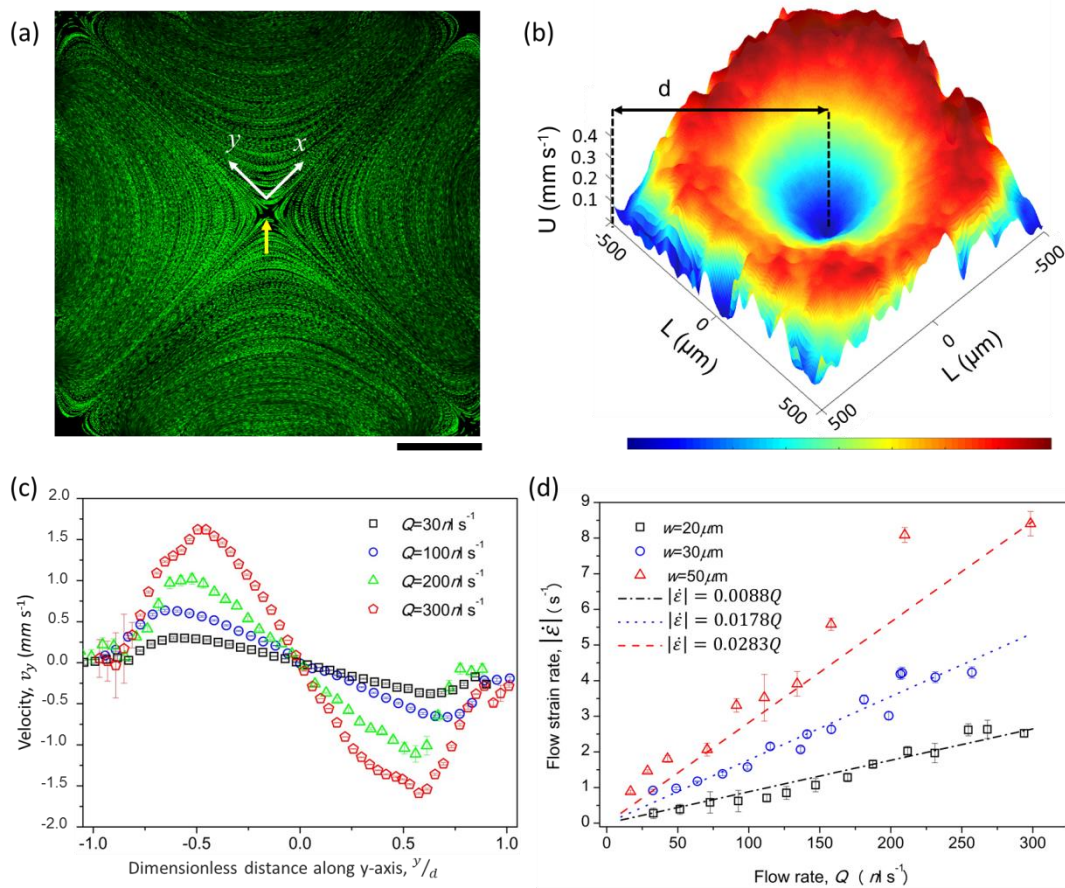


Figure 4.2 (a) Microparticle (2μm) streamlines tracing the formation of stagnation flow within the MCS device ($w=30\mu\text{m}$), at a flow rate of $Q=30\text{nl s}^{-1}$. Yellow arrow

points to stagnation point at the chamber centre. Scale bar is 200 μm . (b) Flow velocity mapping of streamlines shown in (a). Colour bar indicates a velocity range from 0 (blue) to 0.5 mm s^{-1} (red). L represents the length of the stagnation chamber ($L = 1\text{mm}$). (c) Flow velocity profiles along the y -axis that is non-dimensionalized by d , the distance between the chamber edge and the central stagnation point shown in (b). (d) Effect of flow rate on the flow strain rates produced within different MCS devices. Error bars in (c, d) were calculated from 100 image pairs using an experimental uncertainty analysis (see Appendix C for details).

Based on the μPIV measurements, the velocity gradient (or flow strain rate) was found to be linear near the centre stagnation point (Fig. 4.2(c)). Fig. 4.2(c) plots the measured flow velocities along the dimensionless distance, y/d . The velocity profiles show a disruption to the linear velocity gradient at the distal ends of the plot, corresponding to flow near the chamber corner. This edge effect is expected since corner flows are themselves known to result in the formation of stagnation points (Deen, 1998). MCS devices with different diffusion channel widths also exhibited edge effects at the chamber corners. However, for all of the MCS device designs, the velocity gradient was found to be linear near the stagnation point at a range of $-0.5 \leq y/d \leq 0.5$. Based on the experimental data, flow patterns near the stagnation point, at a limiting range of $-0.5 \leq y/d \leq 0.5$ were considered as linear flows having a homogenous flow strain rate.

Linear fitting of the flow strain rate, $\dot{\epsilon}$, within this linear flow region was plotted with respect to inlet flow rates and is shown in Fig. 4.2(d). Previous work on

stagnation flows of Newtonian fluids (Haward et al., 2013) has also reported that $\dot{\epsilon}$ has a linear dependence on injection flow rates. In Fig. 4.2(d), this linear relationship ($\dot{\epsilon} = kQ$) was empirically derived, where k has units m^{-3} and is a proportionality factor which changed as diffusion channel widths were varied. Larger diffusion channel widths allowed more flow into the stagnation chamber and resulted in higher flow velocities and velocity gradients for a given flow rate. Changing the width of the diffusion channels was found to affect the range of flow strains achievable for a given flow rate range. For example, for MCS devices with $w=20\mu m$, the flow strain rates achievable for the flow rate range of $30nl s^{-1}$ to $300nl s^{-1}$ was $0.28 \leq \dot{\epsilon} \leq 2.06$. On the other hand, for MCS devices with $w=50\mu m$, the flow strain rate achievable for the same flow rate range was $1.46 \leq \dot{\epsilon} \leq 8.41$.

During experiments, the flow strain rates that were measured from larger channel widths resulted in measurably larger errors. This is likely attributed to the finite interrogation window size selected for PIV analysis which, was used to determine the flow strain rate. An interrogation window of $22.7\mu m$ was used to track particle trajectories across time correlated images (with a sampling time of $\Delta t=16.7 ms$). At higher flow rates, tracer particles had larger trajectories and travelled out of the interrogation window between consecutive images, thereby contributing errors into the PIV analysis of the velocity profile, and hence strain rate. Alternatively, Hart has previously reported that in order to correct this PIV error, the selection of the interrogation window size can be increased, albeit at the expense of the resolution of the velocity map (Hart 2000). In order to maintain the resolution of velocity mapping in the measured flow rates, an optimized interrogation window size of $22.7\mu m$ was

used, which hence, resulted in larger errors being measured for larger diffusion channel widths.

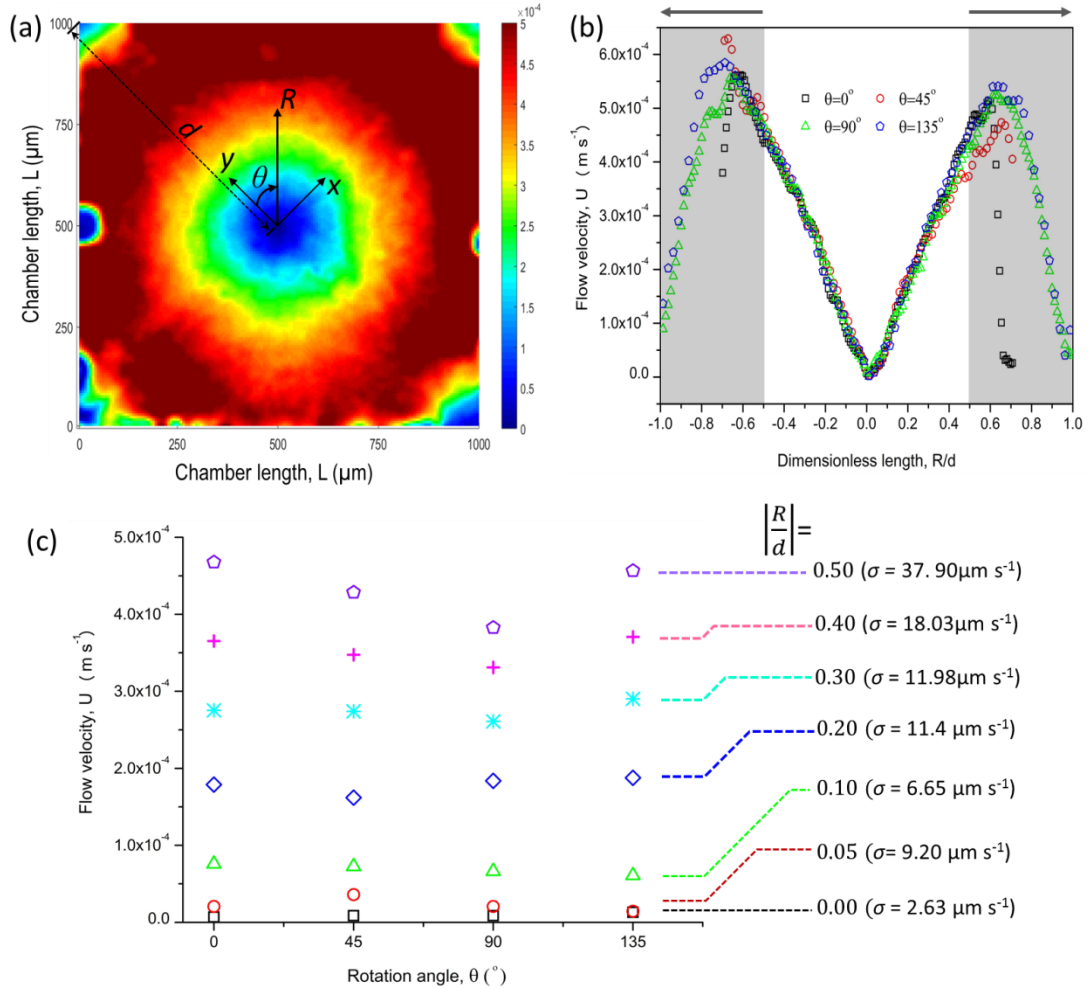


Figure 4.3(a) Formation of stagnation point flow with symmetrical velocity well. (b) Velocity profile (U) plot along the dimensionless length (R/d), for different θ values. Shaded area in plot highlights the disruption to flow velocity from the chamber wall. Arrows point towards the distal ends of the chamber. (c) Comparison of flow velocities across the rotation angle. The small velocity deviation (σ) across the rotation angles (θ), for $|R/d| = \pm 0.5$, indicate a highly symmetrical velocity profile.

Stagnation flow results in rotationally symmetric velocity profiles. An example of this symmetry is measured for the MCS device, injected with an inlet flow rate of 30 nl s^{-1} (shown in Fig. 4.3(a)). In Fig. 4.3(a), the flow velocity is measured across R for $\theta = 0^\circ, 45^\circ, 90^\circ$ or 135° . The velocity profiles along the four directions, revealed well-matched velocity profiles (see Fig. 4.3(b)). Except for edge effects from the chamber wall, the velocity well was rotationally symmetrical within the dimensionless length of $R/d = \pm 0.5$. The symmetry of the velocity well was quantified by comparing the velocity magnitudes across the rotation angles (θ) for various values of R/d (Fig. 4.3(c)). The velocity deviations across the rotation angle were typically 1- 2 orders of magnitude smaller than the measured flow velocities, indicating a highly symmetrical velocity profile.

4.2.2 Convection-diffusion mass transport in stagnation flows

Convection-diffusion processes occurring in the stagnation flow were probed by injecting fluorescein dye into the device (see flow configuration in Fig. 4.1(c)). When the fluorescein solute is injected into the device, convective flow transports the solute towards the stagnation point. As the solute approaches the stagnation point, diffusive mass transport gradually gains dominance and mass transport is characterized by the diffusion coefficient of the fluorescein solute. The diffusion-dominated mass transport near the stagnation point does not, however, reach a saturation limit as an opposing stream consisting of deionized water acts as a perpetual concentration sink. Along the y -axis, the fluorescein (source) flow stream

diffuses into the opposing deionized (sink) flow stream, resulting in the formation of a perpetually stable concentration gradient.

The coupling effect of convection-diffusion mass transport on the concentration gradient formed is mathematically defined by the mass conservation equation (earlier shown in equation [2.14]). Scaling of equation [2.14] was demonstrated earlier in Chapter 2. An analytical solution describing concentration gradient formation across the stagnation flow was derived in equation [2.33]. The validity of the derived solution was tested by comparing analytical concentration profiles with those obtained experimentally and numerically.

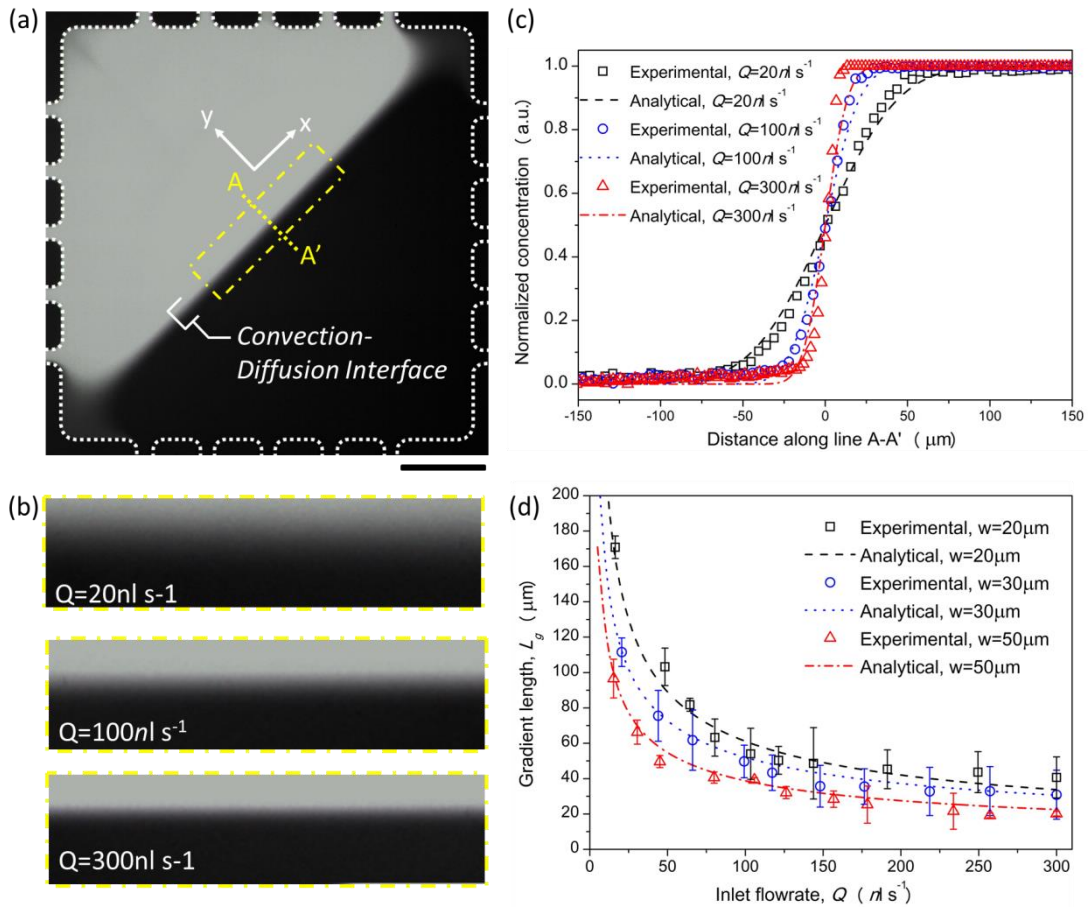


Figure 4.4 (a) Concentration gradient formed by convection-diffusion processes across the stagnation flow with an MCS design of $w=30\mu\text{m}$. Scale bar represents $200\mu\text{m}$. (b) Concentration gradients formed at different flow rates, magnified from the location of the yellow dotted box in (a). (c) Comparison between experimental and analytical concentration profiles. (d) Comparison of gradient length, L_g across different diffusion channel widths, w , for a range of flow rates. The gradient length (L_g) is determined as the distance along line A-A' that separates 5% and 95% of the normalized concentration shown in (c).

Table 4.1 Correlation fitting (R^2) between the analytically calculated and experimentally measured concentration gradient profiles.

MCS device configuration	Correlation coefficient (R^2)	
	Concentration profiles (shown in Fig. 4.3(c))	Concentration gradient lengths (shown in Fig. 4.3(d))
$w=20\mu\text{m}$	0.998	0.989
$w=30\mu\text{m}$	0.999	0.996
$w=50\mu\text{m}$	0.998	0.995

Fig. 4.4(a) shows the concentration gradient formed by injecting flow at 30nl s^{-1} into an MCS device with diffusion channel width of $30\mu\text{m}$. Experimental results show that at the convection-diffusion interface between the fluorescein solute and deionized water, an increase in flow rate results in the formation of a more steep velocity gradient, thereby reducing the interface that is dominated by diffusion. This presents itself as a reduction of the concentration gradient length as the flow rate is increased (see Fig. 4.4(b)). The concentration flow profile across the stagnation point was measured along line A-A' and plotted with respect to the analytically derived concentration profile (Fig. 4.4(d)). The concentration profile derived from equation [4.7] matches closely to the experimentally measured profiles. The correlation

coefficient (R^2) between the analytical and experimental concentration profiles was analyzed (see Table 4.1); an R^2 value of 1 represents perfect correlation between the analytical and experimental results. Correlation between the analytical and experimental concentration profiles was consistently greater than 0.998 for all the MCS devices with different diffusion channel widths. Furthermore, comparing the analytical and experimental concentration gradient lengths (Fig. 4.4(d)) registered a correlation coefficient of $R^2 \geq 0.989$ for all the MCS designs. The analytical model was found to be sensitive to flow strain rate changes that were brought about by variations in the diffusion channel widths (w).

It was found that MCS devices with the smallest diffusion channel width, *i.e.* $w=20\mu m$, achieved the largest concentration gradient length for the range of flow rates measured. Narrower diffusion channels increase the hydraulic resistance to flow entering the stagnation chamber. This results in a reduction of the flow strain rate (*i.e.* velocity gradient) which widens the interface that is dominated by diffusion. In particular, it was found that the gradient length was also affected by changing the flow strain rate due to inlet flow rate variations. Similarly, this change in concentration gradient length due to inlet flow rate variations was also closely tracked by the analytical model. The errors in gradient lengths measured were $\sim 10\mu m$. This error was likely attributed to a combination of factors such as slight dimensional variation between fabricated chips, the image resolution of the camera ($\sim 1.36\mu m/\text{pixel}$) and inlet flow rate variation ($\sim 5 \text{ nl s}^{-1}$) across experiments.

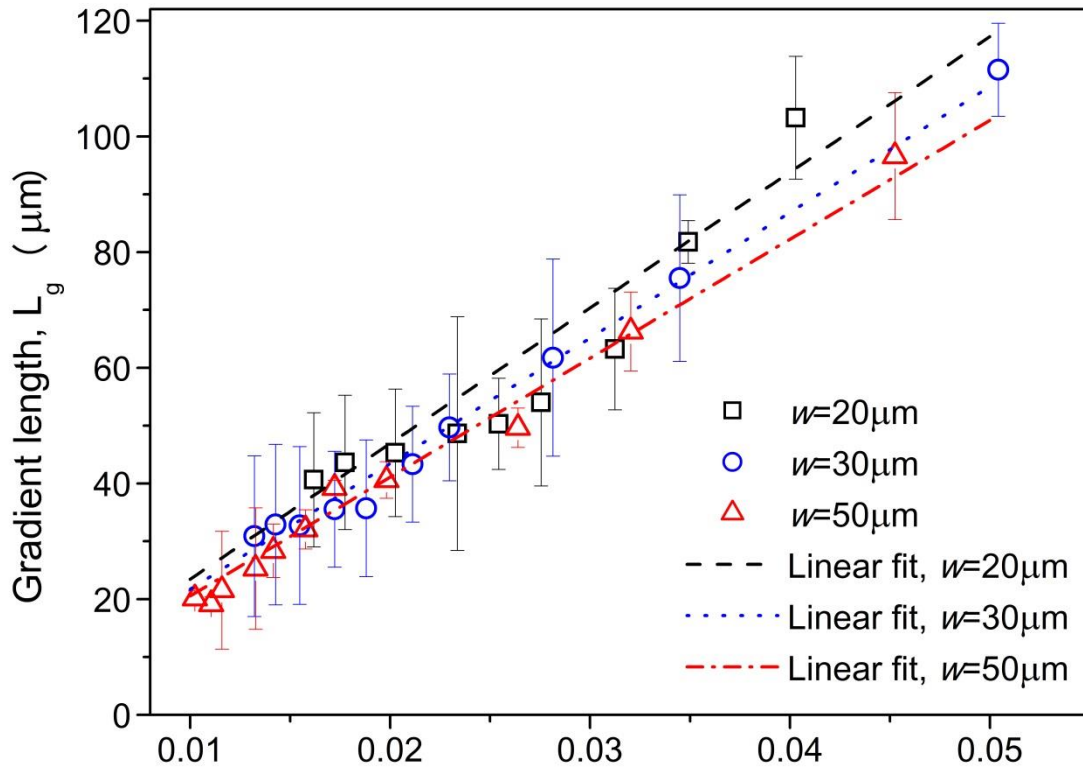


Figure 4.5 Linear correlation between the concentration gradient, L_g and the *Péclet* number, $Pé$, within the stagnation flow.

Table 4.2 Prediction of the gradient length, L_g , using the linear correlation, $L_g = C_w \sqrt{Pé}$ where C_w is an empirically derived constant for each MCS device

Diffusion channel width, w μm	C_w	Correlation coefficient, R^2
20	2345.17	0.989
30	2171.66	0.996
50	2055.51	0.995

Since convection-diffusion interface across the stagnation flow is strongly influenced by the flow strain rate, it was deduced that the concentration gradient length (L_g) formed could be defined as a function of the *Péclet* ($Pé$) number. $Pé$ is defined here as $Pé = \frac{\dot{\epsilon} d^2}{D}$, where d is the characteristic length, $\dot{\epsilon}$ is the flow strain rate and D is the diffusion coefficient of the fluorescein solute in water. In both the

experimental and analytical data, $Pé$ was found to play a determinant role in influencing the convection- diffusion process across stagnation flows (see Fig. 4.5 and Appendix D for $Pé$ values). Further analysis of the results shows a linear dependence between L_g and $1/\sqrt{Pé}$. This correlation is plotted in Fig. 4.5 and summarized in Table 4.2. The results for all the MCS device designs show that defining $Pé$ based on the flow strain rate, $\dot{\epsilon}$, can accurately predict the concentration gradient formation across the stagnation flow. This correlation with the Pé number provides direct insight into the concentration gradient formed across the stagnation point- a value not directly discernable by numerical modeling. It should however be noted that the application of the analytical model is implicitly linked to the assumption of linear flow. Thus at flow rates where the concentration gradient length exceeds the linear flow limit of $-0.5 \leq y/d \leq 0.5$, the model validity is compromised; the concentration gradient length is not only influenced by extensional stagnation flow but also by the chamber edge geometry.

4.3 Dynamics of concentration gradient formation in stagnation flows

In this section, the transient convection-diffusion (C-D) processes occurring across the stagnation flow is explored. As previously mentioned, the time-dependent C-D process was experimentally measured by employing a flow deflection technique that gated the flow of fluorescein solute into the stagnation chamber. This allowed analysis of the progressive development of concentration gradients across the stagnation flow. The time-dependent development of fluorescein concentrations

inside the chamber is shown in Fig. 4.6. The experimental results were compared to those simulated using time-dependent numerical simulations in COMSOL Multiphysics (see Section 2.4). At the stagnation point, the time required for concentration levels to reach steady state values has an inverse dependence on the inlet flow rate (*i.e* an increase in flow rate results in a decrease in the time to achieve steady-state). The time to steady-state, t_{ss} , was tracked by measuring concentration values at the centre of the stagnation chamber (shown as a white cross in Fig. 4.6(a)). As shown in Fig. 4.6(c), the time to reach steady-state was plotted with respect to various flow rates. After reaching state-state, the normalized concentration levels for MCS devices with 30 μm diffusion channels (profiles shown in Fig. 4.6(c)) had normalized concentration fluctuations of 2.40%, 1.79% and 1.15% for flow rates of 44nl s⁻¹, 100nl s⁻¹ and 22-nl s⁻¹, respectively. As such, the experimental time to reach steady-state was measured as the time lapsed from 5% to 95% of the steady state normalized concentration. For data comparisons, the analytical data was derived by calculating the reference time scale of the MCS device, $t_0 = \frac{d^2}{Pe \cdot D}$, for the flow rate range. If the time and length scales were defined appropriately, the calculated values of t_0 should exhibit a broad qualitative agreement with the experimentally extracted t_{ss} values, thereby obviating the need for extensive solutions to the transient C-D equation [4.2].

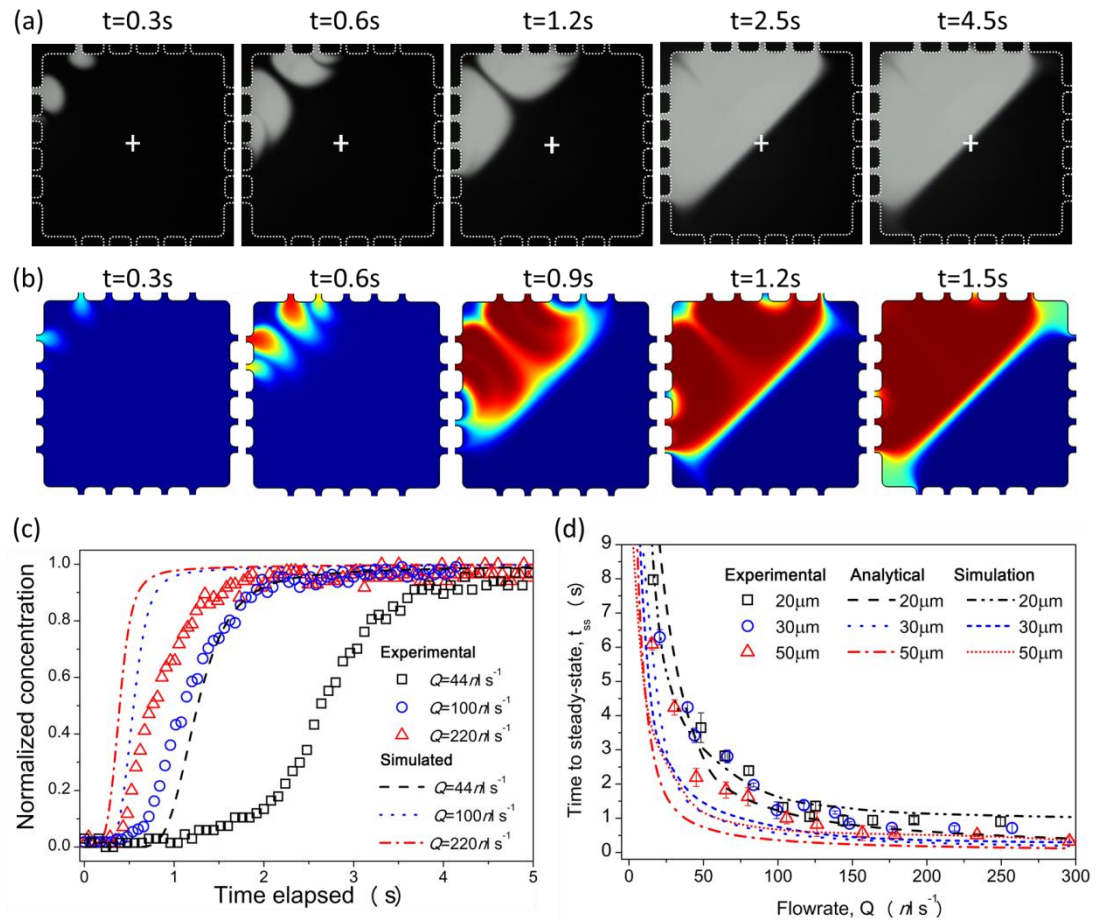


Figure 4.6 Time-dependent transport of fluorescein solute obtained through (a) experiments and (b) numerical simulations of MCS devices with $30\mu\text{m}$ diffusion channels. (c) Concentration profiles showing the stabilization of the concentration levels at the stagnation point of the MCS device with $30\mu\text{m}$ diffusion channels. (d) Effect of flow rate on the time required for fluorescein concentration to stabilize at the stagnation point.

Fig. 4.6(d) shows that the analytical model accurately predicts the order of magnitude transition of t_{ss} from $\sim O(10^1)$ to $\sim O(10^{-1})$, for the range of flow rates tested. As shown in Fig. 4.6(d), the analytical model was found to slightly underestimate t_{ss} and this is expected since velocity profiles (shown in Fig. 4.2(b, c))

indicate that velocities decrease significantly towards the corners of the stagnation chamber. As the analytical model considers a homogenous velocity profile across the y-axis, it does not account for the decrease in velocities at the chamber corners, thereby underestimating the time for a steady-state concentration to form at the stagnation point. A notable effect of this is that t_{ss} is similarly underestimated for all MCS devices sharing the same chamber geometry and dimensions. Furthermore, the numerical model was also found to closely trend the experimental and analytical results, unanimously for all the MCS device variations. In this regard, the analytical t_{ss} presented here provides a valid estimation of transient C-D processes across the stagnation flow, without executing time consuming transient numerical analysis. At the very least, this first estimation is an appropriate time scale input for performing transient numerical simulations of such extensional stagnation flows.

4.4 Summary

The dynamic characteristics associated with convection and diffusion across stagnation flows has been studied using the modified cross-slot (MCS) device to recapitulate Taylor's four roll mill macroscale experiments. Through experimental investigations, it was found that the spatial and temporal characteristics of convection-diffusion (C-D) processes across the stagnation flow were uniquely determined by the flow strain rate, $\dot{\epsilon}$, and the *Péclet* number, Pe . The simplified analytical model derived here provides a solution to C-D problems pertaining to the transportation of concentration species in similar planar extensional flows. Furthermore, the time dependent stabilization of concentration species across

stagnation flows was studied and compared to theory, highlighting the accuracy of the analytical model with proper scaling in predicting transient C-D processes. Considering the analogous relationship between mass and heat transfer processes (Bedingfield & Drew, 1950), this simplified model may draw further relevance to problems pertaining to convection- diffusion heat transfer across laminar stagnation flows.

In the next section, the formation of binary and combinational concentration gradients across stagnation flow is explored. Flow configurations within the MCS device are adjusted such that these concentration gradients can be hydrodynamically positioned by moving the stagnation flow.

5 Binary and Combinational Concentration Gradient Confinement in Stagnation Flow²

In this chapter, the formation of binary and combinational concentration gradients across stagnation flows is discussed. The MCS device with valves is used to investigate stagnation flows, the hydrodynamic spatial and temporal control of concentration gradients confined within such flows. The addition of Quake membrane valves allows rapid control in inlet flow rates, thereby facilitating hydrodynamic positioning of the stagnation point and entrained concentration gradients. Section 5.1 introduces the state-of-the-art use of stagnation flow in microfluidic applications. Section 5.2 covers the flow experiments conducted to characterize stagnation flow within this MCS device. Section 5.3 discusses the experimental and simulation results for concentration gradients confined with the velocity wells that are characteristic of stagnation flows. Section 5.4 further explores the use of velocity wells to confine and hydrodynamically position combinational concentration gradients.

5.1 Introduction

Stagnation flows have recently been demonstrated in niche applications such as the trapping and manipulation of single cells (Johnson-Chavarria et al., 2014; Nève et al., 2010), biomolecules (Dylla-Spears et al., 2010; Perkins et al., 1997; Young &

² This chapter is in part reproduced by permission of The Royal Society of Chemistry [A.G.G Toh, C. Yang, Z.P. Wang, and N-T Nguyen, *Lab Chip*, 16, pp. 368-376 (2016)].

Shelley, 2007) and nanoparticles (Tanyeri & Schroeder, 2013). In microfluidics, a direct method to generate stagnation flow is the formation of planar extensional flows in cross-slot devices (Deen, 1998; Dylla-Spears et al., 2010; Haward, 2014; Young & Shelley, 2007). In microfluidic cross-slot configurations, an extensional flow is manifested in the presence of opposing flow streams with equal velocity field strength; the interface that forms between the opposing streams intersects the axis of flow at the stagnation point (Deschamps et al., 2009; Haward, 2014; Tanyeri et al., 2011).

Stagnation flows in microfluidic cross-slot devices have been used to isolate and extend single strands of DNA (Perkins et al., 1997). Perkins *et al.* demonstrated how an extensional flow field could be used to study the non-Newtonian polymer dynamics of individual coiled and uncoiled DNA strands (Perkins et al., 1997). Recently, Johnson-Chavarria *et al.* demonstrated hydrodynamic trapping of individual *E. coli* bacterium (Johnson-Chavarria et al., 2014). While recent efforts have applied stagnation flows to confine micro/ nano- particles, the potential of stagnation flows to confine and control concentration gradients has not been fully explored. Near the stagnation point, the large velocity gradient can be exploited to balance the convection-diffusion transport processes between multiple chemical species. Chemical concentrations can be fed continuously across the stagnation point to produce perpetually stable concentration gradients that can be moved in an instance by controlling inlet flow rates. Thus far, microfluidic gradient generators have typically relied on high flow velocities to achieve the precise spatio-temporal control of concentration gradients (Nakajima et al., 2014; Toh et al., 2014). Flow

velocities have a direct correlation to the shear stresses induced on cells (Dupin et al., 2013; Shamloo et al., 2008; Shemesh et al., 2015). To this end, microfluidic devices with features such as expansion chambers (Bhattacharjee et al., 2010), hydraulic resistance networks (Gao et al., 2014), porous gels (Xu et al., 2014) and membranes (Kim et al., 2009) have been demonstrated to reduce shear effects during gradient generation. Expansion chambers reduce bulk flow velocities from inlet channels while hydrogels (Xu et al., 2014) or membranes (Kim et al., 2009) add tortuosity to the inflow path, thereby achieving similar reductions in flow velocity and induced shear stresses. Whilst these strategies reduce cell exposure to flow-induced shear stresses, they also drastically increase the time required to stabilize and move concentration gradients. In this respect, stagnation flows present as a novel approach to rapidly generate concentration gradients while limiting flow shear effects as velocity flow fields drastically diminish around the stagnation point.

In this section, the modified cross-slot (MCS) device with valves is used to demonstrate the confinement, focusing and moving of concentration gradients via hydrodynamic adjustments in stagnation flow. The stagnation flow within the MCS is characterized in terms of key parameters such as velocity gradient, length and hydrodynamic localization of the concentration gradients. In addition, the experimental data is compared to numerical simulations of the stagnation flow fields formed within the MCS. Based on these investigations, we demonstrate the use of a MCS device to generate perpetual source-sink diffusion gradients. Most notably, the MCS device achieves the suppression of flow-induced shear stresses while

simultaneously allowing the precise spatiotemporal control of concentration gradients.

5.2 Stagnation flow characteristics of the MCS device

In this section, the MCS device used consists of a fluidic layer and a valve control layer (see Section 3.1). Fig. 5.1(a) shows the microscope image of the MCS device. Briefly, the fluidic layer was designed with the standard MCS configuration consisting of four main delivery channels (of $200\mu\text{m}$ width and $12\mu\text{m}$ depth). Each of the delivery channels is connected to diffusion channels (of $30\mu\text{m}$ width and $12\mu\text{m}$ depth). The diffusion channels introduce the solutes into a $1000\mu\text{m}$ square stagnation flow chamber. The alignment and bonding between the fluidic layer and the valve pneumatic layer were achieved by following the fabrication processes of membrane-based ‘Quake valves’ (Thorsen et al., 2002; Unger et al., 2000). The orthogonal intersection between channels in the fluid layer and pneumatic layer form a ‘push-up’ valve, as shown in Fig. 5.1(a,c).

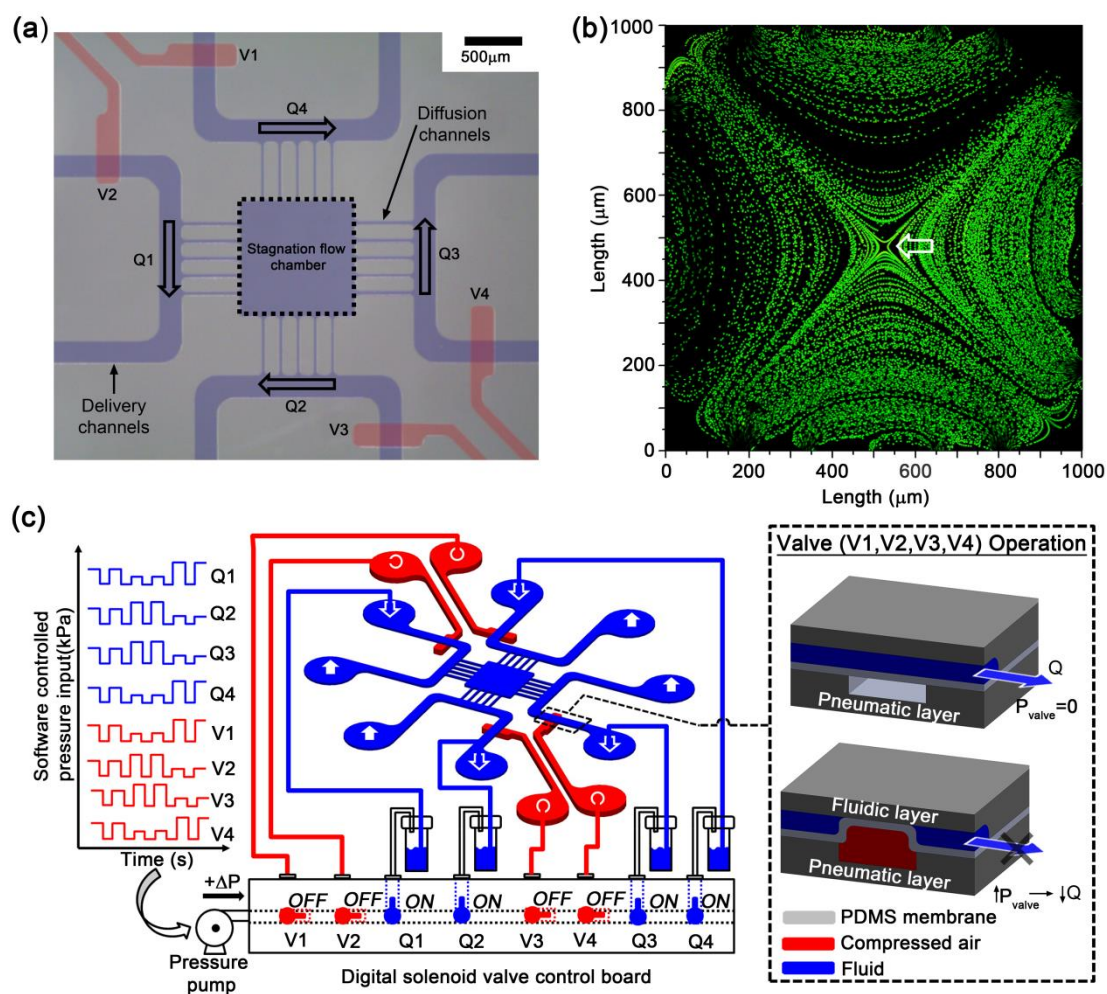


Figure 5.1 (a) Microscope image of the MCS device with a fluidic layer (filled with blue dye) and a pneumatic valve layer (filled with red dye). (b) Streakline traces of the extensional stagnation flow formed at the centre of the stagnation flow chamber. (c) Pump and flow configurations used to control stagnation flow within the MCS device. Inset shows the 3D valve configuration and valve actuation scheme that was used to hydrodynamically control the position of the stagnation point.

Within the main stagnation chamber, a stagnation point is generated by planar extensional flows resulting from the four opposing flow streams that converge in the chamber. This design allows the introduction of dual source-sink concentration pairs

into the main stagnation chamber, thereby facilitating the generation of overlapping gradients for a maximum of four different chemical species. Under symmetrical flow conditions, *i.e.* $Q=Q_1=Q_2=Q_3=Q_4$, the MCS with valves, similar to the MCS device introduced in Chapter 4, generates a stagnation point at the intersection of the four converging flows. Streakline images of stagnation flow (Fig. 5.1(a)) were obtained by digitally superimposing the trajectory of beads across 200 sequential images (recorded at a time intervals of 30ms) via ImageJ software (National Institutes of Health Maryland, USA). Bead movements shown in Fig. 5.1(a) depict a congregation of hyperbolic streaklines that surround the stagnation point at the centre of the chamber. In the vicinity of the stagnation point, linear flow dominates such that the velocity field is mathematically defined as :

$$v_x = \varepsilon x ; v_y = -\varepsilon y \quad [5.1]$$

where x and y are Cartesian coordinates corresponding to the reference frame shown in Fig. 5.2(a) and, v_x and v_y are the velocity vectors along the x and y direction, respectively. ε is the homogeneous flow strain rate derived from the linear velocity gradient near the stagnation point.

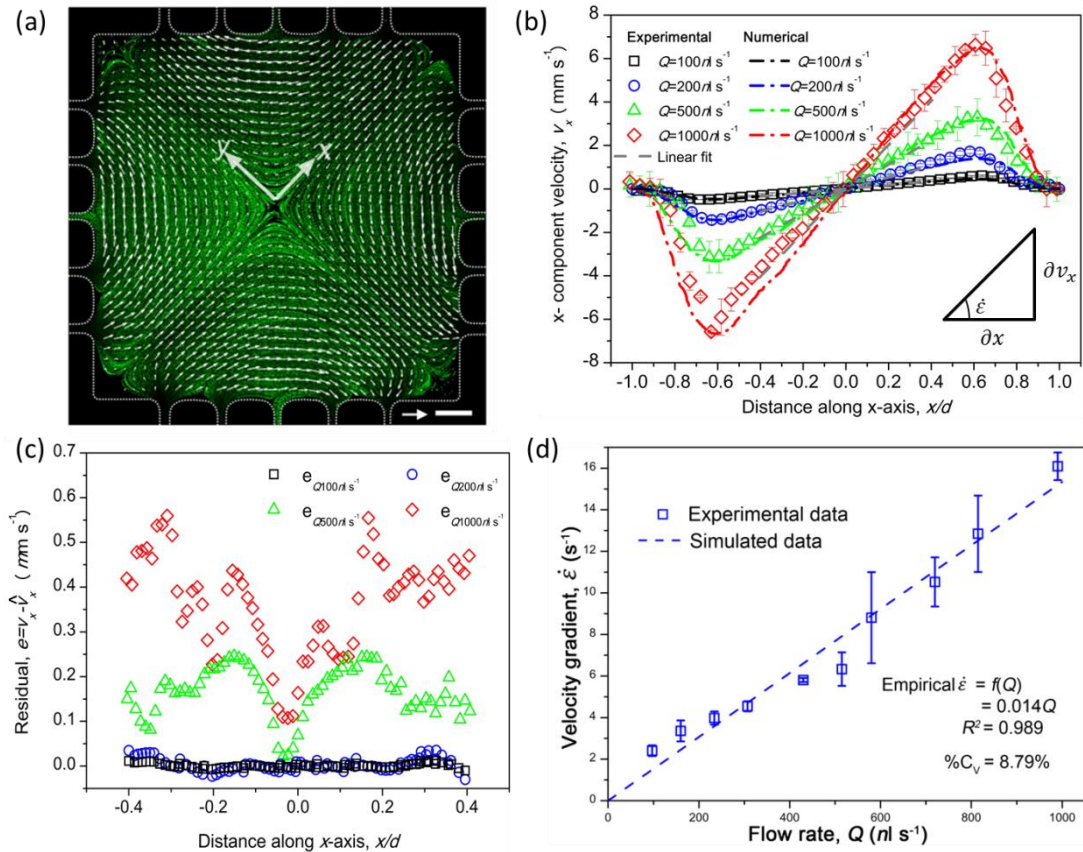


Figure 5.2 (a) Vector mapping of flow velocities within the stagnation chamber ($Q=100 \text{ nl s}^{-1}$). Arrow scale indicates velocity vector strength of 2 mm s^{-1} . Scale bar represents $100 \mu\text{m}$. (b) Velocity component (v_x) along the dimensionless x -axis (x/d) where d is half the diagonal length of the chamber. Inset in figure shows how the homogeneous flow strain rate, $\dot{\epsilon}$ is calculated from the velocity profile. (c) Residual data, e , which plots the difference between measured velocity profiles (v_x) and the linear correlations (\hat{v}_x). (d) Velocity gradient, also known as flow strain rate plotted with respect to the inlet flow rates.

Quantitative mapping of flow velocities within the device was performed by correlating particle flow image pairs and correlating the images using a Matlab particle image velocimetry (PIV) software (Thielicke & Stamhuis, 2014). Along the x -axis, the gradient of the velocity vector, v_x , also known as the homogeneous flow

strain rate, $\dot{\epsilon}$, was found to be linear near the stagnation point (see Fig. 5.2(b)). Within the length range of $-0.5 \leq x/d \leq 0.5$, the strain rate was homogeneous and the velocity gradient could be obtained by fitting the velocity profile to a linear correlation. Linear regression was applied to determine the residual between the experimental data and the fitted linear correlation. As evidenced by the small residuals along the length range of $-0.5 \leq x/d \leq 0.5$ (shown in Fig. 5.2(c)), the assumption of linear flow near the stagnation point was validated. Within this length range, the maximum residual (0.56 mm s^{-1}) was calculated for flow profiles observed at $Q=1000 \text{ nl s}^{-1}$. For the measured flow rate range, the largest residual registered at less than 8% of the maximum flow velocity for each velocity profile, validating the consideration of a homogeneous strain rate near the stagnation point.

Fig. 5.2(d) plots the relationship between the flow strain rate and the flow rate. As shown in Fig. 5.2 (d), the flow strain rate was observed to increase with flow rates in the following dependence, $\dot{\epsilon} = f(Q) = 0.0198 \cdot Q$. This linear dependence between $\dot{\epsilon}$ and Q has previously been reported for Newtonian fluids experiencing stable stagnation flows within the laminar flow regime (S. J. Haward et al., 2013). In Fig. 5.2(d), the errors in the velocity gradient were found to increase with increasing flow rate, Q . This is likely attributed to the finite interrogation window size selected during PIV analysis. An interrogation window of $22.7 \mu\text{m}$ was used to track particle trajectories across time correlated images (with a sampling time of $\Delta t=16.7 \text{ ms}$). At higher flow rates, tracer particles had larger trajectories and travelled out of the interrogation window between consecutive images, thereby contributing errors into the PIV analysis of the velocity profile, and hence strain rate. This is also in part due

to the limitations in the experiment setup, with the camera limited to a minimum sampling duration of 16.7ms. Alternatively, Hart has previously reported that in order to correct this PIV error, the selection of the interrogation window size can be increased, albeit at the expense of the resolution of the velocity map (Hart, 2000). In order to maintain the resolution of velocity mapping across the entire range of flow rates, the optimized interrogation window size of 22.7 μm was used throughout the experiments, which hence result in larger flow strain rate errors for flow rates greater than 500 nl s^{-1} .

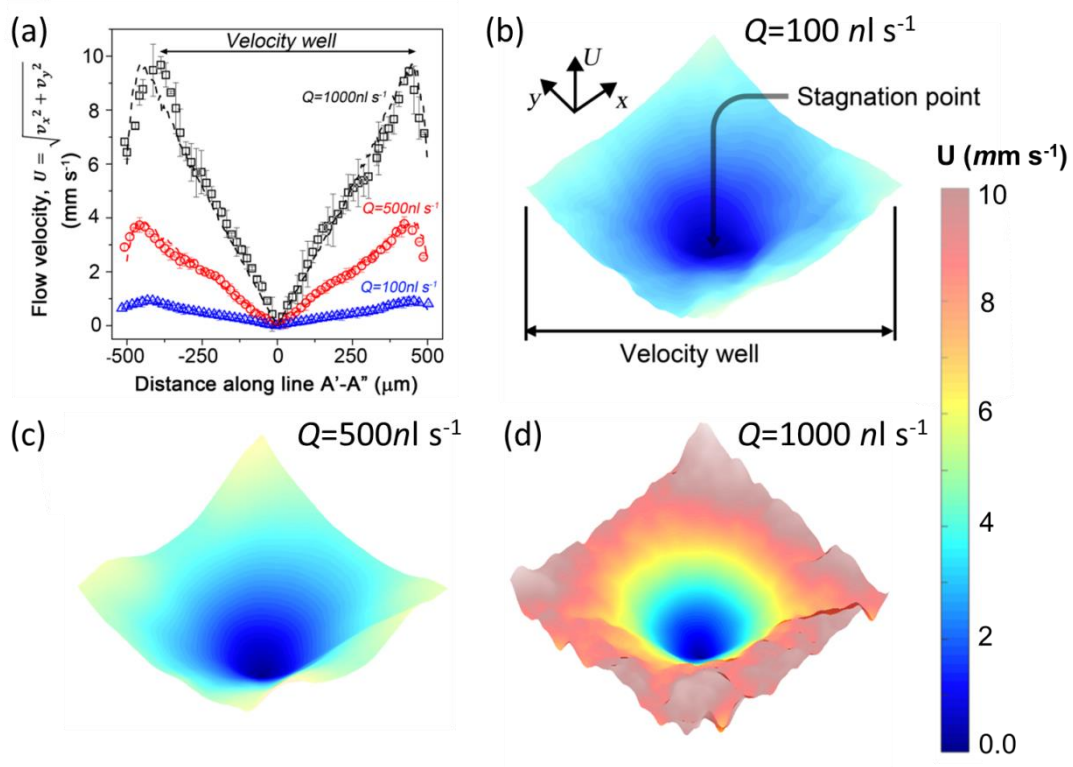


Figure 5.3 (a) Flow velocity profile measured from stagnation flows at various flow rates. (b-d) Two-dimensional velocity mapping showcasing the velocity well that increases in steepness as the inlet flow rates are increased.

Deriving the velocity magnitude, U , from the individual velocity vectors, v_x and v_y , a velocity well was found to surround the centre stagnation point (see Fig. 5.3 (a)). The velocity well is characterized by the diminishing velocity magnitudes that converge towards the stagnation point, a singularity in which the local fluid velocity is theoretically zero, *i.e.* $v(x,y)=0$. In the practical sense, it was not possible to evidence this point since velocity measurements were extracted from bead movement and trajectory. Experimentally, the stagnation point was considered to be the location at which the velocity magnitude was 4 to 5 orders of magnitude smaller than the maximum velocity magnitude within the chamber. Two-dimensional flow velocity mapping of the stagnation chamber reveals an inverted conical velocity well surrounding the stagnation point (see Fig. 5.3 (b)). This conical well is a hallmark of the presence of flow symmetry- a result of applying symmetrical flow and geometrical conditions. Further to this finding, it was observed that within the stagnation chamber, the velocity well steepness could be directly controlled by the inlet flow rates (shown in Fig. 5.3). It is conceived that the steepness of the velocity well, analogous to a potential well, could be exploited to confine and control the formation of multiple concentration gradients via convective mass transport.

5.3 Confinement of binary concentration gradients

The use of velocity wells to confine concentration gradients was demonstrated by injecting fluorescein (concentration source) into one of four flow inlets, while the other inlets were injected with water (concentration sinks). Detailed

experiment methods used were introduced in Chapter 3. At flow rates of $Q=100 \text{ nl s}^{-1}$, a steady state concentration gradient of fluorescein was formed across the velocity well surrounding the stagnation point (see Fig. 5.4 (a)). The concentration gradient formed under stagnation flow was steady and non-saturating since the source constantly replenishes concentration species towards the stagnation point (via the convective flow) while the sink removes the concentration species (via equal convective flow). In a stagnation flow, the mass transport of concentration species is characterised by the steady-state convection-diffusion equation (Deen, 1998):

$$D\vec{\nabla}^2 C = \vec{v} \cdot \vec{\nabla} C \quad [5.2]$$

where C is the mass concentration of fluorescent dye within the gradient chamber, D is the diffusion coefficient of fluorescein or Rhodamine 6G dye in water and $\vec{v} = f(\dot{\epsilon})$ is the velocity vector, described earlier in equation [5.1].

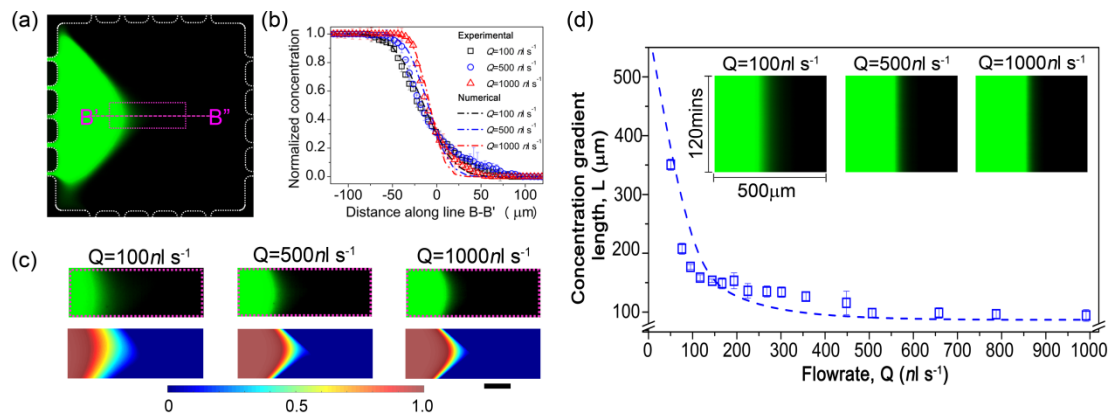


Figure 5.4 (a) Binary source fluorescein gradient across stagnation flow. (b) Concentration gradient along line B'-B'' for various flow rates. (c) Focused 2D concentration contours (from dotted box in (a)), comparing experimental (upper) and numerical (lower) concentration gradient formation. Scale bar represents 200μm for images in (c). (d) Measured concentration gradient length, L , for various flow rates.

(Inset) Time slices of concentration gradient across line B'-B'' for a time period of 2 hours. In plots (b) and (d), dotted lines represent numerical simulation results.

Mathematically, equation [5.2] shows how the steady-state concentration gradient arises due to mass conservation and the balance between diffusive mass transport ($D\vec{\nabla}^2 C$) and convective mass transport ($\vec{v} \cdot \vec{\nabla} C$). Experimentally, upon comparing the measured concentration gradient profiles (shown in Fig. 5.4(b)), the concentration gradient length (region) could be stretched or compressed across the velocity well by increasing or decreasing flow rates, respectively. The concentration gradient length measured along line B'-B'' is defined as the lateral distance that separates 5% and 95% of the normalized concentration profile. The experimental results were congruent to the simulation results shown in the two dimensional concentration contours within Fig. 5.4 (c). The relationship between the concentration gradient length, L , and the flow rate, Q , is shown in Fig. 5.4(d). Decreases in flow rates were found to elongate concentration gradients. For instance, reducing the flow rate to 50 nl s^{-1} resulted in gradient lengths of $350 \text{ }\mu\text{m}$. Au contraire, increasing the flow rate from 50 nl s^{-1} to 1000 nl s^{-1} compressed gradient lengths from $\sim 350 \text{ }\mu\text{m}$ to $94 \text{ }\mu\text{m}$. Both numerical and experimental data show the same trend such that the gradient length, L , is inversely proportional to the flow rate, *i.e.* $L \propto Q^{-1}$. On the basis of earlier data which showed that $\dot{\epsilon} \propto Q$, the data presented in Fig. 5.4(d) implicitly show that the gradient length is inversely related to the steepness of the velocity well where $L \propto \dot{\epsilon}^{-1}$. This demonstrates that velocity gradients surrounding stagnation points can be used to effectively tune concentration gradients. Thus, a reduction in flow rates would further reduce the velocity gradient

and in turn, effectively widen the concentration gradient formed. On the other hand, it was also found that for $Q > 800 \text{ nl s}^{-1}$, the gradient length was limited by a finite mass transfer boundary layer of $\sim 92 \mu\text{m}$. Similar gradient length scales have previously been reported in convection dominated microfluidic devices for biological assays (Huang et al., 2015). In order to test the temporal stability of the concentration gradient, the concentration gradients were observed over a period of 2 hours. Image slices of the fluorescein gradient along line B'-B'' were extracted from a sequential stack of images taken every 18 seconds. These slices were then appended onto one another to illustrate the variation in concentration gradients over a duration of 2 hours (shown as inset images in Fig. 5.4(d)). The insets in Fig. 5.4(d) indicate the stability of concentration gradients formed at various flow rates, highlighting the stability of concentration gradients confined by stagnation flow.

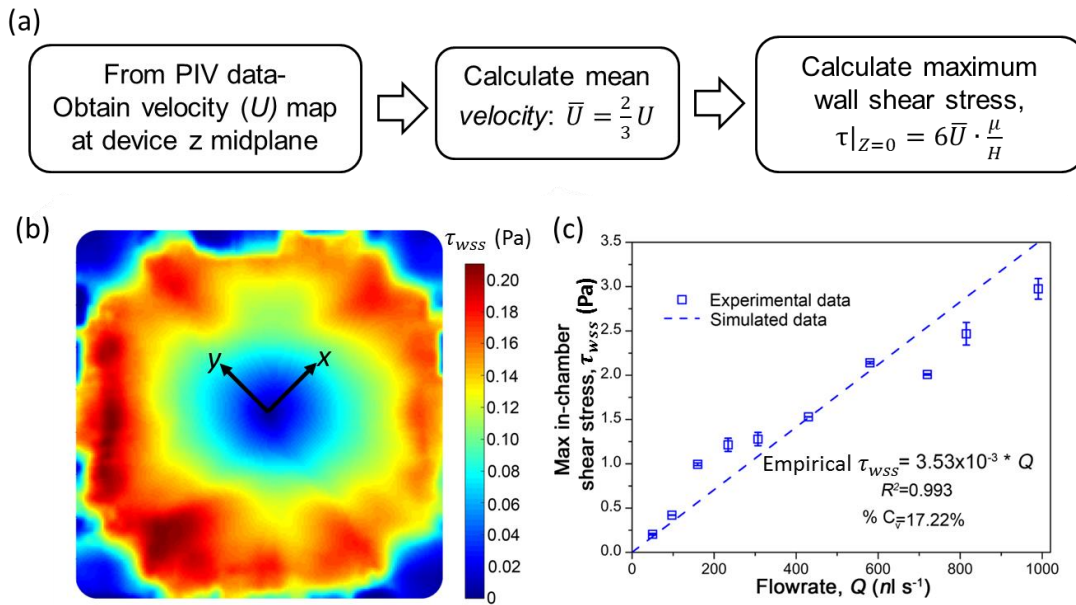


Figure 5.5 (a) Flow chart of work flow for deriving maximum wall shear stresses from PIV maps of flow velocities. (b) Shear stress contour map of the stagnation

chamber for a flow rate of $Q=50 \text{ nls}^{-1}$. (c) Maximum flow-induced shear stresses for various inlet flow rates. c_v measures the % variation between the measured and numerical wall shear stress.

One of the key benefits of confining concentration gradients within stagnation flow is the ability to maintain a steady-state concentration gradient at low shear stress conditions. The experimental velocity magnitude ($U = \sqrt{v_x^2 + v_y^2}$) obtained from PIV measurements was used to determine the wall shear stress. The maximum shear stress (τ_{wss}) induced by fluid flow within the stagnation chamber is mapped from the flow velocity data (Chuang & Wereley, 2007; Poelma, et al., 2008). The flow chart shown in Fig. 5.5(a) illustrates the work flow for calculating the wall shear stresses from PIV data. Due to the height (H) of the stagnation chamber being many folds smaller than the length (L) of the square stagnation chamber (*i.e.* $H/L=15/1000=0.015$), parallel plate calculations of wall shear stresses was applied. Considering Poiseuille's law for the pressure-driven flow, the wall shear stress was calculated as $\tau_{wss} = 6\bar{U} \cdot \frac{\mu}{H}$, where $\bar{U} = \frac{2}{3} \cdot U$, μ is the fluid viscosity and H is the depth of the chamber. Based on these calculations, the maximum wall shear stress map correlates directly to the flow velocity map and is shown in Fig. 5.5 (b). Maximum chamber shear stresses were found to linearly increase with the inlet flow rate, exhibiting a dependence on flow rate such that $\tau_{wss} = 3.53 \times 10^{-3} Q$. The empirical and numerical data were found to be in close agreement, with a 17.22% variation across the flow rates measured. Stagnation flows at $50 \text{ nl s}^{-1} < Q < 1000 \text{ nl s}^{-1}$ resulted in low in-chamber flow shear stresses ranging from $0.2 < \sigma < 2.9 \text{ Pa}$ (shown in Fig. 5.5 (c)), indicating that different shear stress ranges could be directly targeted by

modulations to flow rates. This finding, along with our earlier data presented on velocity wells highlights the use of stagnation flows to augment the mass transport of chemical species, while effectively suppressing flow shear stress effects.

5.4 Hydrodynamic positioning of combinational concentration gradients

In stagnation flow confinement of concentration gradients, hydrodynamic positioning of the stagnation flow (and entrained concentration gradients) was achieved by varying the flow rate ratios between ($Q_1=Q_4=Q_{1,4}$) and ($Q_2=Q_3=Q_{2,3}$) (flow configurations follow that shown in Fig. 5.1(c)). Actuating the valve pairs $V_1=V_2=V_{1,2}$ or $V_3=V_4=V_{3,4}$ adjusts the flow rate ratio between $Q_{1,4}$ and $Q_{2,3}$. The valve pairs are actuated when pneumatic pressure is applied to the control channel, causing the valve membranes to deflect and reduce the flow entering the stagnation chamber (see Fig. 5.1(c)). Consequently, the adjusted flow ratios allow hydrodynamic positioning of the stagnation point- and entrained concentration gradients. During hydrodynamic positioning, the inlet flow rate is adjusted by the extent of valve actuation (or the valve actuation pressure). As earlier presented in the experimental methods (see Section 3.3.1.1.2, Fig. 3.8), valve actuation was used to adjust inlet flow rates ranging from $Q= 50\text{nl s}^{-1}$ to 1000nl s^{-1} . Varying the flow rate ratio in this manner allows positioning the stagnation flow along the y- axis (see Fig. 5.6). In order to characterize the movement of the stagnation flow with respect to the flow rate ratio, we scaled the flow rates by introducing a non-dimensionalized flow factor, \tilde{f} where $\tilde{f}=(Q_{1,4}-Q_{2,3})/(Q_{1,4}+Q_{2,3})$. Programming the actuation pressure of the

valve pairs adjust the flow rates into the stagnation flow chamber and produces the desired flow factor for dynamic localization of the stagnation point (see Fig. 5.6(a)). In Fig. 5.6(b), stagnation point positions were quantified from the velocity maps and plotted with respect to the flow factor, \tilde{f} . Along the y -axis, the positioning of the stagnation point can be predicted by a linear relationship such that $\tilde{y} = 2.56 \tilde{f}$. Numerical data (dotted line plot in Fig. 5.6(c)) agree well with the experimental data to within 2.6%.

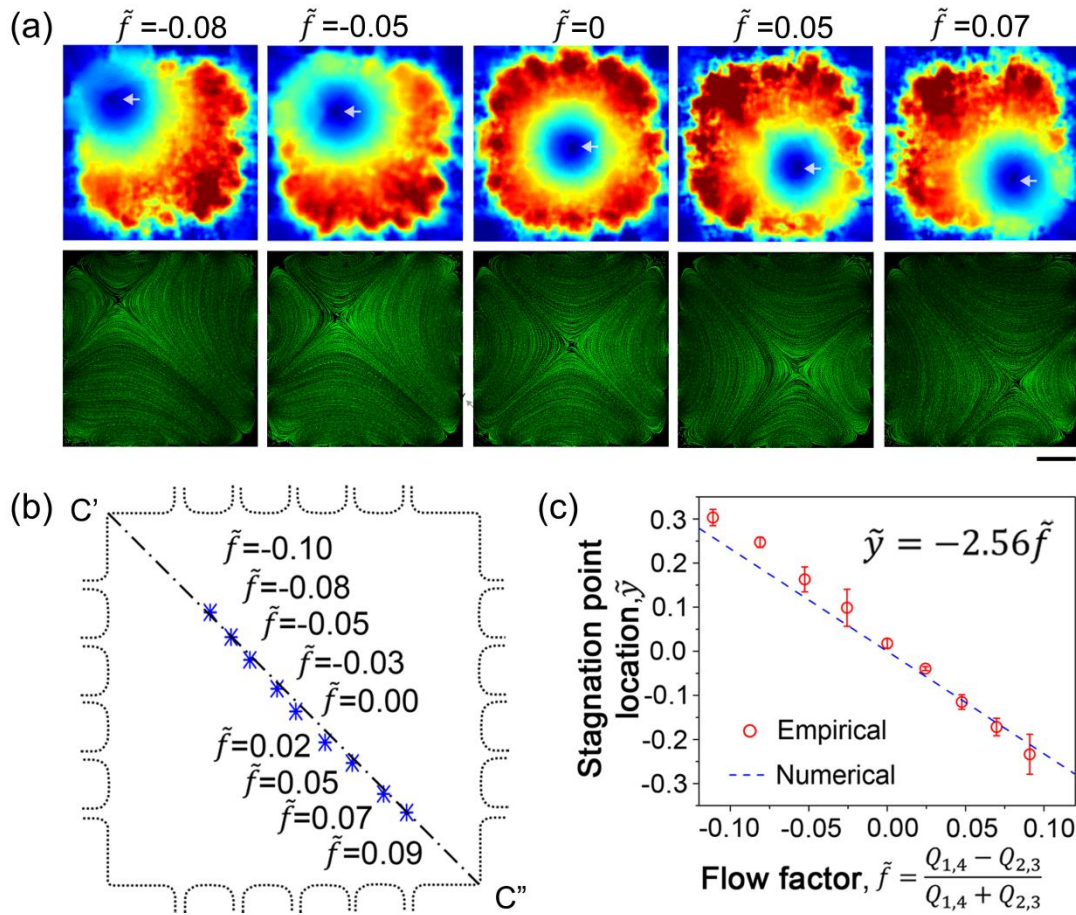


Figure 5.6 (a) 2D velocity maps (*top*) and streakline images (*bottom*) highlighting the variation of the stagnation point with the non-dimensionalized flow factor, \tilde{f} . Circular velocity wells are present around the stagnation point as they are moved

across the chamber along the line C'-C''. White arrows indicate the stagnation point location. Scale bar represents 200 μ m. (b) Locational map of stagnation point translation along line C'-C''. (c) Characterization plot of stagnation point location, \tilde{y} with respect to flow factor, \tilde{f} . The stagnation point location, \tilde{y} is scaled using the length of line C'-C'' such that $\tilde{y} = y/(C' - C'' \text{ length})$.

Using the flow factor, the hydrodynamic localization of stagnation flow allows the control and positioning of entrained concentration species. The confinement of combinational concentration gradients with fluorescein (green) and Rhodamine 6G (red) dyes is shown in Fig. 5.7, with respect to the applied flow factors.

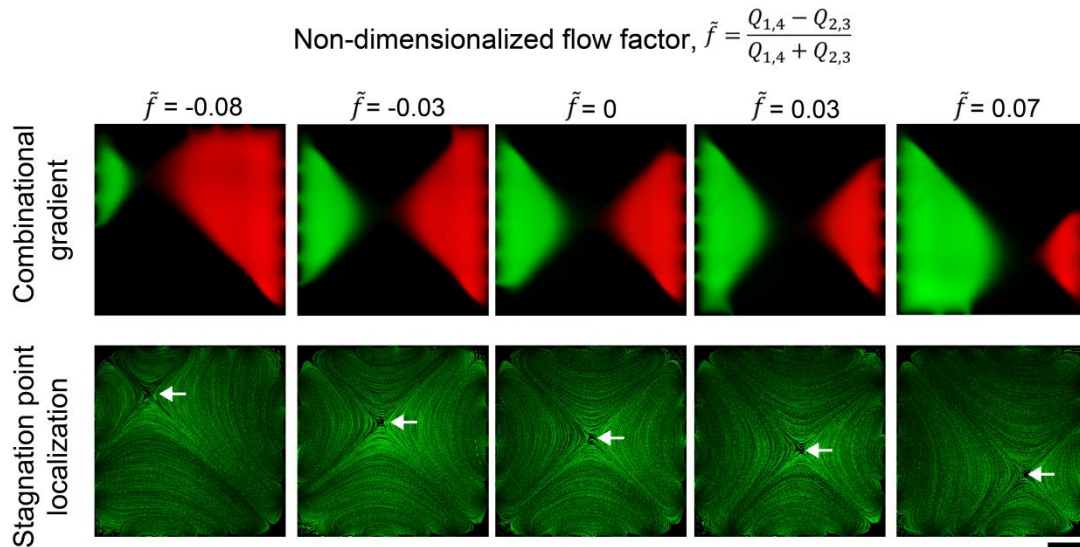


Figure 5.7 (*Upper*) Confinement of fluorescein and rhodamine 6G overlapping concentration gradients as stagnation flow is tuned with respect to the flow factor. (*Lower*) Localization of stagnation point with flow factor adjustment. Arrows point to stagnation point location for each non-dimensionalized flow factor, \tilde{f} . Scale bar represents 200 μm for images.

During experiments, it was found that dynamic positioning of the entrained combinational concentration gradients could be performed in a smooth manner, allowing real-time adjustment to be made to combinational concentration landscapes across the stagnation chamber.

5.5 Summary

In this chapter, the confinement of combinational and dynamically tunable concentration gradients was demonstrated across stagnation flow patterns. On the basis of the theoretical relationship between the flow rate, flow strain rate and the convection-diffusion equation, concentration gradient lengths were demonstrated to be directly tunable by stagnation flows. More notably, concentration gradients were directly tunable by the steepness of velocity wells that surrounded the stagnation point. Based on our device design, velocity wells across the stagnation point effectively balanced the convective flow and diffusion of concentration species within the chamber, creating a permanently sustained concentration gradient. Further to this analysis, it was found that hydrodynamic adjustments to the flow rates

allowed binary or combinational concentration gradients to be positioned within the chamber.

In particular, it was demonstrated that the MCS was able to dynamically establish concentration gradients while maintaining low in-chamber shear stresses. While prior gradient generators have demonstrated the reduction of shear flow through the addition of shear relief structures like expansion chambers, membranes or gels, these structures in turn hamper the speed at which concentration gradients can be tuned or moved. The use of velocity wells in stagnation flow addresses the mass transport problem of quickly moving binary and combinational concentration gradients, while inducing low shear flow. Furthermore, such a gradient generation scheme can be used to quickly stabilize rapidly decaying gradients of small molecules while maintaining low in-chamber shear stresses, surpassing the saturation limitations of gel-based low shear gradient generators. The device structure should be well suited for biological studies involving dynamic cell sensing (Guo et al., 2013) as concentration gradients can be rapidly targeted to or away from cells of interest, based on real-time experimental observations. It should be noted, however, that the application of stagnation flows to control concentration landscapes may not be suitable for non-Newtonian or viscoelastic solutions as such solutions exhibit flow instabilities under certain circumstances. (Arratia, Thomas, Diorio, & Gollub, 2006; S. J. Haward & McKinley, 2013) Nonetheless, the MCS device and its demonstrated use is a direct method to hydrodynamically focus and move combinational concentrations on-demand, providing a novel approach to achieving low shear stress combinational gradients in a two-dimensional landscape.

In the next section, the rapid delivery of concentration species within stagnation flow is used in the study of *P. Aeruginosa* individual cells. In particular, the biophysical adaption response of *P. Aeruginosa* individual cells is studied.

6 Dynamic Concentration Signalling for Studying Individual Cell Sensing

In this chapter, stagnation flow within the MCS cell chamber is analyzed and applied to study the chemotactic kinetics of *P. Aeruginosa* cells located near the stagnation point. The temporal and shear stress attributes of stagnation flow make it ideal for extracting dynamic chemotaxis information from individual cells, in a fluid environment that is unperturbed by shear. Through precise microfluidic control of stagnation flow dynamics, the kinetics of chemotactic adaptation in monotrichous *P. aeruginosa* bacteria were extracted from individual cell tethering assays. The findings suggest that *P. Aeruginosa* cells exhibit markedly different adaptation kinetics as compared to that of model *E.coli* bacteria. In this chapter, section 6.1 introduces the field of work and the manner in which the MCS is applied to study chemotaxis adaptation in *P. Aeruginosa* cells. Section 6.2 presents experimental findings related to the temporal and shear stress characteristics of stagnation flow within the MCS device. Section 6.3 discusses the adaptation responses of individual *P. Aeruginosa* cells within a population and section 6.4 summarizes the key findings from using stagnation flows to study *P. Aeruginosa* adaptation.

6.1 Introduction

Chemotaxis is a universal phenomenon amongst microorganisms, eukaryotic and prokaryotic cells (Eisenbach, 2004). The tendency for living organisms to move

from less to more favorable environments is basic and ubiquitous, although intrinsically complex. Key strides have been made in understanding the multiple and sometimes, simultaneous processes occurring in prokaryotic cells during chemotaxis. For example, in the model bacteria, *Escherichia coli* (*E. coli*), receptors sense chemical stimuli in the microenvironment and initiate multiple feedback loops that change the probability in which the flagella rotate clockwise (CW) or counterclockwise (CCW). The flagella rotation determines whether *E. coli* moves erratically (tumble phase) or swims (runs) in response to the stimuli present (Berg, 2004). Further to this understanding, it is now widely accepted that during chemotaxis, *E.coli* makes short term comparisons of the stimuli and over time, exhibits chemotactic adaptation under sustained stimuli exposure (Block, Segall, & Berg, 1982; Clausznitzer, Oleksiuk, Løvdok, Sourjik, & Endres, 2010; Min et al., 2012; Spiro, Parkinson, & Othmer, 1997). When cells are exposed to a sudden chemical change in their microenvironment, they dynamically respond by altering their swimming behavior. This alteration does not, however, manifest indefinitely and subsequently, over time, cells adapt and recalibrate their swimming behavior to prestimulus states. It is believed that the temporal response rescaling and shift in sensitivity is important for cells to navigate their environments over a broad range of background stimuli concentrations (Lazova, Ahmed, Bellomo, Stocker, & Shimizu, 2011). New studies have further shown that the sensitivity shift in *E.coli* is attributed to composition changes in the flagella motor and that this adaptative remodeling may be a common feature in other molecular machines (Yuan, Branch, Hosu, & Berg, 2012).

While the adaptation kinetics of *E.coli* has been widely studied, far less is known for monotrichious ('single flagellum') bacteria such as *P. Aeruginosa*. *P. Aeruginosa*, having a single flagellum, as opposed to a bundle (as in the case of *E. coli*), have different flagella rotation behaviours. *P. Aeruginosa* cells harvested at the late stage growth were 1-3 μ m in length. These cells are monotrichious (having a single flagellum of diameter approximately 100nm) and direct their movement by the bias of their flagellum rotation. Motility and chemotaxis in monotrichious bacteria such as *P. Aeruginosa* is unclear, except for current evidence that points to a 'run-reverse-turn' mechanism for cell motility (Qian et al., 2013). Further to this narrative, studies have shown that the chemosensory system and flagellar apparatus arrangement in the *Pseudomonas spp.* may be significantly more complex than other bacterial species (Doyle, Hawkins, & McCarter, 2004; Kato, Kim, Takiguchi, Kuroda, & Ohtake, 2008). For example, in *Pseudomonas aeruginosa*, five gene clusters operate during chemotaxis, as compared to *E.coli* which operates a singular gene cluster (Kato et al., 2008). Additionally, *P. Aeruginosa* possess two sets of flagellar stators as opposed to one set for *E.coli*. In light of these differences, it is not known if a unified model of chemotactic adaptation would be observed in *P. Aeruginosa* cells.

Of fundamental consequence in accurately measuring the adaptation kinetics of *P. Aeruginosa* is the ability to deliver temporally precise chemoattractant stimuli to cells while, maintaining a flow environment that minimizes perturbation effects on flagellar rotation. In previously reported adaptation experiments on single *E.coli* cells, a Y-microchannel was used to control a temporal ramp input of chemoattractant

signals; the study conceded that flow shear had decreased run and tumble durations by 10% and 20%, respectively (Min et al., 2012). Within microfluidic devices, high flow velocities significantly influence cell chemotaxis due to the shear stresses induced on cells (Min, Mears et al. 2012; Nakajima, Ishihara et al. 2014). A greater understanding of shear effects on flagella rotation has recently been furnished (Rusconi, Guasto, & Stocker, 2014). Particularly, at shear stresses ranging from 2.23mPa- 8.90mPa, bacteria chemotaxis is suppressed, with cells preferring sessile drifting (and biofilm formation) instead of free swimming (Rusconi et al., 2014). In this respect, stagnation flow provides the platform for understanding chemotactic adaptation without hydrodynamically induced shear effects. Stagnation flow fields have been demonstrated in the cross-slot (Dylla-Spears et al., 2010) and modified cross- slot (MCS) device (G. G. A. Toh, Yang, Wang, & Nguyen, 2016). Stagnation flows generated within the MCS device exhibit the existence of dramatically decreasing flow velocities (*i.e* a flow velocity well) surrounding the stagnation point. Near the stagnation point, cells that are exposed to a sudden wave of chemoattractant flow do not experience the excessive brunt of flow shear.

In this work, stagnation flow is used to apply a rapid ramp-up and ramp-down concentration step of the chemoattractant *L*-Serine and to monitor the chemotactic adaptation of tethered cells located near the stagnation point. Most notably, with the stagnation flow platform, bacteria motility data from a population of freely moving cells was successfully extracted at a high temporal resolution (of 40Hz) revealing the intricacies of chemotactic adaptation kinetics. The rotational profiles of tethered cells were quantified in the presence and absence of *L*-Serine. More specifically, the

adaptation time for cell responses to ramp-up and ramp- down stimuli was characterized and compared. The data suggests that cell adaptation response is unique for *P. Aeruginosa* and does not exhibit the adaptation features reported for peritrichous bacteria like *E. coli*. These results could be used to construct a physical model for how monotrichous bacteria, by varying the rotational direction and duration of their single flagella, respond and adapt to changes in chemical cues in their micro-environment.

6.2 Chemoattractant ramp signaling through stagnation flow

Stagnation flow was generated within the MCS device (see Fig. 6.1(a)) and used to produce the temporal concentration ramps shown in Fig. 6.1(b). The ramp up (Fig 6.1(c)) and ramp down (Fig. 6.1(d)) of *L*-Serine concentrations were reliably controlled through flow deflection. When a ramp up in *L*-Serine concentration was exposed to tethered *P. Aeruginosa* cells, the chemoattractant flow inlets (denoted by green arrows in Fig. 6.1(c, d)) experience markedly higher flow rates than that in medium flow inlets (denoted by blue arrows in Fig. 6.1(c, d)). Conversely, when a ramp down in *L*-Serine was required within the stagnation flow chamber, the medium inlet had a markedly higher flow rate than the chemoattractant flow inlets. During ramp-up and ramp down signaling, rotational profiles of individual *P. Aeruginosa* cells were measured through time-lapsed microscopy. Features of flagella rotation such as cell rotation speed and rotation phase frequency were

thereupon extracted for a population of 50 cells (see Fig. 6.1(e)). Details of the protocols used in this work can be found in the experimental section 3.4.

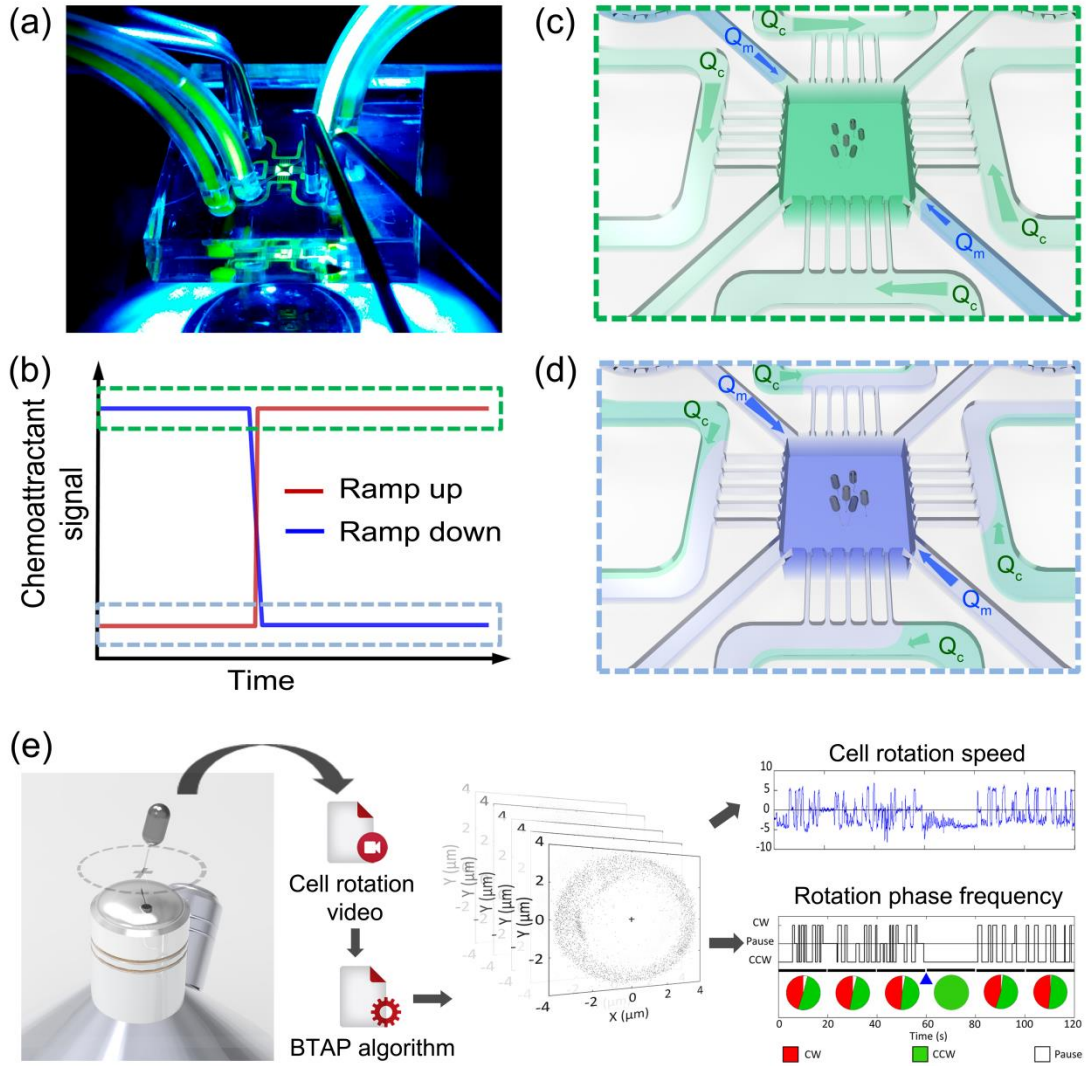


Figure 6.1 Microfluidic and chemotaxis protocol used during experiments. (a) Image of flow within main chamber when chemoattractant (visualized here using fluorescein dye) is introduced into the main chamber. (b) Temporal ramp up and ramp down signals experienced by cells within the main chamber. To generate a ramp up in chemoattractant concentration, Q_c is set at higher flow rate than Q_m , allowing chemoattractant to enter the chamber (c). To generate a ramp down in chemoattractant to enter the chamber (d). To generate a ramp down in

chemoattractant concentration, Q_m is set at a higher flow rate than Q_m , allowing medium to flush out chemoattractant from the chamber (d). (e) During the process of ramping chemoattractant concentrations, individual tethered cells within a central $100\mu\text{m}$ square periphery of the velocity well, are observed using time-lapsed microscopy. The cell rotation videos (population size of 50 cells) are entered into a bacteria tethering analysis program (*BTAP*) to extract information such as cell rotation speed and rotation phase frequency for each individual cell.

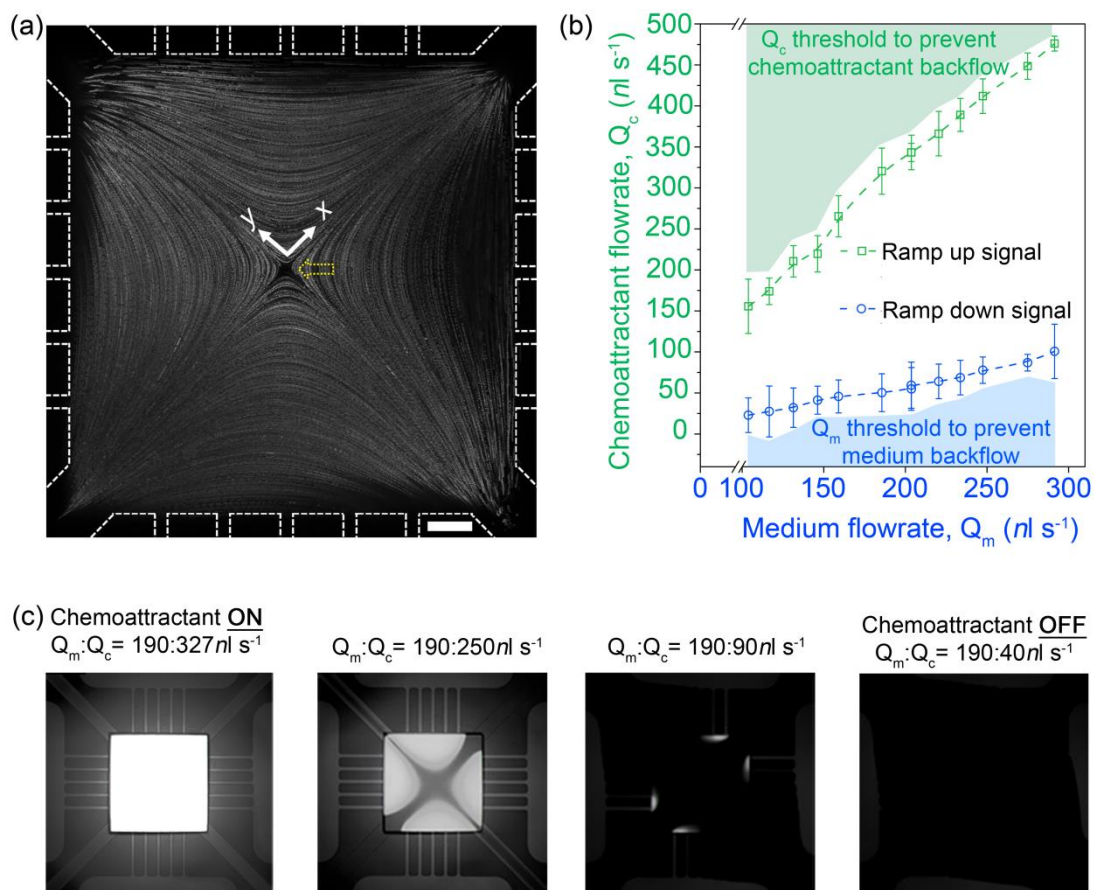


Figure 6.2 Stagnation point formation and concentration signal gating within the stagnation flow chamber. (a) Streakline image of stagnation flow with a yellow dotted arrow pointing to the stagnation point in the centre of the chamber. Scale bar represents 100 μm . (b) Corresponding flow rates for chemoattractant, Q_c , and medium, Q_m , that were used to either ramp up or ramp down the chemoattractant concentration within the stagnation chamber. (c) Example of how flow rate ratios influence chemoattractant concentrations within the stagnation chamber.

Prior to conducting chemotaxis experiments using the MCS device, stagnation flow generation of concentration ramps within the cell chamber was first characterized. In this device, stagnation flow is generated at the intersection between four converging laminar streams (Fig. 6.1(c)), resulting in a single stagnation point

being formed at the centre of the chamber (Fig. 6.2(a)). Surrounding this stagnation point, the flow streamlines shown in Fig. 6.2(a) are defined by the velocity potential function:(Deen, 1998).

$$\varphi(x, y) = \frac{\dot{\varepsilon}}{2}(x^2 - y^2) \quad [6.1]$$

where $\dot{\varepsilon}$ (s^{-1}) is the flow strain rate and, x and y are the spatial co-ordinates with reference to the stagnation point shown in Fig. 6.2(a). Equation 6.1 mathematically defines the velocity well surrounding the stagnation point since $v(x, y) = \nabla\varphi(x, y)$ and $v \rightarrow 0$ as $x, y \rightarrow 0$.

During chemotaxis experiments, stagnation flows were synchronized to gate ramp-up and ramp-down concentrations of *L*-Serine within the cell chamber. Fig. 6.2(b) plots the threshold flow rates for toggling the ramp up or ramp down chemoattractant signal within the stagnation chamber. Toggling between the two flow rate thresholds facilitated the dynamic exposure of ramp-up and ramp-down signals to cells tethered in the stagnation chamber. Flow in the two medium inlets (Q_m) acts as flow deflection streams for gating the four chemoattractant inlets (Q_c). The corresponding flow rate thresholds used to generate ramp up or ramp down chemoattractant concentration states is shaded in either green or blue respectively (Fig. 6.2(b)). Fig. 6.2(c) shows how the flow rate ratio of Q_m and Q_c is adjusted to gate the chemoattractant between ramp up and ramp down thresholds. For instance, when flow deflection streams (Q_m) are set at 123nl s^{-1} , Q_c is toggled to 190nl s^{-1} and 30nl s^{-1} respectively, to initiate *L*-Serine ramp up and ramp down concentration

states. This flow deflection technique was found to be extremely robust and could reversibly switch the nutrient landscapes surrounding cells, within several milliseconds. In addition, flow deflection guaranteed that bacteria tethered in the stagnation chamber were completely shielded from the chemoattractant prior to chemotaxis experiments, without the additional control burden of mechanical valves. It was noted, however, that varying flow rates beyond the flow rate thresholds could result in contamination of either the chemoattractant or M9 medium inlet streams. As a precaution, miniature check valves (barbed check valves, Nordson Medical) were added to inlet tubings to prevent any possible backflow and contamination of either buffer or chemoattractant streams.

6.3 Resolving temporal and shear effects during signal ramps

Once the stagnation flow and flow deflection parameters were determined, further experiments were conducted to validate that cells' rotations were not convoluted by flow shear effects during chemotaxis. Consequently, the paradox of mass transport is encountered- higher flow rates increase the temporal resolution in which concentration ramping could be controlled but also introduces shear effects on flagella rotation. To minimize the shear effects, cell rotation was analyzed within a square 100 μ m window at the centre of the stagnation chamber. During control experiments, at flow rates greater than 220nl s⁻¹, deterrence in flagella rotation was frequently evidenced. When flow rates were increased beyond 220nl s⁻¹, the tethered cells stopped rotating and aligned themselves along the flow direction. This

observation corroborates recent studies of bacteria transport in high shear environments (Rusconi et al., 2014). At this threshold flow rate, particle velocimetry was conducted to determine the maximum flow velocity, and hence, the corresponding shear stress within the observation window. The wall shear stress, τ_{wss} , was calculated from the near- wall velocities ($z \sim 6\mu\text{m}$) such that $\tau_{wss}|_{z=0} = 6\bar{U} \cdot \frac{\mu}{H}$, where the mean velocity \bar{U} is 2/3 of the measured flow velocity, U . The flow velocities within the $100\mu\text{m}$ observation window is shown in Fig. 6.3(a), for a flow rate of $Q_c = 190\text{nl s}^{-1}$. Maximum shear stresses within the $100\mu\text{m}$ observation window were quantified for both ramp up and ramp down chemoattractant signals and are plotted in Fig. 6.3(b). The maximum shear stress was found to increase in unison with the maximum flow velocity, as flow rates were increased. At the threshold flow rate of 220nl s^{-1} , the maximum shear stress experienced by bacteria within the observation window was $\tau_w = 2.43\text{mPa}$. This value corresponds closely to that previously reported ($\tau_{reported} = 2.23\text{mPa}$) for *P. Aeruginosa* cells experiencing suppressions in chemotactic responses due to flow shear (Rusconi et al., 2014). Factoring flow shear effects into the microfluidic assay, flow rate ratios for ramp up and ramp down signaling were set at $Q_c:Q_m = 190:123\text{nl s}^{-1}$ and $Q_c:Q_m = 40:193\text{nl s}^{-1}$, respectively.

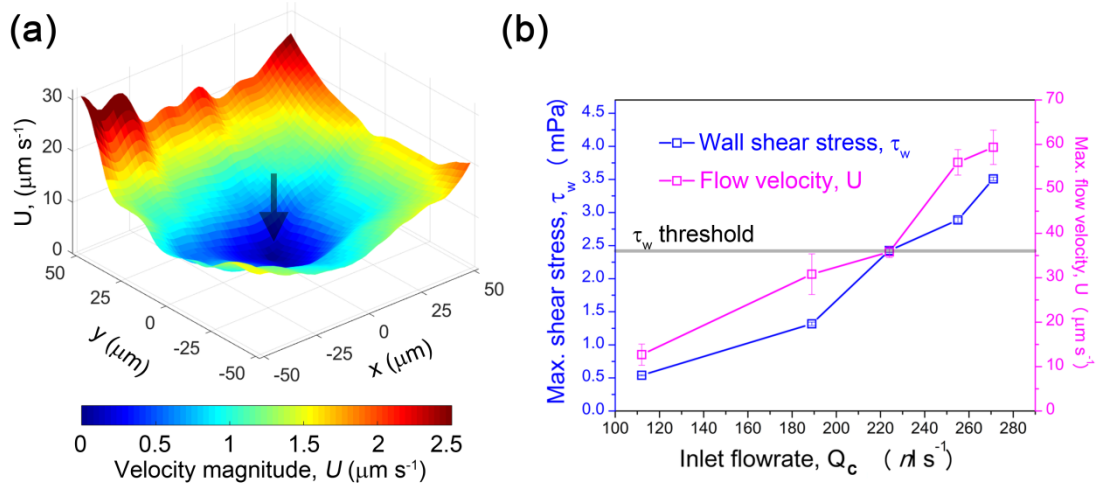


Figure 6.3 Shear stress induced by flow velocities during the onset of bacteria motor stalling. (a) Velocity mapping within the observation window for the chemoattractant flow rate of $Q_c=190\text{nl s}^{-1}$ (arrow points to the central stagnation point) and (b) Maximum flow velocities and corresponding wall shear stresses, τ_{wss} , with respect to the chemoattractant flow rate. Bacteria rotation experiences stalling at a threshold flow rate of $Q_c=220\text{nl s}^{-1}$ (*i.e.* $\tau_{wss}=2.43\text{mPa}$).

Applying the afore-mentioned flow rate ratios, the temporal characteristics of ramp up and ramp down chemoattractant signals were measured. Fig. 6.4(a) shows the progressive filling of chemoattractant into the chamber ($Q_c=190\text{nl s}^{-1}$) during ramp-up signalling. Images in Fig 6.4(b) show the filling of buffer into the chamber (at $Q_m=123\text{nl s}^{-1}$) during ramp-down signalling. The dynamic filling of the stagnation chamber was tracked along five indicator points within the observation window and is shown in Fig. 6.4(a). Fig. 6.4(c,d) plots the temporal change in concentrations experienced by cells across the five locations. During the onset of chemoattractant signalling, the coefficient of variation (c_v) was evaluated to determine the variation in chemoattractant concentrations experienced by tethered bacteria, at each location, for

the duration of ramp-up or ramp-down signals. The maximum c_v for ramp-up and ramp-down signalling was calculated and found to be 3.7% and 3.3% respectively (see Appendix E for c_v calculations). The tethered bacteria within the observation window experienced temporally equivalent chemoattractant concentrations, with variations of 3.7% or less- highlighting the precise temporal signaling achieved in the microfluidic assay. In Fig. 6.4 (e), the time to reach steady-state, τ is plotted with respect to the inlet flow rate, Q . Shorter τ was achieved when flow rates were increased. In this series of experiments, it is likely the errors associated with τ measurements were attributed to shifts in the stagnation point. Prior characterisation of stagnation point movement (Fig. 5.6(a)) quantified this shift to a spatial limit of $x,y \sim 5\mu\text{m}$. This slight shift in stagnation point locations could account for the error distribution in τ . During chemoattractant and medium filling, the ramp up and ramp down τ was $3.08 \pm 0.83\text{s}$ and $3.47 \pm 0.31\text{s}$, respectively. For both ramp up and ramp down temporal profiles, concentration signals reached their respective steady-state by approximately 3s. This is considered to be the temporal resolution of the microfluidic chemotaxis assay.

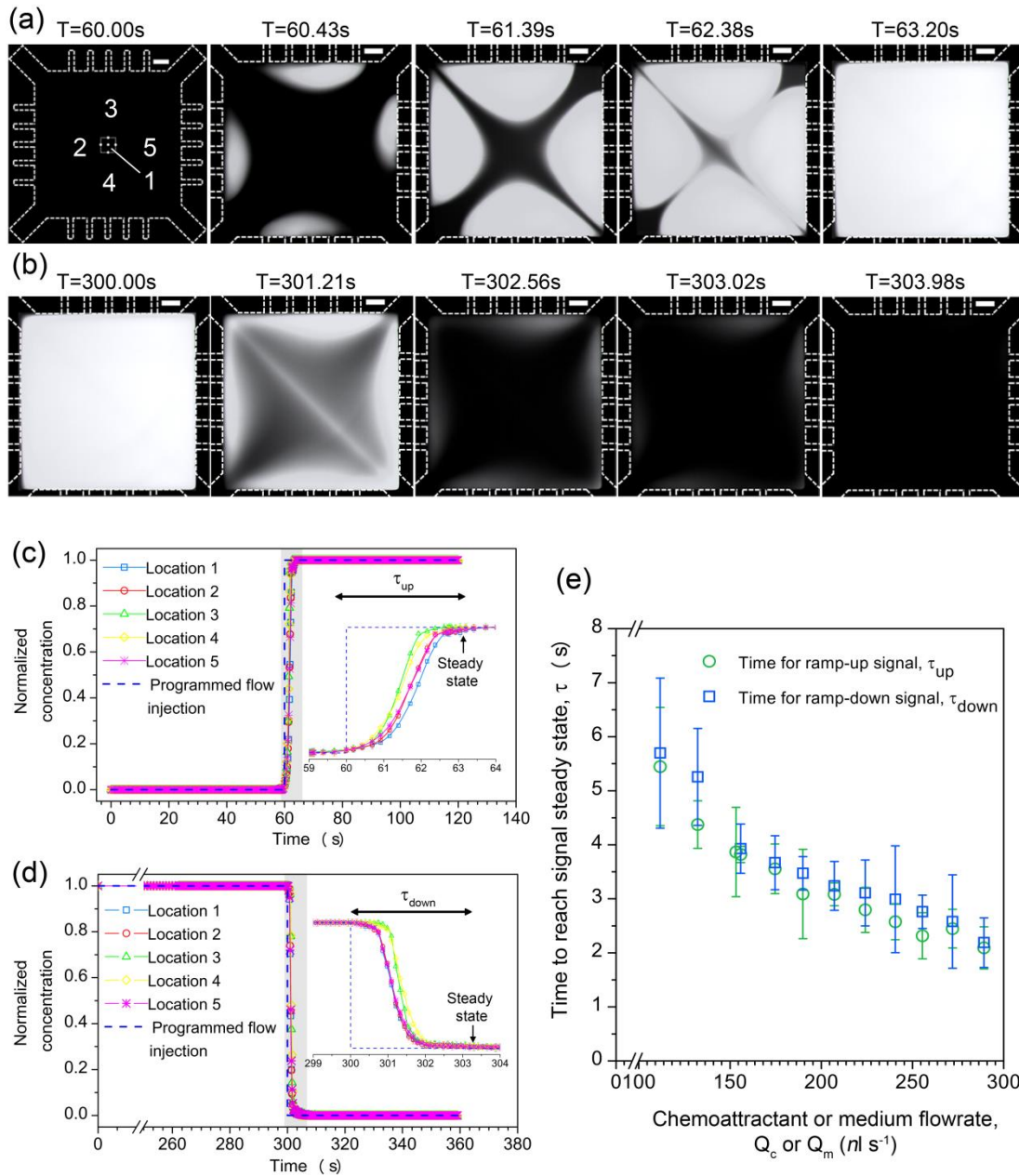


Figure 6.4 Stagnation flow dynamics resulting in precisely controlled steady state ramp-up and ramp-down chemoattractant signalling. (a) Progressive filling of chemoattractant ($Q_c = 190 \text{ nl s}^{-1}$) into the stagnation chamber during ramp-up signalling and (b) filling of medium ($Q_m = 123 \text{ nl s}^{-1}$) into the stagnation chamber during ramp-down signalling. (c) Ramp-up and (d) ramp-down signal steady state response across five locations of the observation window shown in (a). Insets in (c)

and (d) are concentration profiles with zoomed-in time scales. (e) Time required for ramp-up or ramp-down signal to completely fill the chamber. Scale bars in images (a, b) represent 100 μ m.

6.4 Population based chemotaxis and chemotactic adaptation of individual *P.Aeruginosa* cells

Chemotactic ligands such as *L*-serine are detected by *P.Aeruginosa* cell surface chemoreceptors known as methyl-accepting chemotaxis proteins. These proteins sense extracellular stimuli such as *L*-serine levels and produce intracellular signals which control flagella rotation. Fig. 6.5 shows the chemotactic responses of single *P. Aeruginosa* cells during ramp-up and ramp-down exposure of the *L*-Serine chemoattractant. The rotational behavior of cells within the observation window was derived from time-lapsed images of cell rotation movies (see Fig. 6.5(a)). The images capture the tethered cells in either of three rotational states- clockwise (CW), counterclockwise (CCW) or pause. The rotation of cells, in response to chemoattractant ramp conditions was subsequently recorded over time (Fig. 6.5(b)). Analyzing the trajectories using Matlab determined the cell rotational speed and rotation phase duration for individual *P. Aeruginosa* cells (plotted in Fig. 6.5(c-f)). The frequency of rotational phase occurrence (in CW, CCW or pause) is then averaged across a 20s time window and is presented in the pie charts shown in Fig. 6.5(d) and Fig. 6.5(f).

The ramp-up exposure of *L*-Serine to cells is first discussed (see Fig. 6.5(c,d)). During ramp-up exposure, the cell's microenvironment was initially filled with M9 medium for 60s and subsequently rapidly exposed to a ramp in *L*-Serine concentration. During the first 60s, cells spend roughly equivalent durations in either CW or CCW rotational phases. This rotational behavior is similar to that previously reported for tethered *P. Aeruginosa* cells, in the absence of chemoattractants (Qian et al., 2013). However, upon sensing the abrupt ramp in *L*-Serine concentrations after 60s, the cells immediately exhibit a strong bias in rotational direction as shown in Fig. 6.5(d). This rotational bias can occur in either CW or CCW directions and is dependent on the rotation direction at which the cell senses the ramp in chemoattractant concentrations. This bias in rotation allows the cell to continue moving towards the favorable environment as it makes short-term comparisons of temporal changes in its environment. Particularly interesting is what happens when the *L*-Serine concentration is maintained. After ~22s upon *L*-serine exposure, the biased rotational profile ceases and cells return to their pre-stimulus state of spending equivalent durations in CW or CCW directions. A meaningful comparison of the effect of *L*-Serine ramp exposure can be made when juxtapositioned with experiments involving the ramp-down of initial *L*-Serine exposure (see Fig. 6.5 (e,f)). During ramp-down experiments, cells were first exposed to *L*-Serine chemoattractant for a longer duration of 5mins to elicit a post-adaptation response where cell have adapted back to having a symmetrical CW-CCW rotational profile. Following this, the ramp down assay is performed by exposing cells to the chemoattractant for 60s and subsequently flooding the main chamber with M9 medium. This creates an abrupt depletion of chemoattractant concentration around

the cells. Fig. 6.5(e,f) shows the chemotactic response and adaptation of cells after the depletion of chemoattractant within their surroundings. Analyzing Fig 6.5(e) closely, a reversal in rotation phase is seen when the environment becomes less favourable to the cells. This reversal in direction is expected as cells make short-term comparisons of their nutrient landscape and change their rotation direction to move away from less favorable surroundings. After a reversal in its rotation direction, the cells persist in the new rotation direction (*CCW*) for approximately 20s, before exhibiting post-adaptation responses of spending equivalent durations in *CCW* and *CW* phases. Cells experiencing abrupt enrichment or depletion of chemoattractant within their microenvironment reveal the presence of chemotactic adaptation (which manifests as a adaptation back to pre-stimulus rotational states).

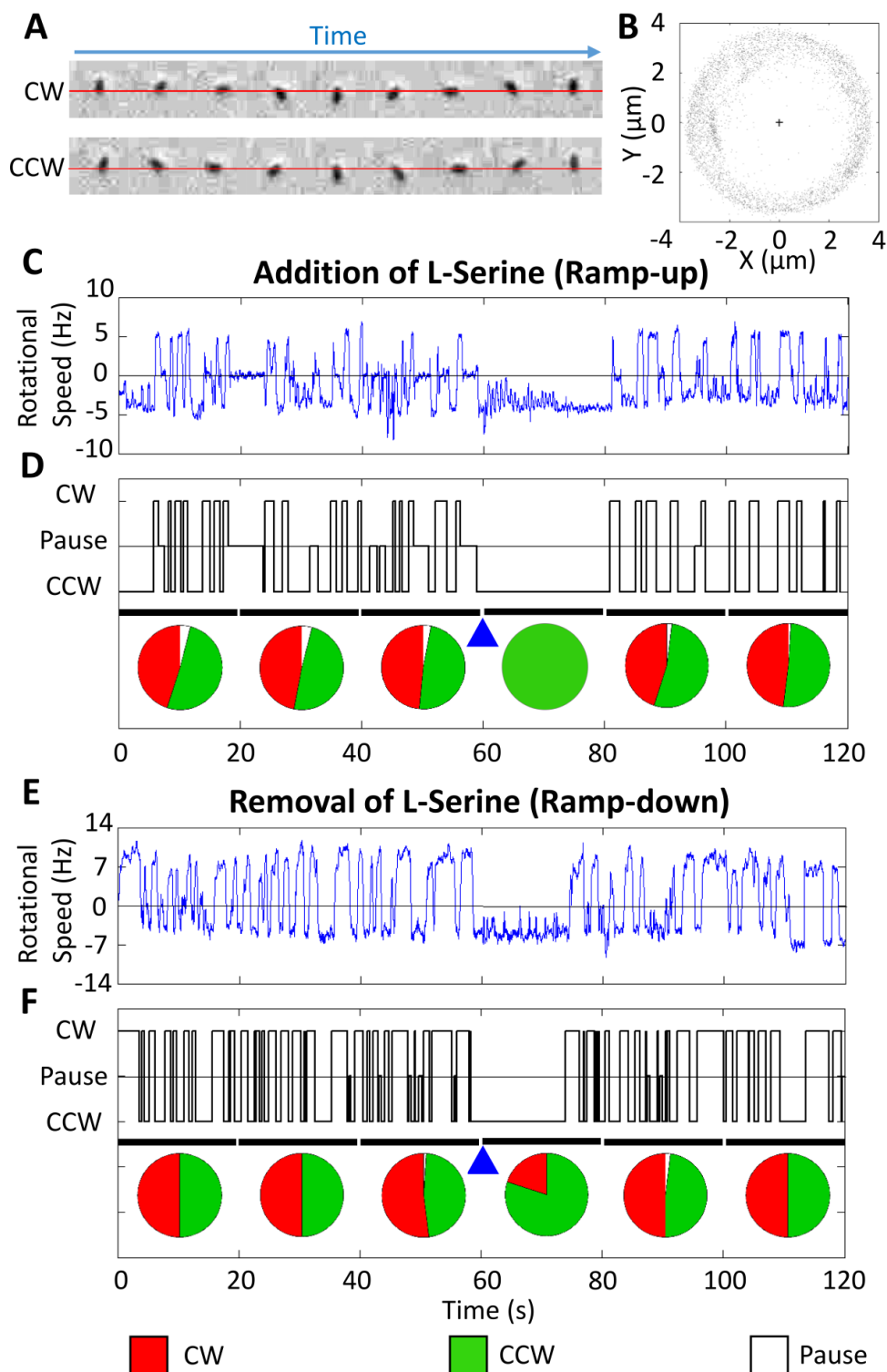


Figure 6.5 Quantitative analysis of the rotation profile of a tethered *P. aeruginosa* cell before (0-60 s) and after (60-120 s) addition of chemoattractant L-serine or control buffer M9. (a) Phase contrast time-lapsed images of a tethered cell rotating in

the CW and CCW direction (*top* and *bottom row* respectively). *Red lines* denote horizontal lines passing through the axis of rotation of the cell. (b) Scattering profile of the centroid positions of the tethered cell throughout the experiments at 40 fps for 120 s, with the *cross* indicating the bacterial rotation axis. (c) Instantaneous rotational speed of a tethered *P. aeruginosa* cell during a L-serine ramp-up experiment. (d) Rotational profile of the cell being classified into CW, CCW or pause phases during a L-serine ramp-up experiment. The *blue triangle* denotes the time in which L-serine is added. The pie charts show the percentage of CW (*red*), CCW (*green*) and pause (*white*) for every 20 seconds (thick *bars* at the bottom of the time series). (e) Instantaneous rotational speed of a tethered cell during ramp-down exposure in which M9 medium is flooded into the cell chamber. (f) Rotational profile of the cell being classified into CW, CCW or pause phases during the ramp-down experiments. The *blue triangle* denotes the time in which the chemoattractant was removed.

The adaptation time exhibited by cells during ramp up and ramp down signals was extracted from moving window analysis of the rotational profiles earlier shown in Fig. 6.5 (c,e). To calculate the adaptation time for bacteria, a 20s moving window was applied; the proportion of time cells spent in the CW or CCW phase was calculated for within a 20s time window and this time window was shifted by a time step of 0.025seconds. In order to quantify the adaptation response, the CW and CCW bias response was weighted as 1.0 and -1.0, respectively. For example, a CW bias of 1.0 indicates that cells exhibit rotation in only the CW direction, within the time window. Conversely, a -1.0 bias response indicates that cell rotation is entirely

biased to the *CCW* direction. The moving window analysis was applied to data obtained from both ramp-up and ramp-down exposure experiments. Results correlating to the ramp response of cells are plotted in Fig. 6.6 (a,b). In both scenarios, cells exhibit an immediate bias in rotation (in either the *CW* or *CCW* direction) upon the enrichment or removal of *L*- Serine within their microenvironment. This result is uniform, regardless of the rotation direction that the cell was moving in when a change in its nutrient landscape was sensed. This can be seen in the symmetry of adaptation responses for *CW* and *CCW* rotational bias, during ramp up and ramp down chemoattractant exposure (Fig. 6.6(a-d)). The adaptation time in response to ramp up or ramp down of *L*-serine was calculated by first plotting the rotation bias against the time lapsed during chemotaxis experiments. Fig 6.6(a, b) show the decay in *CW* rotation bias to pre-stimulus states, after an individual *P. Aeruginosa* cell had adapted to either a ramp up or ramp down in Chemoattractant concentration. This adaptation decay is fitted to an exponential curve denoted by $|F| = |F_0|e^{-\frac{t}{\tau}}$. (Segall et al., 1986) F and F_0 are the *CW* (or *CCW*) bias and maximum magnitude of *CW* (or *CCW*) bias attained respectively. t denotes chemotaxis assay time and τ denotes the adaptation time.

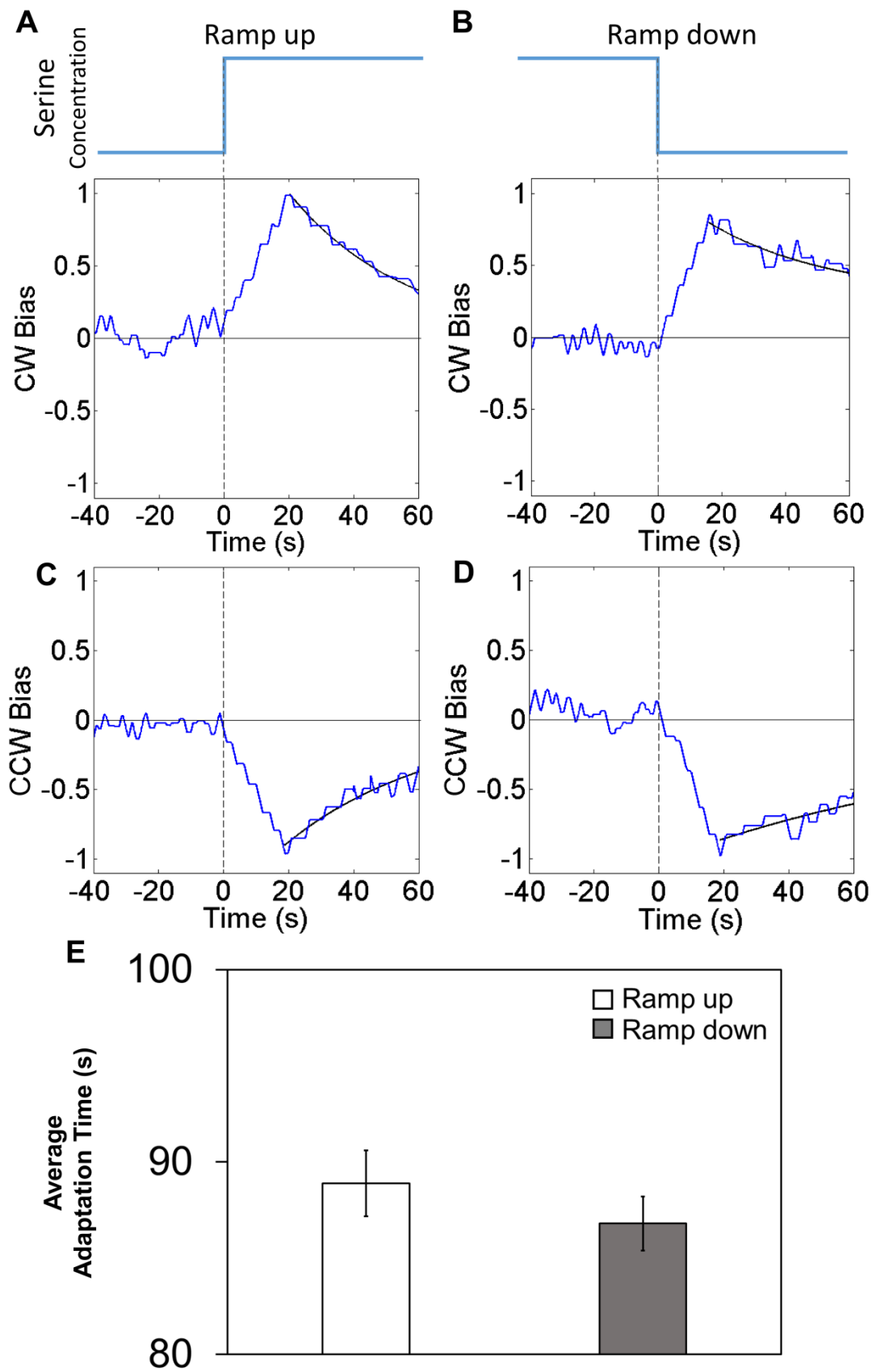


Figure 6.6 Moving time window analysis of the rotational behavior of *P. Aeruginosa* during a (a,c) ramp up and (b,d) ramp down of chemoattractant concentrations within their surroundings. (e) Using the adaptation profile shown in (a-d), the adaptation time for both scenarios was determined for a population of 50 cells.

Based on a population of 50 cells, the adaptation time exhibited by cells experiencing an enrichment or depletion of nutrient landscape was obtained and is summarized in Fig. 6.6(e). The findings indicate that there is no significant difference between the average adaptation times for cells exposed to either a ramp-up or a ramp-down L-serine signal (Student's t-test, $p = 0.3368$). This behavior is markedly different from previous reports on the model bacteria, *E.coli*. Firstly, previous reports found that *E.coli* sense a ramp up and ramp down in chemoattractant concentrations differently, sensing ramp down stimulation much quicker than ramp up stimulation (Min et al., 2012; Springer, Goy, & Adler, 1979). Based on the findings here, *P. Aeruginosa*, did not exhibit such asymmetry in adaptation times. However, similar to previous reports on adaptation (Endres & Wingreen, 2006; H. Park et al., 2010; Springer et al., 1979), it was found that *P. Aeruginosa* exhibited adaptation gradually, regardless of the abrupt change in nutrient landscapes. What occurs differently in *P. Aeruginosa* as compared to *E. coli*, during the process of adaptation? What is now known from this study is that chemotactic adaptation does not occur uniformly across different bacteria species. What is however, not known, is the mechanisms that result in the differences in the adaptation kinetics that are observed on a whole-cell level. Further studies on the level of individual flagellar

motors could produce interesting findings, linking the conformational state of individual motors to swimming behavior exhibited on a whole cell level.

6.5 Summary

In summary, the present results demonstrate a novel chemotactic microfluidic assay which is capable of delivering a rapid chemoattractant concentration ramp with no perturbation effects to *P. Aeruginosa* flagella rotation. The ability to deliver chemoattractant concentrations rapidly while not exposing cells to perturbations caused by flow shear is a significant advantage over current microfluidic platforms. Current microfluidic platforms achieve rapid deliver of chemoeffectors but do so at the expense of inducing flow shear (Min et al., 2012), which has been shown to curtail chemotactic responses in bacteria (Rusconi et al., 2014). As flow shear greatly influences cell migrational trajectories, microfluidic assays should be designed to account for flow shear effects especially when studying the chemotactic response of free swimming or tethered cells. Hithero, microfluidic assays to dynamically study and elicit evolving cell behavior in low shear environments are limited, especially for cells that exhibit chemotactic adaptation on the order of several seconds. Here, using the stagnation flow platform, *P. Aeruginosa* was shown, within seconds after *L*-Serine exposure, to adapt back to their pre-stimulus behaviour. A slower ramp delivery of *L*-Serine concentration would have partially convoluted the dynamic chemotactic response and the kinetics of adaptation thereafter. On the basis of results from chemotactic experiments, *P. Aeruginosa* cells were found to adapt to ramp-up and ramp-down stimuli within 88.9s and 86.8s, respectively. Comparing the adaptation kinetics to that reported for *E.coli*, *P. Aeruginosa* cells exhibit significantly longer

adaptation durations. Additionally, *P. Aeruginosa* cells do not portray the ‘overshoot’ or ‘response asymmetry’ behavior that has been previously measured in *E.coli* (Clausznitzer et al., 2010; Min et al., 2012). Neither of these characteristics were present in the single cell or population level chemotactic responses that were measured in this study. What is now known is that chemotactic adaptation and its associated characteristics are dependent on the flagella motor apparatus and chemosensory network. Further investigations involving the adaptation changes in molecular motors within the *P. Aeruginosa* cell would shed more light on how proteins within the chemosensory network influence changes in externalized flagellum movement. This precise microfluidic platform could be used to extract more information for constructing a biophysical model of the cell’s chemotactic responses and adaptation, bringing us closer to developing and controlling intelligent artificial molecular machines.

7 Conclusion and Future Studies

7.1 Conclusion and contributions of this study

Following the objectives of the present work, extensive work was done to study the use of stagnation flows to hydrodynamically confine and control concentration gradients. Using experimental, analytical and numerical approaches, steady-state and transient characteristics of concentration gradient development across stagnation flows were discovered. Good agreement amongst the experimental, analytical and numerical results was obtained. An in-depth understanding of the physical parameters influencing concentration gradient generation was demonstrated. Additionally, the MCS device with associated stagnation flow was applied to study the dynamic chemotactic behavior of *P. Aeruginosa*, without flow shear effects. The major contributions made by this research can thus be summarized as follows:

1. **Thorough steady-state and transient studies of concentration gradient development across stagnation flow are conducted, resulting in the derivation of an analytical model that identifies the characteristic length and time scales.** A modified cross-slot (MCS) device with a central stagnation flow chamber was designed, fabricated and tested through a parametric study of concentration gradient development in stagnation flow. The effects of MCS channel geometry and flow rate, on stagnation flow characteristics were studied. In particular, channel geometry and flow rate were both found to influence the flow strain rate of extensional stagnation flow within the central flow chamber. These parametric effects on the flow strain rate can be described using a dimensionless Péclet number and appropriate length and time scales. Steady-state concentration gradient length is

inversely related to the Peclet number increased, thus showing that the gradient lengths could be hydrodynamically or geometrically controlled. An analytical solution was derived to describe the steady-state concentration gradient formed across the stagnation flow. An appropriate time scale was selected to characterize the transient development of concentration gradients across the stagnation flow. The experimental results were found to be in good agreement to the analytical results for steady-state concentration gradients formed. The analytically derived time scale for concentration gradient development within the MCS device was also shown to accurately predict the transient development of concentration gradients. While there have been several analytical models that describe stagnation flow characteristics (Hudson et al., 2004; J. S. Lee et al., 2007), models that describe the convective-diffusive process of concentration species across such flows have not been developed. The identification of appropriate scaling factors and the dimensionless Péclet number in the derived model is useful in several ways:

- Allows direct evaluation of the concentration gradient length formed with respect to the Péclet number- a value that is not directly discerned from numerical simulations
- Provides an accurate time scale for convection-diffusion processes across stagnation flow.
- Can be extended to describe the temperature distributions across stagnation flows since heat transfer is analogous to mass transport.

2. **Binary and combinational concentration gradients are shown to be hydrodynamically confined within the velocity wells that form as a consequence of stagnation flow.** Binary and combinational concentration gradients

can be hydrodynamically focused across stagnation flow. By feeding streams of concentration source- sink pairs into the stagnation flow chamber, concentration gradients of a single chemical species or a combination of chemical species can be tuned across the stagnation flow. Most notably, concentration gradients are directly tunable by the steepness of velocity wells that surround the stagnation point. In particular, the MCS device demonstrated dynamic establishment of these concentration gradients while maintaining low in-chamber shear stresses. Furthermore, such a gradient generation scheme can be used to quickly stabilize rapidly decaying gradients of small molecules while maintaining low in-chamber shear stresses, surpassing the saturation limitations of gel-based low shear gradient generators.

3. **Hydrodynamic positioning of velocity wells are demonstrated to move binary and combinational concentration gradients in a fast and controllable manner.** The effect of flow rate ratio was characterized in relation to stagnation point positioning within the MCS flow chamber. Variations in the flow rate ratio were found to directly position the stagnation point and move the associated velocity wells. These moving velocity wells were demonstrated to entrain combinational and overlapping concentration gradients, allowing a direct method to hydrodynamically move combinational concentrations on-demand. Current concentration gradient generators endeavour to achieve a reduction in shear flow through the addition of shear relief structures like expansion chambers, membranes or gels, these structures in turn hamper the speed at which concentration gradients can be tuned or moved. The use of velocity wells in stagnation flow addresses the mass transport problem of quickly moving binary and combinational concentration

gradients, while inducing low shear flow. The MCS device was shown to achieve the hydrodynamic positioning of concentration gradients in a two-dimensional landscape, while suppressing flow shear effects.

4. **The MCS device demonstrates the novel use of stagnation flow to rapidly deliver temporal concentration ramps while eliciting dynamic cell responses that are unperturbed by flow shear.** The chemotactic response of tethered *P. Aeruginosa* cells was studied within the MCS stagnation flow chamber. At high flow rates of 220nl s^{-1} , corresponding to a flow shear of 2.45mPa , tethered *P. Aeruginosa* cells stopped rotating and aligned themselves along the flow direction. At optimized flow rates less than 220nl s^{-1} , a rapid ramp ($t \sim 3\text{s}$) in chemoattractant concentration was introduced, via stagnation flow, to unperturbed *P. Aeruginosa* cells located near the stagnation point. The precise temporal ramp-up and ramp-down of chemoattractant concentrations, allowed tethered cell rotations to be studied with high temporal resolutions. The rotational bias and subsequent adaptation of cells upon exposure to a ramp-up in *L*-Serine concentration was quantified to be $88.9 \pm 17.3\text{s}$. The adaptation time upon exposure to a ramp-down in *L*-serine concentration was also discernible at $86.8 \pm 12.8\text{s}$. The chemotactic adaptation of *P. Aeruginosa* was found to differ from that reported for the model organism, *E.coli* (Min et al., 2012). Chemotactic adaptation in *E.coli* has been shown to exhibit two characteristic responses- an overshoot response after adaptation and asymmetric responses to ramp-up or ramp-down stimuli. *P. Aeruginosa* did not exhibit any of these characteristics. Specifically, *P. Aeruginosa* responded in a significantly similar manner to ramp-up and ramp-down stimuli and did not exhibit any increase in rotational bias as compared to pre-stimulus states. Using this microfluidic assay, the

chemotactic kinetics of *P. Aeruginosa* cells, unperturbed by flow shear, were found to be vastly dissimilar to previous studies on the model bacteria, *E.coli*. The results presented here highlight the complex nature of bacteria motility and the need for more information to construct biophysical models that accurately predict bacteria behaviour. By leveraging on precise microfluidic assays, more information can be gleamed about the manner these cells move, bringing us closer to developing and controlling artificial molecular machines.

7.2 Recommendations for future studies

Based on the results presented in this study, some recommendations are made for future research.

1. Further to the experimental and analytical work presented in Chapter 4, stagnation flow experiments can be conducted with respect to changes in the stagnation chamber height. Current experimental results show that concentration gradient generation across the stagnation flow can be controlled by hydrodynamic flow or variations in diffusion channel widths. Further dynamic control of the concentration gradients can also be achieved if the geometry of the stagnation chamber could be dynamically controlled. It is known from the present experimental results that a reduction in the diffusion channel width decreases the flow strain rate by way of an increase in hydraulic resistance. Dynamic variations in the hydraulic resistance could, theoretically be achieved using a flexible membrane roof for the stagnation chamber. Similar to a membrane valve, addition of a pressure line above the membrane roof would allow the height of the stagnation chamber to be

dynamically controlled. It would be meaningful to find out if a simplified analytical relationship between the stagnation chamber geometry and the concentration gradient length could be derived by the introduction of a mathematically defined shape factor. In addition, more studies can be done to provide a better understanding of how different combinations of inlet flow rates (Q1 to Q4) could influence the localization and development of stagnation flows within the main chamber.

2. In Chapter 6, population and single cell level analysis of *P. Aeruginosa* chemotactic behavior was successfully elucidated from the MCS device platform. However, more in depth and complex studies can be designed using the MCS device. The MCS device has mainly four delivery channels (*i.e.* concentration poles) feeding concentration species across the stagnation flow. In this respect, dynamic chemotaxis assays can be performed by exposing micro-organisms to competing chemoeffector landscapes. Currently, it is not possible to recapitulate overlapping concentration gradients in a dynamic manner. Most overlapping or combinational concentration gradients recreated in microfluidic devices have been statically derived across hydrogels , and are thus, not dynamically configurable. Stagnation flow confined combinational concentration gradients, together with dynamic capture of cell behavior, would allow new insights to be gleamed about herarchical decision making processes occurring during cell chemotaxis and their underlying kinetics. Moreover, the number of concentration poles within this MCS device is not limited to four. Addition of concentration pairs around a symmetrical stagnation flow chamber could also be achieved if more concentration species are to be studied.

Appendix A. FOTS Deposition Protocol

A self-assembled monolayer of Trichloro(1H,1H,2H,2H-perfluorooctyl)silane (FOTS) is deposited on silicon wafer molds to ensure clean release of casted PDMS devices. The deposition protocol requires use of a vacuum oven (Fisher Scientific Isotemp Model 281A), a glass petri dish and a fumehood. Due to the flammable nature of FOTS, it should not be heated under an open flame. In addition, because its vapour is colourless and carcinogenic, the chemical should be handled in an operating fumehood.

The protocol used during deposition is as follows:

- 1) Place wafers into the vacuum oven trays
- 2) Aliquot 60 μ l of FOTS into a glass petri dish
- 3) Tune the oven settings to heat the chamber at 80°C
- 4) Set the chamber vacuum level to 20”Hg (\sim 40kPa)
- 5) Retrieve wafers after a deposition duration of 12 hours

Appendix B. Pressure Pump Design

To ensure stable flow during microfluidic experiments, a customized pressure system was developed. This system was used to connect to an air pressure source and was assembled using the following components:

- 1) 4 Pressure Regulators (SMC)
- 2) 4 Pressure Sensors (SMC)
- 3) 4 Digital Pressure Display (SMC)
- 4) 4 Solenoid Valves (Lee Valves)
- 5) 1 Valve Manifold (Lee Valves)
- 6) 1 DAQ Controller (National Instruments)
- 7) 1 DC to AC converter (Digikey)

The components were used to control pressure- driven flow within the MCS device.

The control scheme for the pressure pump is shown in Fig. B1.

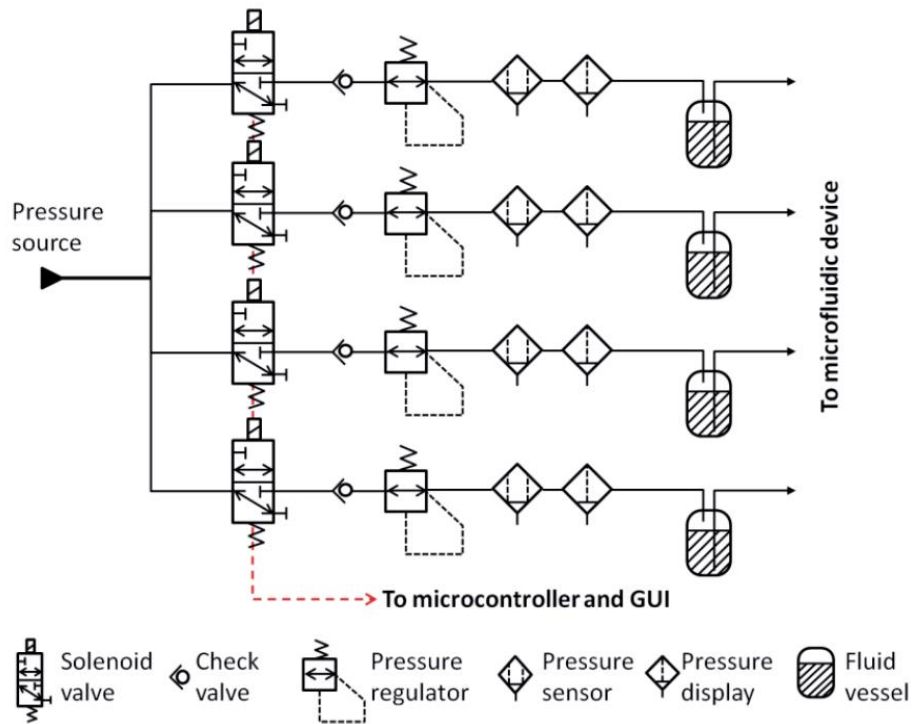


Fig. B1 Control scheme for the pressure pump system.

The components were integrated into a pump system as shown in Fig. B2.

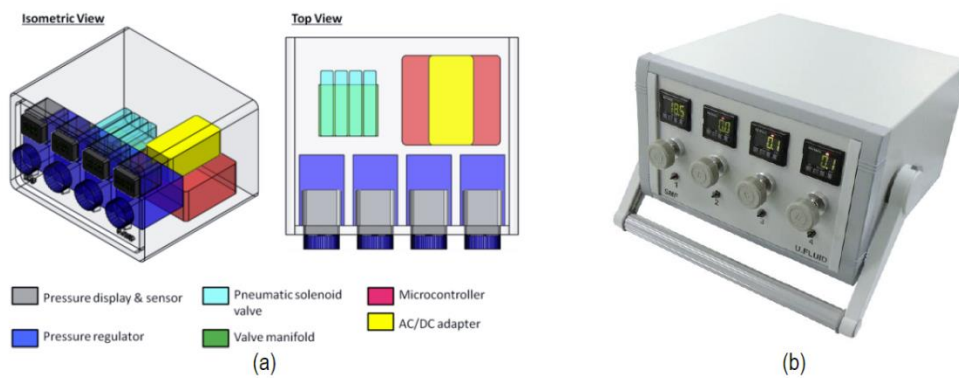


Fig. B2 (a) Placement of control components within the pump. (b) Photograph of assembled pressure pump system.

In order to determine the stability of the flow driven by the pump, a pump calibration test was performed by measuring the flow eluted from the fluid vessel (a 100ml glass bottle reservoir, with GL45 tube fittings). The flow was measured using a flow meter (Mitos flow rate sensor, 30-1000 $\mu\text{L min}^{-1}$). The flow rate performance of the pump is presented in Fig. B3. Based on calibration experiments, the flow rate eluted from the pressure pump was stable at $\pm 5\%$ of the full scale flow rate range of 900 $\mu\text{L min}^{-1}$.

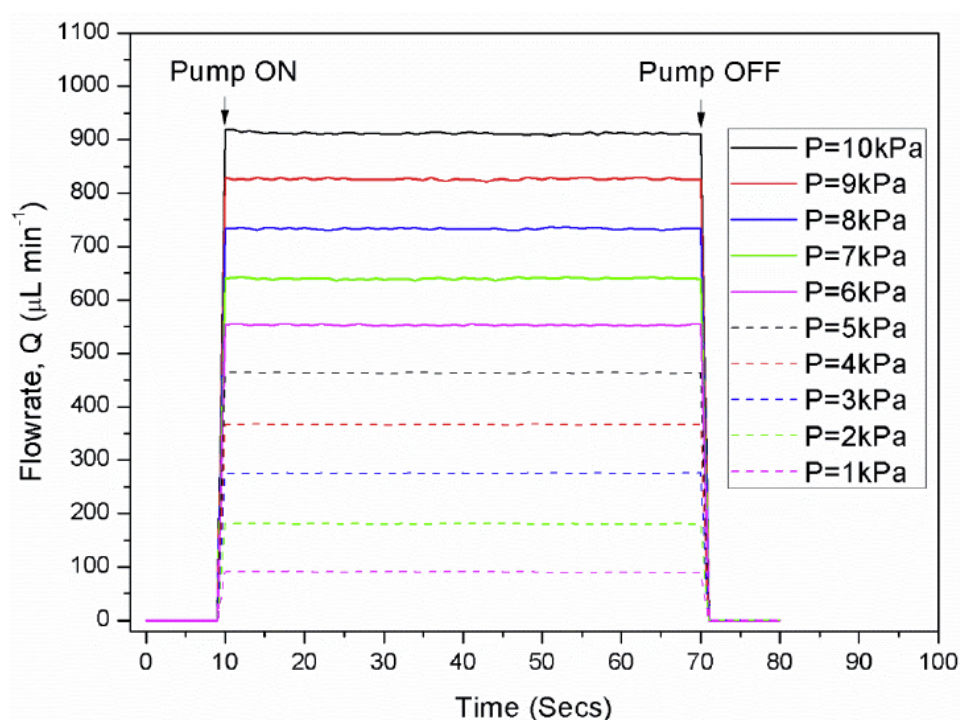


Fig. B3 Plot showing the stability of flow controlled by the pressure pump.

Appendix C. Experimental uncertainty analysis

In this thesis, the uncertainty during PIV experiments was due to the translocation of PIV particles through the thickness of the device. In order to account for this experimental error, the flow velocities and also derived flow strain rates, were obtained by sampling 100 sets of image pairs. The uncertainty involved in experimental data collection is calculated by first deriving the standard deviation, σ for $n=100$ repeated readings such that:

$$\sigma = \sqrt{\frac{\sum (x_i - \bar{x})^2}{(n - 1)}}$$

where the sample mean $\bar{x} = \sum x_i / n$.

The random uncertainty of the experiment, U_e , is subsequently evaluated by the standard deviation of the mean:

$$U_e = \sigma / \sqrt{n}$$

In this thesis, experimental uncertainty was quantified as the standard deviation, and is shown as the error-bars in all the experimental data plotted.

Appendix D. *Péclet* number calculations for flows

Mass transport across the stagnation flow was scaled using a dimensionless *Péclet* number, $Pé$, such that $Pé = \frac{UL}{D} = \frac{\dot{\epsilon}d^2}{D}$. An estimate of the characteristic velocity is defined here as $U = |v_{y=d}| = \dot{\epsilon}d$. d is defined as the characteristic length of the MCS device. D is the diffusion coefficient of the fluorescein sodium in water, $D=5 \times 10^{-10} \text{ m}^2 \text{ s}^{-1}$. In order to determine the correlation between the $Pé$ number and the concentration gradient formed, the flow strain rates at various flow rates were first experimentally measured. These strain rates were subsequently used to calculate the $Pé$ number which was correlated to the gradient length and plotted Fig. 4.4. The flow strain rates corresponding to the calculated $Pé$ and concentration gradient lengths are summarized in Tables B1, B2 and B3.

Table B 1 Flow strain rates corresponding to the calculated $Pé$ and concentration gradient lengths for $w=20\mu\text{m}$ devices.

Inlet flow rate, Q (nl s ⁻¹)	Strain rate (s ⁻¹)	$Pé$	$\frac{1}{\sqrt{Pé}}$	Concentration gradient length (μm)	Gradient length error (μm)
16.421	0.21676	209.2058	0.06914	170.8335	6.39208
48.359	0.63834	616.1004	0.04029	103.2261	10.61939
64.425	0.85041	820.7834	0.0349	81.7738	3.69152
80.4145	1.06147	1024.492	0.03124	63.23207	10.49244
103.43	1.36528	1317.713	0.02755	54.02387	14.43242
121.3817	1.60224	1546.42	0.02543	50.30353	7.88382
143.8133	1.89834	1832.201	0.02336	48.63687	20.20538
191.3276	2.52552	2437.54	0.02025	45.29767	11.01084
249.545	3.29399	3179.238	0.01774	43.64293	11.59862
300	3.96	3822.042	0.01618	40.64293	11.59862

Table B 2 Flow strain rates corresponding to the calculated $Pé$ and concentration gradient lengths for $w=30\mu\text{m}$ devices.

Inlet flow rate, Q (nl s ⁻¹)	Strain rate (s ⁻¹)	$Pé$	$\frac{1}{\sqrt{Pé}}$	Concentration gradient length (μm)	Gradient length error (μm)
20.5833	0.40755	393.3511	0.05042	111.5178	8.04812
44	0.8712	840.8491	0.03449	75.52197	14.39471
66.0833	1.30845	1262.866	0.02814	61.756	17.04829
99.25	1.96515	1896.688	0.02296	49.69907	9.21922
117.3333	2.3232	2242.264	0.02112	43.3334	10.02054
148.083	2.93204	2829.897	0.0188	35.71427	11.81139
176.5	3.4947	3372.952	0.01722	35.5556	10.0206
218.5	4.3263	4175.58	0.01548	32.73807	13.63855
257.25	5.09355	4916.101	0.01426	32.8888	13.8778
300	5.94	5733.062	0.01321	30.8888	13.8778

Table B 3 Flow strain rates corresponding to the calculated $Pé$ and concentration gradient lengths for $w=50\mu\text{m}$ devices.

Inlet flow rate, Q (nl s ⁻¹)	Strain rate (s ⁻¹)	$Pé$	$\frac{1}{\sqrt{Pé}}$	Concentration gradient length (μm)	Gradient length error (μm)
15.3333	0.506	488.3709	0.04525	96.5774	10.98078
30.5833	1.00925	974.0887	0.03204	66.27893	6.82043
45.08333	1.48775	1435.92	0.02639	49.62913	3.39492
79.91667	2.63725	2545.374	0.01982	40.59267	3.15306
105.8333	3.4925	3370.827	0.01722	39.25933	1.28287
126.25	4.16625	4021.106	0.01577	32.07413	3.39447
156.75	5.17275	4992.542	0.01415	28.3702	4.6262
178.4167	5.88775	5682.634	0.01327	25.296	10.50189
233.75	7.71375	7445.018	0.01159	21.5554	10.18373
257.25	8.48925	8193.501	0.01105	19.14787	1.28264
300	9.9	9555.104	0.01023	20.14787	1.28264

Appendix E. Coefficient of variation analysis for steady state time within cell observation window

Within the 100 μm square observation window, chamber concentrations (visualized through fluorescein dye) were measured during ramp up and ramp down concentration profiles. The temporal concentration profiles across five location around the periphery of the observation window, were analyzed and plotted. Amongst the five concentration profiles, the coefficient of variation across time was calculated as:

$$c_v(t) = \frac{\sigma_{1-5}(x,y,t)}{\mu_{1-5}(x,y,t)} \quad [\text{C1}]$$

where $\mu_{1-5}(x,y,t)$ denotes the concentration mean across the five locations and $\sigma_{1-5}(x,y,t)$ denotes the concentration variation across the five locations.

Fig. C1 plots the coefficient of variation for (a) ramp up and (b) ramp down concentration profiles. In both cases, the maximum c_v occurred near the onset of concentration ramping. The maximum concentration variation for ramp up and ramp down concentration profiles was calculated to be 3.7% and 3%. This result highlights that within the 100 μm observation window, cells experience relatively uniform concentration levels, during the duration of the chemotaxis assay.

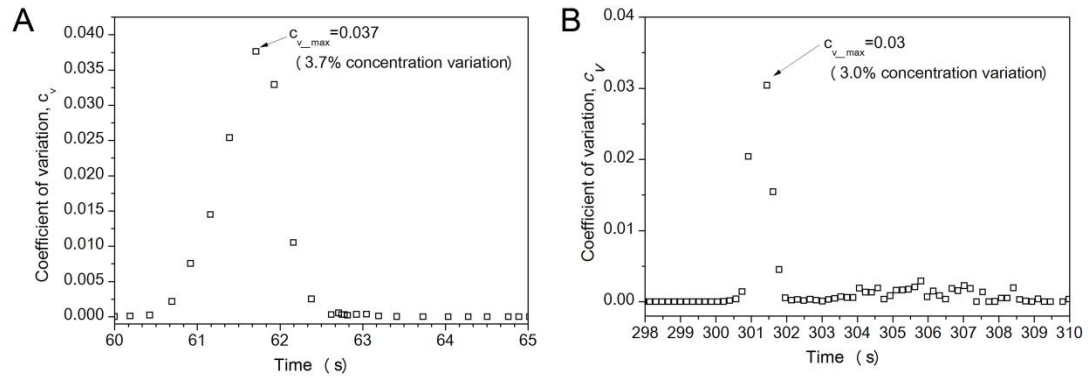


Fig. C1 | Analysis of temporal concentration variation across five locations within the 100 μ m by 100 μ m central observation window.

References

- Abhyankar, V. V., Toepke, M. W., Cortesio, C. L., Lokuta, M. A., Huttenlocher, A., & Beebe, D. J. (2008). A platform for assessing chemotactic migration within a spatiotemporally defined 3D microenvironment. *Lab on a Chip*, 8(9), 1507-1515.
- Ahmed, T., Shimizu, T. S., & Stocker, R. (2010). Bacterial Chemotaxis in Linear and Nonlinear Steady Microfluidic Gradients. *Nano Letters*, 10(9), 3379-3385.
- Ahmed, T., Shimizu, T. S., & Stocker, R. (2010). Microfluidics for bacterial chemotaxis. *Integrative Biology*, 2(11-12), 604-629.
- Archimedes. (2009). *The Works of Archimedes*: Cambridge University Press.
- Arratia, P. E., Thomas, C. C., Diorio, J., & Gollub, J. P. (2006). Elastic instabilities of polymer solutions in cross-channel flow. *Physical Review Letters*, 96, 144502.
- Astarita, G. (1979). Objective and generally applicable criteria for flow classification. *Journal of Non-Newtonian Fluid Mechanics*, 6(1), 69-76.
- Atencia, J., Cooksey, G. A., & Locascio, L. E. (2012). A robust diffusion-based gradient generator for dynamic cell assays. *Lab on a Chip*, 12(2), 309-316.
- Atencia, J., Morrow, J., & Locascio, L. E. (2009). The microfluidic palette: A diffusive gradient generator with spatio-temporal control. *Lab on a Chip*, 9, 2707 - 2714.
- Bacabac, R. G., Smit, T. H., Cowin, S. C., Van Loon, J. J., Nieuwstadt, F. T., Heethaar, R., & Klein-Nulend, J. (2005). Dynamic shear stress in parallel-plate flow chambers. *Journal of Biomechanics*, 38(1), 159-167.
- Bang, H., Lim, S. H., Lee, Y. K., Chung, S., Chung, C., Han, D.-C., & Chang, J. K. (2004). Serial dilution microchip for cytotoxicity test. *Journal of Micromechanics and Microengineering*, 14, 1165 - 1170.
- Bedingfield, C. H., & Drew, T. B. (1950). Analogy between Heat Transfer and Mass Transfer. *Industrial & Engineering Chemistry*, 42(6), 1164-1173.
- Berg, H. C. (2004). *E. coli in Motion*: Springer-Verlag New York.
- Berthier, E., Surfus, J., Verbsky, J., Huttenlocher, A., & Beebe, D. (2010). An arrayed high-content chemotaxis assay for patient diagnosis. *Integrative Biology*, 2(11-12), 630-638.
- Beta, C., & Bodenschatz, E. (2011). Microfluidic tools for quantitative studies of eukaryotic chemotaxis. *European Journal of Cell Biology*, 90(10), 811-816.
- Bhattacharjee, N., Li, N., Keenan, T. M., & Folch, A. (2010). A Neuron-Benign Microfluidic Gradient Generator for Studying the Response of Mammalian Neurons towards Axon Guidance Factors. *Integr. Biol. (Camb.)*, 2(0), 669-679.
- Block, S. M., Segall, J. E., & Berg, H. C. (1982). Impulse responses in bacterial chemotaxis. *Cell*, 31(1), 215-226.
- Boy, D. A., Gibou, F., & Pennathur, S. (2008). Simulation tools for lab on a chip research: advantages, challenges, and thoughts for the future. *Lab on a Chip*, 8(9), 1424-1431.

- Boyden, S. (1962). Chemotactic effect of mixtures of antibody and antigen on polymorphonuclear leukocytes. *Journal of Experimental Medicine*, 115(3), 453-466.
- Brenner, S. (1974). The genetics of *Caenorhabditis Elegans*. *Genetics*, 77(1), 71-94.
- Brett, M.-E., DeFlorio, R., Stone, D. E., & Eddington, D. T. (2012). A microfluidic device that forms and redirects pheromone gradients to study chemotropism in yeast. *Lab on a Chip*, 12(17), 3127-3134.
- Chau, L. T., Rolfe, B. E., & Cooper-White, J. J. (2011). A microdevice for the creation of patent, three-dimensional endothelial cell-based microcirculatory networks. *Biomicrofluidics*, 5(3), 034115-034114.
- Chen, C.-Y., Wo, A. M., & Jong, D.-S. (2012). A microfluidic concentration generator for dose-response assays on ion channel pharmacology. *Lab on a Chip*, 12(4), 794-801.
- Cheng, J.-Y., Yen, M.-H., Kuo, C.-T., & Young, T.-H. (2008). A transparent cell-culture microchamber with a variably controlled concentration gradient generator and flow field rectifier. *Biomicrofluidics*, 2, 1 - 12.
- Cheng, S.-Y., Heilman, S., Wasserman, M., Archer, S., Shuler, M. L., & Wu, M. (2007). A hydrogel-based microfluidic device for the studies of directed cell migration. *Lab on a Chip*, 7(6), 763-769.
- Chung, B. G., & Choo, J. (2010). Microfluidic gradient platforms for controlling cellular behavior. *Electrophoresis*, 3014-3027.
- Chung, B. G., Flanagan, L. A., Rhee, S. W., Schwartz, P. H., Lee, A. P., Monuki, E. S., & Jeon, N. L. (2005). Human neural stem cell growth and differentiation in a gradient-generating microfluidic device. *Lab on a Chip*, 5(4), 401-406.
- Chung, K., Zhan, M., Srinivasan, J., Sternberg, P. W., Gong, E., Schroeder, F. C., & Lu, H. (2011). Microfluidic chamber arrays for whole-organism behavior-based chemical screening. *Lab on a Chip*, 11(21), 3689-3697.
- Cimetta, E., Cannizzaro, C., James, R., Biechele, T., Moon, R. T., Elvassore, N., & Vunjak-Novakovic, G. (2010). Microfluidic device generating stable concentration gradients for long term cell culture: application to Wnt3a regulation of [small beta]-catenin signaling. *Lab on a Chip*, 10(23), 3277-3283.
- Clausznitz, D., Oleksiuk, O., Løvdok, L., Sourjik, V., & Endres, R. G. (2010). Chemotactic Response and Adaptation Dynamics in *Escherichia coli*. *PLoS Computer Biology*, 6(5), e1000784.
- COMSOL. (2012). *COMSOL Multiphysics User Guide (Version 4.3a)*: COMSOL.
- Connelly, J. T., Gautrot, J. E., Trappmann, B., Tan, D. W.-M., Donati, G., Huck, W. T. S., & Watt, F. M. (2010). Actin and serum response factor transduce physical cues from the microenvironment to regulate epidermal stem cell fate decisions. *Nature Cell Biology*, 12(7), 711-718.
- Crane, M. M., Chung, K., Stirman, J., & Lu, H. (2010). Microfluidics-enabled phenotyping, imaging, and screening of multicellular organisms. *Lab on a Chip*, 10(12), 1509-1517.
- Culbertson, C. T., Jacobson, S. C., & Michael Ramsey, J. (2002). Diffusion coefficient measurements in microfluidic devices. *Talanta*, 56(2), 365-373.

- Dai, W., Zheng, Y., Luo, K. Q., & Wu, H. (2010). A prototypic microfluidic platform generating stepwise concentration gradients for real-time study of cell apoptosis. *Biomicrofluidics*, 4, 0241011 - 02410114.
- Deen, W. M. (1998). *Analysis of transport phenomena*: Oxford University Press.
- Dertinger, S. K. W., Chiu, D. T., Jeon, N. L., & Whitesides, G. M. (2001). Generation of gradients having complex shapes using microfluidic networks. *Analytical Chemistry*, 73, 1240-1246.
- Deschamps, J., Kantsler, V., Segre, E., & Steinberg, V. (2009). Dynamics of a vesicle in general flow. *Proceedings of the National Academy of Science of the United States of America*, 106(28), 11444-11447.
- Dirk, A. R., & Cornelia, B. I. (2011). High-content behavioral analysis of *Caenorhabditis elegans* in precise spatiotemporal chemical environments. *Nature Methods*, 8(7), 599-605.
- Dishinger, J. F., Reid, K. R., & Kennedy, R. T. (2009). Quantitative Monitoring of Insulin Secretion from Single Islets of Langerhans in Parallel on a Microfluidic Chip. *Analytical Chemistry*, 81(8), 3119-3127.
- Doyle, T. B., Hawkins, A. C., & McCarter, L. L. (2004). The Complex Flagellar Torque Generator of *Pseudomonas aeruginosa*. *Journal of Bacteriology*, 186(19), 6341-6350.
- Du, Y., Shim, J., Vidula, M., Hancock, M. J., Lo, E., Chung, B. G., & Khademhosseini, A. (2009). Rapid generation of spatially and temporally controllable long-range concentration gradients in a microfluidic device. *Lab on a Chip*, 9(6), 761-767.
- Dupin, I., Dahan, M., & Studer, V. (2013). Investigating Axonal Guidance with Microdevice-Based Approaches. *J. Neurosci.*, 33(45), 17647-17655.
- Dylla-Spears, R., Townsend, J. E., Jen-Jacobson, L., Sohn, L. L., & Muller, S. J. (2010). Single-molecule sequence detection via microfluidic planar extensional flow at a stagnation point. *Lab on a Chip*, 10(12), 1543-1549.
- Einstein, A. (1905). The theory of the brownian movement. *Annalen der Physik*, 17, 549.
- Eisenbach, M. (2004). *Chemotaxis*: Imperial College Press.
- El-Ali, J., Sorger, P. K., & Jensen, K. F. (2006). Cells on chips. *Nature*, 442(7101), 403-411.
- Endres, R. G., & Wingreen, N. S. (2006). Precise adaptation in bacterial chemotaxis through "assistance neighborhoods". *Proceedings of the National Academy of Sciences of the United States of America*, 103(35), 13040-13044.
- Englert, D. L., Manson, M. D., & Jayaraman, A. (2009). Flow-Based Microfluidic Device for Quantifying Bacterial Chemotaxis in Stable, Competing Gradients. *Applied and Environmental Microbiology*, 75(13), 4557-4564.
- Englert, D. L., Manson, M. D., & Jayaraman, A. (2010). Investigation of bacterial chemotaxis in flow-based microfluidic devices. *Nature Protocols*, 5(5), 864-872.
- Frank, T., & Tay, S. (2013). Flow-switching allows independently programmable, extremely stable, high-throughput diffusion-based gradients. *Lab on a Chip*, 13(7), 1273 - 1281.
- Gabrielson, N. P., Desai, A. V., Mahadik, B., Hofmann, M.-C., Kenis, P. J. A., & Harley, B. A. C. (2013). Cell-Laden Hydrogels in Integrated Microfluidic Devices for Long-Term Cell Culture and Tubulogenesis Assays. *Small*, 9(18), 3076-3081.

- Gao, X., Zhang, X., Xu, H., Zhou, B., Wen, W., & Qin, J. (2014). Regulation of cell migration and osteogenic differentiation in mesenchymal stem cells under extremely low fluidic shear stress. *Biomicrofluidics*, 8(5), 052008.
- Gendron, P. O., Avaltroni, F., & Wilkinson, K. J. (2008). Diffusion Coefficients of Several Rhodamine Derivatives as Determined by Pulsed Field Gradient–Nuclear Magnetic Resonance and Fluorescence Correlation Spectroscopy. *Journal of Fluorescence*, 18(6), 1093-1101.
- Gomez-Sjoberg, R., Leyrat, A. A., Pirone, D. M., Chen, C. S., & Quake, S. R. (2007). Versatile, fully automated, microfluidic cell culture system. *Analytical Chemistry*, 79, 8557- 8563.
- Grossmann, G., Guo, W.-J., Ehrhardt, D. W., Frommer, W. B., Sit, R. V., Quake, S. R., & Meier, M. (2011). The RootChip: An Integrated Microfluidic Chip for Plant Science. *The Plant Cell Online*, 23(12), 4234-4240.
- Guilak, F., Cohen, D. M., Estes, B. T., Gimble, J. M., Liedtke, W., & Chen, C. S. (2009). Control of Stem Cell Fate by Physical Interactions with the Extracellular Matrix. *Cell Stem Cell*, 5(1), 17-26.
- Guo, F., French, J. B., Li, P., Zhao, H., Chan, C. Y., Fick, J. R., & Huang, T. J. (2013). Probing cell-cell communication with microfluidic devices. *Lab on a Chip*, 13(16), 3152-3162.
- Gupta, K., Kim, D. H., Ellison, D., Smith, C., Kundu, A., Tuan, J., & Levchenko, A. (2010). Lab-on-a-chip devices as an emerging platform for stem cell biology. *Lab on a Chip*, 10(16), 2019-2031.
- Hart, D.P. (2000). PIV error correction. *Experiments in Fluids*, 29(1), 13-22.
- Haessler, U., Kalinin, Y., Swartz, M., & Wu, M. (2009). An agarose-based microfluidic platform with a gradient buffer for 3D chemotaxis studies. *Biomedical Microdevices*, 11(4), 827-835.
- Haessler, U., Pisano, M., Wu, M., & Swartz, M. A. (2011). Dendritic cell chemotaxis in 3D under defined chemokine gradients reveals differential response to ligands CCL21 and CCL19. *Proceedings of the National Academy of Sciences of the United States of America*, 108(14), 5614-5619.
- Hamid, Z. A. A., Blencowe, A., Ozcelik, B., Palmer, J. A., Stevens, G. W., Abberton, K. M., & Qiao, G. G. (2010). Epoxy-amine synthesised hydrogel scaffolds for soft-tissue engineering. *Biomaterials*, 31(25), 6454-6467.
- Harting, J., Kunert, C., & Hyvaluoma, J. (2010). Lattice Boltzmann simulations in microfluidics: probing the no-slip boundary condition in hydrophobic, rough, and surface nanobubble laden microchannels. *Microfluidics and nanofluidics*, 8(1), 1-10.
- Haward, S. J. (2014). Synovial Fluid Response to Extensional Flow: Effects of Dilution and Intermolecular Interactions. *PLoS ONE*, 9(3), e92867.
- Haward, S. J., Jaishankar, A., Oliveira, M. S. N., Alves, M. A., & McKinley, G. H. (2013). Extensional flow of hyaluronic acid solutions in an optimized microfluidic cross-slot device. *Biomicrofluidics*, 7(4), 044108.
- Haward, S. J., & McKinley, G. H. (2013). Instabilities in stagnation flows of polymer solutions. *Physics of Fluids*, 25, 083104.
- Heo, Y. S., Cabrera, L. M., Bormann, C. L., Shah, C. T., Takayama, S., & Smith, G. D. (2010). Dynamic microfunnel culture enhances mouse embryo development and pregnancy rates. *Human Reproduction*, 25(3), 613-622.

- Hu, W., Berdugo, C., & Chalmers, J. J. (2011). The potential of hydrodynamic damage to animal cells of industrial relevance: current understanding. *Cytotechnology*, 63(5), 445-460.
- Huang, P.-H., Chan, C. Y., Li, P., Nama, N., Xie, Y., Wei, C.-H., & Huang, T. J. (2015). A spatiotemporally controllable chemical gradient generator via acoustically oscillating sharp-edge structures. *Lab on a Chip*, 15(16), 4166-4176.
- Hudson, S. D., Phelan, F. R., Handler, M. D., Cabral, J. T., Migler, K. B., & Amis, E. J. (2004a). Microfluidic analog of the four-roll mill. *Applied Physics Letters*, 85(2), 335-337.
- Hulme, S. E., Shevkoplyas, S. S., McGuigan, A. P., Apfeld, J., Fontana, W., & Whitesides, G. M. (2010). Lifespan-on-a-chip: microfluidic chambers for performing lifelong observation of *C. elegans*. *Lab on a Chip*, 10(5), 589-597.
- Hung, P. J., Lee, P. J., Sabounchi, P., Lin, R., & Lee, L. P. (2005). Continuous perfusion microfluidic cell culture array for high-throughput cell-based assays. *Biotechnology and Bioengineering*, 89(1), 1 - 8.
- Hung, P. J., Lee, P. J., Sabounchi, P., Lin, R., & Lee, L. P. (2005). Continuous perfusion microfluidic cell culture array for high-throughput cell-based assays. *Biotechnology and Bioengineering*, 89(1), 1-8.
- Incropera, F. P., DeWitt, D. P., Bergman, T. L., & Lavine, A. S. (2006). *Fundamentals of Heat and Mass Transfer* (6th ed.): John Wiley & Sons, Inc.
- Inglis, D. W. (2010). A method for reducing pressure-induced deformation in silicone microfluidics. *Biomicrofluidics*, 4(2), 026504.
- Irimia, D., Geba, D. A., & Toner, M. (2006). Universal microfluidic gradient generator. *Analytical Chemistry*, 78, 3472 - 3477.
- Jeon, N. J., Dertinger, S. K. W., Chiu, D. T., Choi, I. S., Stroock, A. D., & Whitesides, G. M. (2000). Generation of solution and surface gradients using microfluidic systems. *Langmuir*, 16, 8311-8316.
- Jeon, N. L., Baskaran, H., Dertinger, S. K. W., Whitesides, G. M., Water, L. V. D., & Toner, M. (2002). Neutrophil chemotaxis in linear and complex gradients of interleukin-8 formed in a microfabricated device. *Nature Biotechnology*, 20, 826 - 830.
- Jeon, N. L., Dertinger, S. K. W., Chiu, D. T., Choi, I. S., Stroock, A. D., & Whitesides, G. M. (2000). Generation of Solution and Surface Gradients Using Microfluidic Systems. *Langmuir*, 16(22), 8311-8316.
- Wang, J. C., Li, X., Lin, B., Shim, S., Ming, G.-L., & Levchenko, A. (2008). A microfluidics-based turning assay reveals complex growth cone responses to integrated gradients of substrate-bound ECM molecules and diffusible guidance cues. *Lab on a Chip*, 8(2), 227-237.
- Johnson-Chavarria, E. M., Agrawal, U., Tanyeri, M., Kuhlman, T. E., & Schroeder, C. M. (2014). Automated single cell microreactor for monitoring intracellular dynamics and cell growth in free solution. *Lab on a Chip*, 14(15), 2688-2697.
- Juncker, D., Schmid, H., & Delamarche, E. (2005). Multipurpose microfluidic probe. *Nature Materials*, 4(8), 622-628.
- Kalinin, Y. V., Jiang, L., Tu, Y., & Wu, M. (2009). Logarithmic Sensing in Escherichia coli Bacterial Chemotaxis. *Biophysical Journal*, 96(6), 2439-2448.

- Kane, B. J., Zinner, M. J., Yarmush, M. L., & Toner, M. (2006). Liver-specific functional studies in a microfluidic array of primary mammalian hepatocytes. *Analytical Chemistry*, 78(13), 4291-4298.
- Kato, J., Kim, H. E., Takiguchi, N., Kuroda, A., & Ohtake, H. (2008). *Pseudomonas aeruginosa* as a model microorganism for investigation of chemotactic behaviors in ecosystem. *Journal of Bioscience and Bioengineering*, 106(1), 1-7.
- Keenan, T. M., & Folch, A. (2008). Biomolecular gradients in cell culture systems. *Lab on a Chip*, 8, 34-57.
- Keenan, T. M., Hsu, C.-H., & Folch, A. (2006). Microfluidic “jets” for generating steady-state gradients of soluble molecules on open surfaces. *Applied Physics Letters*, 89(11), 114103.
- Kestin, J., Sokolov, M., & Wakeham, W. A. (1978). Viscosity of liquid water in the range -8°C to 150°C . *Journal of Physical and Chemical Reference Data*, 7(3), 941-948.
- Kilian, K. A., Bugarija, B., Lahn, B. T., & Mrksich, M. (2010). Geometric cues for directing the differentiation of mesenchymal stem cells. *Proceedings of the National Academy of Sciences of the United States of America*, 107(11), 4872-4877.
- Kim, M., & Kim, T. (2010). Diffusion-Based and Long-Range Concentration Gradients of Multiple Chemicals for Bacterial Chemotaxis Assays. *Analytical Chemistry*, 82(22), 9401-9409.
- Kim, S., Kim, H. J., & Jeon, N. L. (2010). Biological applications of microfluidic gradient devices. *Integrative Biology*, 2(11-12), 584-603.
- Kim, T., Pinelis, M., & Maharbiz, M. M. (2009). Generating steep, shear-free gradients of small molecules for cell culture. *Biomedical Microdevices*, 11(1), 65-73.
- Kothapalli, C. R., van Veen, E., de Valence, S., Chung, S., Zervantonakis, I. K., Gertler, F. B., & Kamm, R. D. (2011). A high-throughput microfluidic assay to study neurite response to growth factor gradients. *Lab on a Chip*, 11(3), 497-507.
- Lazova, M. D., Ahmed, T., Bellomo, D., Stocker, R., & Shimizu, T. S. (2011). Response rescaling in bacterial chemotaxis. *Proceedings of the National Academy of Sciences of the United States of America*, 108(33), 13870-13875.
- Lee, J. S., Dylla-Spears, R., Teclemariam, N. P., & Muller, S. J. (2007). Microfluidic four-roll mill for all flow types. *Applied Physics Letters*, 90(7), 074103.
- Lee, P. J., Hung, P. J., Rao, V. M., & Lee, L. P. (2006). Nanoliter scale microbioreactor array for quantitative cell biology. *Biotechnology and Bioengineering*, 94(1), 5-14.
- Li, G. N., Liu, J., & Hoffman-Kim, D. (2008). Multi-molecular gradients of permissive and inhibitory cues direct neurite outgrowth. *Annals of Biomedical Engineering*, 36(6), 889-904.
- Li, Z., Mak, S. Y., Sauret, A., & Shum, H. C. (2014). Syringe-pump-induced fluctuation in all-aqueous microfluidic system implications for flow rate accuracy. *Lab on a Chip*, 14(4), 744-749.
- Lin, F., Nguyen, C. M. C., Wang, S. J., Saadi, W., Gross, S. P., & Jeon, N. L. (2004). Effective neutrophil chemotaxis is strongly influenced by mean IL-8 concentration. *Biochemical and Biophysical Research Communications*, 319(2), 576-581.
- Long, T., & Ford, R. M. (2009). Enhanced Transverse Migration of Bacteria by Chemotaxis in a Porous T-Sensor. *Environmental Science & Technology*, 43(5), 1546-1552.

- Lucchetta, E. M., Lee, J. H., Fu, L. A., Patel, N. H., & Ismagilov, R. F. (2005). Dynamics of *Drosophila* embryonic patterning network perturbed in space and time using microfluidics. *Nature*, 434(7037), 1134-1138.
- Ma, L., Zhou, C., Lin, B., & Li, W. (2010). A porous 3D cell culture micro device for cell migration study. *Biomedical Microdevices*, 12(4), 753-760.
- Ma, Y., Zhu, C., Ma, P., & Yu, K. T. (2005). Studies on the Diffusion Coefficients of Amino Acids in Aqueous Solutions. *Journal of Chemical & Engineering Data*, 50(4), 1192-1196.
- Maguire, T. J., Novik, E., Chao, P., Barminko, J., Nahmias, Y., Yarmush, M. L., & Cheng, K.-C. (2009). Design and application of microfluidic systems for in vitro pharmacokinetic evaluation of drug candidates. *Current Drug Metabolism*, 10, 1192- 1199.
- Mark, D., Haeberle, S., Roth, G., von Stetten, F., & Zengerle, R. (2010). Microfluidic lab-on-a-chip platforms: requirements, characteristics and applications. *Chemical Society Reviews*, 39(3), 1153-1182.
- Marrucci, G., & Astarita, G. (1967). Linear, steady, two-dimensional flows of viscoelastic liquids. *AIChE Journal*, 13(5), 931-935.
- Meer, A. D. V. D., Vermeul, K., Poot, A. A., Feijen, J., & Vermes, I. (2010). A microfluidic wound-healing assay for quantifying endothelial cell migration. *American Journal of Physiology Heart and Circulatory Physiology*, 298, H719- H725.
- Meier, M., Lucchetta, E. M., & Ismagilov, R. F. (2010). Chemical stimulation of the *Arabidopsis thaliana* root using multi-laminar flow on a microfluidic chip. *Lab on a Chip*, 10(16), 2147-2153.
- Min, T. L., Mears, P. J., Golding, I., & Chemla, Y. R. (2012). Chemotactic adaptation kinetics of individual *Escherichia coli* cells. *Proceedings of the National Academy of Sciences of the United States of America*, 109(25), 9869-9874.
- Morel, M., Galas, J.-C., Dahan, M., & Studer, V. (2012). Concentration landscape generators for shear free dynamic chemical stimulation. *Lab on a Chip*, 12(7), 1340-1346.
- Mosadegh, B., Saadi, W., Wang, S. J., & Jeon, N. L. (2008). Epidermal growth factor promotes breast cancer cell chemotaxis in CXCL12 gradients. *Biotechnology and Bioengineering*, 100(6), 1205-1213.
- Müller, C. B., Loman, A., Pacheco, V., Koberling, F., Willbold, D., Richtering, W., & Enderlein, J. (2008). Precise measurement of diffusion by multi-color dual-focus fluorescence correlation spectroscopy. *Europhysics Letters*, 83(4), 46001.
- Nagai, M., Ryu, S., Thorsen, T., Matsudaira, P., & Fujita, H. (2010). Chemical control of Vorticella bioactuator using microfluidics. *Lab on a Chip*, 10(12), 1574-1578.
- Nakajima, A., Ishihara, S., Imoto, D., & Sawai, S. (2014). Rectified directional sensing in long-range cell migration. *Nature Communications*, 5, 5367.
- Nandagopal, S., Wu, D., & Lin, F. (2011). Combinatorial Guidance by CCR7 Ligands for T Lymphocytes Migration in Co-Existing Chemokine Fields. *PLoS ONE*, 6(3), e18183.
- Nève, N., Kohles, S., Winn, S., & Tretheway, D. (2010). Manipulation of Suspended Single Cells by Microfluidics and Optical Tweezers. *Cellular and Molecular Bioengineering*, 3(3), 213-228.
- Nguyen, N.-T. (2012). *Micromixers- Fundamentals, Design and Fabrication* (2nd ed.): Elsevier.

- Nguyen, N-T. & Wesley, S. (2002). *Fundamentals and Applications of Microfluidics*. Boston, London: Artech House.
- Oh, K. W., Lee, K., Ahn, B., & Furlani, E. P. (2012). Design of pressure-driven microfluidic networks using electric circuit analogy. *Lab on a Chip*, 12(3), 515-545.
- Paguirigan, A. L., & Beebe, D. J. (2008). Microfluidics meets cell biology: bridging the gap by validation and application of microscale techniques for cell biological assays. *Bioessays*, 30(9), 811.
- Park, H., Pontius, W., Guet, C. C., Marko, J. F., Emonet, T., & Cluzel, P. (2010). Interdependence of behavioural variability and response to small stimuli in bacteria. *Nature*, 468(7325), 819-823.
- Park, J. Y., Hwang, C. M., & Lee, S. H. (2007). Gradient generation by an osmotic pump and the behavior of human mesenchymal stem cells under the fetal bovine serum concentration gradient. *Lab on a Chip*, 7(12), 1673-1680.
- Park, J. Y., Kim, S.-K., Woo, D.-H., Lee, E.-J., Kim, J.-H., & Lee, S.-H. (2009). Differentiation of Neural Progenitor Cells in a Microfluidic Chip-Generated Cytokine Gradient. *Stem Cells*, 27(11), 2646-2654.
- Perkins, T. T., Smith, D. E., & Chu, S. (1997). Single Polymer Dynamics in an Elongational Flow. *Science*, 276(5321), 2016-2021.
- Probst, R., Cummins, Z., Ropp, C., Waks, E., & Shapiro, B. (2012). Flow Control of Small Objects on Chip: Manipulating Live Cells, Quantum Dots, and Nanowires. *IEEE Control System Magazine*, 32(2), 26-53.
- Qasaimeh, M. A., Gervais, T., & Juncker, D. (2011). Microfluidic quadrupole and floating concentration gradient. *Nature Communications*, 2, 464.
- Qian, C., Wong, C. C., Swarup, S., & Chiam, K.-H. (2013). Bacterial Tethering Analysis Reveals a “Run-Reverse-Turn” Mechanism for *Pseudomonas* Species Motility. *Applied and Environmental Microbiology*, 79(15), 4734-4743.
- Queval, A., Ghattamaneni, N. R., Perrault, C. M., Gill, R., Mirzaei, M., McKinney, R. A., & Juncker, D. (2010). Chamber and microfluidic probe for microperfusion of organotypic brain slices. *Lab on a Chip*, 10(3), 326-334.
- Ricart, B. G., John, B., Lee, D., Hunter, C. A., & Hammer, D. A. (2011). Dendritic Cells Distinguish Individual Chemokine Signals through CCR7 and CXCR4. *The Journal of Immunology*, 186(1), 53-61.
- Rosa, P., Tenreiro, S., Chu, V., Outeiro, T. F., & Conde, J. P. (2012). High-throughput study of alpha-synuclein expression in yeast using microfluidics for control of local cellular microenvironment. *Biomicrofluidics*, 6(1), 14109-141099.
- Roth, K. B., Eggleton, C. D., Neeves, K. B., & Marr, D. W. M. (2013). Measuring cell mechanics by optical alignment compression cytometry. *Lab on a Chip*, 13(8), 1571-1577.
- Ruan, J., Wang, L. H., Xu, M. F., Cui, D. X., Zhou, X. M., & Liu, D. Y. (2009). Fabrication of a microfluidic chip containing dam, weirs and gradient generator for studying cellular response to chemical modulation. *Materials Science & Engineering C-Biomimetic and Supramolecular Systems*, 29(3), 674-679.
- Rusconi, R., Guasto, J. S., & Stocker, R. (2014). Bacterial transport suppressed by fluid shear. *Nature Physics*, 10(3), 212-217.

- Russom, A., Irimia, D., & Toner, M. (2009). Chemical gradient-mediated melting curve analysis for genotyping of SNPs. *Electrophoresis*, 30(14), 2536-2543.
- Saadi, W., Wang, S. J., Lin, F., & Jeon, N. L. (2006). A parallel-gradient microfluidic chamber for quantitative analysis of breast cancer cell chemotaxis. *Biomedical Microdevices*, 8(2), 109-118.
- Schneider, C. A., Rasband, W. S., & Eliceiri, K. W. (2012). NIH Image to ImageJ: 25 years of image analysis. *Nature Methods*, 9(7), 671-675.
- Segall, J. E., Block, S. M., & Berg, H. C. (1986). Temporal comparisons in bacterial chemotaxis. *Proceedings of the National Academy of Sciences of the United States of America*, 83(23), 8987-8991.
- Shamloo, A., Ma, N., Poo, M. M., Sohn, L. L., & Heilshorn, S. C. (2008). Endothelial cell polarization and chemotaxis in a microfluidic device. *Lab on a Chip*, 8(8), 1292-1299.
- Shemesh, J., Jalilian, I., Shi, A., Guan, H. Y., Knothe Tate, M. L., & Majid, E. W. (2015). Flow-induced stress on adherent cells in microfluidic devices. *Lab on a Chip*, 15, 4114-4127.
- Spiro, P. A., Parkinson, J. S., & Othmer, H. G. (1997). A model of excitation and adaptation in bacterial chemotaxis. *Proceedings of the National Academy of Sciences of the United States of America*, 94(14), 7263-7268.
- Springer, M. S., Goy, M. F., & Adler, J. (1979). Protein methylation in behavioural control mechanisms and in signal transduction. *Nature*, 280(5720), 279-284.
- Squires, T. M., & Quake, S. R. (2005). Microfluidics: Fluid physics at the nanoliter scale. *Reviews of Modern Physics*, 77(3), 977-1026.
- Stokes, G. G. (2009). *Mathematical and Physical Papers*: Cambridge University Press.
- Sugiura, S., Hattori, K., & Kanamori, T. (2010). Microfluidic Serial Dilution Cell-Based Assay for Analyzing Drug Dose Response over a Wide Concentration Range. *Analytical Chemistry*, 82(19), 8278-8282.
- Sulston, J. E. (2003). *Caenorhabditis elegans: The Cell Lineage and Beyond (Nobel Lecture)*. *ChemBioChem*, 4(8), 688-696.
- Suri, S., & Schmidt, C. E. (2010). Cell-Laden Hydrogel Constructs of Hyaluronic Acid, Collagen, and Laminin for Neural Tissue Engineering. *Tissue Engineering Part A*, 16(5), 1703-1716.
- Sutera, S. P., & Skalak, R. (1993). The History of Poiseuille's Law. *Annual Review of Fluid Mechanics*, 25(1), 1-20.
- Takayama, S., Ostuni, E., LeDuc, P., Naruse, K., Ingber, D. E., & Whitesides, G. M. (2003). Selective Chemical Treatment of Cellular Microdomains Using Multiple Laminar Streams. *Chemistry & Biology*, 10(2), 123-130.
- Tanyeri, M., Ranka, M., Sittipolkul, N., & Schroeder, C. M. (2011). A microfluidic-based hydrodynamic trap: design and implementation. *Lab on a Chip*, 11(10), 1786-1794.
- Tanyeri, M., & Schroeder, C. M. (2013). Manipulation and Confinement of Single Particles Using Fluid Flow. *Nano Letters*, 13(6), 2357-2364.
- Taylor, G. I. (1934). The Formation of Emulsions in Definable Fields of Flow. *Proceedings of the Royal Society A*, 146(858), 501-523.

- Thielicke, W., & Stamhuis, E. J. (2014). PIVlab – Towards User-friendly, Affordable and Accurate Digital Particle Image Velocimetry in MATLAB. *Journal of the Operational Research Society*, 2(1), 30.
- Thorsen, T., Maerkl, S. J., & Quake, S. R. (2002). Microfluidic Large-Scale Integration. *Science*, 298(5593), 580-584.
- Toetsch, S., Olwell, P., Prina-Mello, A., & Volkov, Y. (2009). The evolution of chemotaxis assays from static models to physiologically relevant platforms. *Integrative Biology*, 1(2), 170-181.
- Toh, A. G. G., Wang, Z. P., Yang, C., & Nguyen, N.-T. (2014). Engineering microfluidic concentration gradient generators for biological applications. *Microfluidics and Nanofluidics*, 16(1-2), 1-18.
- Toh, G. G. A., Yang, C., Wang, Z., & Nguyen, N.-T. (2016). Combinational concentration gradient confinement through stagnation flow. *Lab on a Chip*, 16(2), 368-376.
- Tong, Z., Balzer, E. M., Dallas, M. R., Hung, W.-C., Stebe, K. J., & Konstantopoulos, K. (2012). Chemotaxis of Cell Populations through Confined Spaces at Single-Cell Resolution. *PLoS ONE*, 7(1), e29211.
- Tripathi, A., Kathuria, N., & Kumar, A. (2009). Elastic and macroporous agarose-gelatin cryogels with isotropic and anisotropic porosity for tissue engineering. *Journal of Biomedical Materials Research Part A*, 90A(3), 680-694.
- Unger, M. A., Chou, H.-P., Thorsen, T., Scherer, A., & Quake, S. R. (2000). Monolithic Microfabricated Valves and Pumps by Multilayer Soft Lithography. *Science*, 288(5463), 113-116.
- VanDersarl, J. J., Xu, A. M., & Melosh, N. A. (2011). Rapid spatial and temporal controlled signal delivery over large cell culture areas. *Lab on a Chip*, 11(18), 3057-3063.
- Vazquez, M., & Paull, B. (2010). Review on recent and advanced applications of monoliths and related porous polymer gels in micro-fluidic devices. *Analytica Chimica Acta*, 668(2), 100-113.
- Velve-Casquillas, G., Le Berre, M., Piel, M., & Tran, P. T. (2010). Microfluidic tools for cell biological research. *Nano Today*, 5(1), 28-47.
- Walker, G. M., Sai, J., Richmond, A., Stremmler, M., Chung, C. Y., & Wikswo, J. P. (2005). Effects of flow and diffusion on chemotaxis studies in a microfabricated gradient generator. *Lab on a Chip*, 5(6), 611-618.
- Walker, G. M., Zeringue, H. C., & Beebe, D. J. (2004). Microenvironment design considerations for cellular scale studies. *Lab on a chip*, 4, 91-97.
- Walsh, C. L., Babin, B. M., Kasinskas, R. W., Foster, J. A., McGarry, M. J., & Forbes, N. S. (2009). A multipurpose microfluidic device designed to mimic microenvironment gradients and develop targeted cancer therapeutics. *Lab on a Chip*, 9(4), 545-554.
- Wang, C. J., Li, X., Lin, B., Shim, S., Ming, G. L., & Levchenko, A. (2008). A microfluidics-based turning assay reveals complex growth cone responses to integrated gradients of substrate-bound ECM molecules and diffusible guidance cues. *Lab on a Chip*, 8(2), 227-237.
- Wang, S. J., Saadi, W., Lin, F., Nguyen, C. M. C., & Jeon, N. L. (2004). Differential effects of EGF gradient profiles on MDA-MB-231 breast cancer cell chemotaxis. *Experimental Cell Research*, 300(1), 180-189.

- Wang, S. Y., Yue, F., Zhang, L. C., Wang, J. R., Wang, Y. Y., Jiang, L., & Wang, Q. (2009). Application of microfluidic gradient chip in the analysis of lung cancer chemotherapy resistance. *Journal of Pharmaceutical and Biomedical Analysis*, 49(3), 806-810.
- Weibel, D. B., & Whitesides, G. M. (2006). Applications of microfluidics in chemical biology. *Current Opinion in Chemical Biology*, 10(6), 584-591.
- Xia, Y., & Whitesides, G. M. (1998). Soft lithography. *Annu. Rev. Mater. Sci.*, 28(1), 153-184.
- Xu, H., Ferreira, M. M., & Heilshorn, S. C. (2014). Small-molecule axon-polarization studies enabled by a shear-free microfluidic gradient generator. *Lab Chip*, 14(12), 2047-2056.
- Young, Y. N., & Shelley, M. J. (2007). Stretch-Coil Transition and Transport of Fibers in Cellular Flows. *Phys. Rev. Lett.*, 99(5), 058303.
- Yuan, J., Branch, R. W., Hosu, B. G., & Berg, H. C. (2012). Adaptation at the output of the chemotaxis signalling pathway. *Nature*, 484(7393), 233-236.
- Zhang, X., Daou, A., Truong, T. M., Bertram, R., & Roper, M. G. (2011). Synchronization of mouse islets of Langerhans by glucose waveforms. *Am J Physiol Endocrinol Metab*, 301(4), E742-747.
- Zhang, X., Grimley, A., Bertram, R., & Roper, M. G. (2010). Microfluidic system for generation of sinusoidal glucose waveforms for entrainment of islets of Langerhans. *Anal. Chem.*, 85(15), 6704- 6711.
- Zheng, G. X., Wang, Y. H., & Qin, J. H. (2012). Microalgal motility measurement microfluidic chip for toxicity assessment of heavy metals. *Analytical and Bioanalytical Chemistry*, 404(10), 3061-3069.
- Zicha, D., Dunn, G. A., & Brown, A. F. (1991). A new direct-viewing chemotaxis chamber. *Journal of Cell Science*, 99, 769-775.
- Zigmond, S. H., & Hirsch, J. G. (1973). Leukocyte locomotion and chemotaxis. New methods for evaluation and demonstration of a cell-derived chemotactic factor. *J. Exp. Med.*, 137(2), 387-410.
- Ziolkowska, K., Jedrych, E., Kwapiszewski, R., Lopacinska, J., Skolimowski, M., & Chudy, M. (2010). PDMS/glass microfluidic cell culture system for cytotoxicity tests and cells passage. *Sensors and Actuators B-Chemical*, 145(1), 533-542.